

A STATIONARY DIGITAL BREAST TOMOSYNTHESIS SYSTEM: DESIGN  
SIMULATION, CHARACTERIZATION AND IMAGE RECONSTRUCTION

Ramya Rajaram

A dissertation submitted to the faculty of the University of North Carolina at  
Chapel Hill in partial fulfillment of the requirements for the degree of Doctor of  
Philosophy in the Curriculum of Applied Sciences and Engineering.

Chapel Hill  
2009

Approved by:

Dr. Otto Z. Zhou

Dr. David S. Lalush

Dr. Jianping Lu

Dr. Yueh Z. Lee

Dr. Sha Chang

## ABSTRACT

RAMYA RAJARAM: A stationary digital breast tomosynthesis system: design simulation, characterization and image reconstruction

(Under the direction of Dr. Otto Zhou)

Conventional screen-film and/or digital mammography, despite being the most popular breast imaging modalities, suffer from certain limitations, most important of which is tissue overlap and false diagnoses arising thereof. A new three-dimensional alternative for breast cancer screening and diagnosis is tomosynthesis in which a limited number of low-dose two-dimensional projection images of a patient are used to reconstruct the three-dimensional tissue information. The tomosynthesis systems currently under development all incorporate an x-ray source that moves over a certain angle to acquire images. This tube motion is a major limitation because it degrades image quality, increases the scan time and causes prolonged patient discomfort. The availability of independently controllable carbon nanotube cathodes enabled us to explore the possibility of setting up a stationary multi-beam imaging system. In this dissertation we have proposed a stationary digital breast tomosynthesis scanner using spatially distributed carbon nanotube based field emission x-ray sources. We have presented details about the design, set-up, characterization and image reconstruction of the completely stationary digital breast tomosynthesis system.

This system has the potential to reduce the total scan time and improve the image quality in breast imaging.

Extensive design simulation results have been used to decide on the final system set-up. The fully assembled actual experimental system is capable of acquiring all the images in as little as eight seconds and yield superior image quality as well. The system has been completely characterized in terms of focal spot size, system resolution and geometric calibration. Certain important results have been obtained during the process that we hope will set the standard for the characterization of the future systems. A novel iterative reconstruction algorithm has been tried on the projection images obtained from the tomosynthesis system. Our algorithm has demonstrated image quality that is on par with the other tomosynthesis systems under development.

To Srini & Suji

## ACKNOWLEDGEMENTS

I would like to take this opportunity to thank my advisor Dr. Otto Zhou whose guidance and encouragement made this work possible. Undoubtedly, Dr. Zhou is a great advisor, a kind man and an amazing entrepreneur. I want to thank Dr. David Lalush for helping me get to this point. He has worked with me ever so patiently and has always been ready to help with my questions. I want to thank Dr. Jianping Lu for his all thoughtful insights. He helped me understand a lot of the basic science behind the various applications I have worked on. I would like to thank Dr. Yueh Lee for getting me started on the micro-computed tomography project initially and giving me the experience I needed to tackle the tomosynthesis project. I want to thank Dr. Sha Chang for being on my committee and providing me with valuable suggestions about my work. She motivates me to pursue a career in medical physics.

I want to take this opportunity to also thank all my group members, past and present – Soojin Oh, Huaizhi Geng, Jian Zhang, Lei An, Peng Wang and Zhijun Liu, my office-mates David Bordelon, Xiomara Calderon, Shabana Sultana and Tuyen Phan, former graduate student Guang Yang who was instrumental in getting the tomosynthesis system fully set up, Xin Qian, Guohua Cao, Rui Peng and Sigen Wang, and of course Christy Redmon.

I am especially grateful to my parents and my family including my sister-in-law and parents-in-law for their unwavering and enthusiastic support to me all these years.

Last but not the least, this research would not have been possible without the constant support and funding from Lineberger Cancer Center of the University of North Carolina at Chapel Hill.

## TABLE OF CONTENTS

LIST OF TABLES.....	xi
LIST OF FIGURES .....	xii
1 Introduction.....	1
1.1 Breast cancer: incidence and mortality.....	1
1.2 Mammography as a breast cancer screening modality.....	2
1.2.1 Digital mammography.....	2
1.2.2 Problems with conventional mammography .....	3
1.3 Alternatives to conventional mammography .....	4
1.3.1 Dedicated breast computed tomography.....	4
1.3.2 Digital breast tomosynthesis.....	6
1.4 Current digital breast tomosynthesis scanners .....	8
1.5 Stationary digital breast tomosynthesis system .....	12
1.5.1 Background - problems with current prototype DBT systems.....	12
1.5.2 Motivation .....	13
1.6 Carbon nanotubes based x-ray systems .....	14
1.6.1 Electron Emission Theory.....	14
1.6.2 Carbon nanotubes as field emitters.....	17
1.6.3 Carbon nanotube cathodes as x-ray sources .....	18
1.6.4 Multi-beam field emission x-ray source .....	21

References .....	22
2 Design Simulation.....	26
2.1 Simulation.....	26
2.2 Geometry simulation for tomosynthesis.....	30
2.2.1 Early Results .....	32
2.2.2 Mammography phantom.....	35
2.3 Simulated geometries.....	36
2.3.1 1D versus 2D array of sources .....	36
2.3.2 Number of projection views .....	38
2.3.3 Angular range.....	40
2.3.4 Number of iterations .....	41
2.4 Discussion of results.....	42
References .....	44
3 System.....	46
3.1 Multiple beam field emission x-ray source .....	46
3.2 Stationary digital breast tomosynthesis system – Argus.....	50
3.2.1 System overview .....	50
3.2.2 Comparison with other systems .....	52
3.2.3 Required system characterization .....	53
Reference .....	55
4 Characterization.....	56
4.1 Focal spot size.....	56
4.1.1 Initial imaging test and results .....	58

4.1.2	Pinhole imaging and results .....	60
4.2	System resolution .....	64
4.2.1	Modulation Transfer Function.....	65
4.2.2	Method for determining the MTF .....	65
4.2.3	Experiment .....	66
4.2.4	Results .....	67
4.2.5	Discussion of results.....	70
4.3	Geometry Calibration.....	72
4.3.1	Method .....	72
4.3.2	Testing.....	75
4.3.2.1	Simulation Tests & Results .....	76
4.3.2.2	Experiment & Results .....	82
4.3.3	Discussion .....	83
	References .....	85
5	Image Reconstruction.....	87
5.1	Introduction to reconstruction .....	87
5.1.1	Sampling geometry.....	89
5.1.2	Fourier Slice Theorem.....	91
5.1.3	Filtered Backprojection .....	95
5.1.4	Fan beam and cone beam reconstruction .....	97
5.2	Iterative algorithms .....	101
5.2.1	Algebraic iterative algorithms .....	103
5.2.2	Statistical Iterative Algorithms .....	107

5.3	Development of Ordered-Subsets Convex algorithm .....	111
5.4	Comparison of algorithms.....	113
5.5	Imaging experiment.....	117
5.6	Discussion .....	126
	References .....	127
6	Conclusions and Future Direction.....	130

## LIST OF TABLES

Table 1:1 Comparison of the three tomosynthesis scanners being developed by major companies. ....	9
Table 2:1 SDNR results for the one and two dimensional array of sources. ....	38
Table 2:2 SDNR results for different number of projection views.....	39
Table 2:3 SDNR results for increasing angular range.....	40
Table 3:1 Argus system specification and comparison with the other systems [4] .....	53
Table 4:1 Focal spot sizes along the long and the short sides of nine x-ray beams in Argus.....	60
Table 4:2 Focal spot sizes for various combination of focusing voltages.....	63
Table 4:3 MTF for the different x-ray beams. ....	70
Table 4:4 Calibrated and theoretical geometric parameters. ....	78
Table 4:5 Geometry parameters for magnification 2.....	81
Table 4:6 Geometry parameters for a phantom with smaller beads.....	81
Table 4:7 Geometric parameters from initial calibration test (magnification 1.1) on Argus .....	82
Table 4:8 Geometric parameters obtained using a new phantom (magnification 1.5).....	83

## LIST OF FIGURES

Figure 1.1 A dedicated breast CT scanner [11].	5
Figure 1.2 Geometry of a DBT system [13].	6
Figure 1.3 Comparison between conventional and tomosynthesis images.	8
Figure 1.4 Mammomat – the prototype tomosynthesis system from Siemens [15].	10
Figure 1.5 Mammogram image versus tomosynthesis slice.	11
Figure 1.6 Electron micrographs of the early carbon nanotubes.	15
Figure 1.7 Electron potential energy near a metal surface with/without applied field [21]	16
Figure 1.8 I-V and lifetime measurements in new CNT cathodes.	18
Figure 1.9 Triode type x-ray tube	19
Figure 1.10 Axial, coronal and sagittal views of a mouse obtained with cardiac and respiratory gating on the micro-CT system [40].	20
Figure 2.1 Illustration of source-let, object-let and detector-let [1].	29
Figure 2.2 The geometry in other DBT systems (left) and the geometry in our DBT system (right)	31
Figure 2.3 Geometry of the tomosynthesis system used in simulation.	33
Figure 2.4 The CNR in the 1x11 and the 3x11 arrays.	34
Figure 2.5 The original CIRS phantom (left) and the simulated CIRS-type phantom (right).	35
Figure 2.6 A single noise-free projection image of the simulated CIRS type phantom.	36
Figure 2.7 Effect of the number of projection views within a fixed angle.	39
Figure 2.8 Effect of angular range on the image quality.	41

Figure 2.9 Reconstructed slice of the CIRS type phantom (with 25 sources over 48°) .....	41
Figure 2.10 Effect of the number of iterations. ....	42
Figure 3.1 The multi-beam field emission x-ray system and schematic of a single source (below) .....	47
Figure 3.2 The nine-beam imaging system and projection images. ....	48
Figure 3.3 Reconstructed slices of the breast phantom obtained from the preliminary system. ....	49
Figure 3.4 Argus system geometry showing the 25 x-ray sources and the flat panel detector [4]. ....	50
Figure 3.5 Photo of a completely assembled Argus system .....	51
Figure 4.1 True versus effective focal spot size.....	57
Figure 4.2 Estimation of the effective focal spot size by using the geometric unsharpness method. ....	59
Figure 4.3 Design of the cross-wire phantom used to estimate the focal spot size (left) and a single projection image of the phantom (right) .....	59
Figure 4.4 The pinhole phantom with the 100 μm pinhole. ....	61
Figure 4.5 An image of the pinhole. ....	62
Figure 4.6 Integrated intensity of the long and the short side of the effective focal spot.....	63
Figure 4.7 Spatial resolution in terms of modulation transfer function (MTF). ....	65
Figure 4.8 Generation of a composite LSF.....	66
Figure 4.9 Calculation of the MTF.....	68
Figure 4.10 MTF plots for the three x-ray sources. ....	69
Figure 4.11 Plot of the detector MTF. ....	69
Figure 4.12 Illustration of the scanner geometry for estimation of geometric parameters [20].....	73

Figure 4.13 A single projection image of the simulated calibration phantom. ....	77
Figure 4.14 Reconstruction using the theoretical and the calibrated geometric parameters. ....	79
Figure 4.15 Intensity profiles for the theoretical and the calibrated reconstruction sets. ....	80
Figure 4.16 Typical imaging geometry in tomosynthesis.....	84
Figure 5.1 Different data sampling geometries. ....	89
Figure 5.2 Object space (left) and the sinogram space (right). ....	90
Figure 5.3 An example of an object and its projections. ....	91
Figure 5.4 An object $f(x,y)$ and its projection $P_{\theta}(t_1)$ are shown for an angle $\theta$ [5]	92
Figure 5.5 The Fourier Slice Theorem.....	94
Figure 5.6 Illustration of the backprojection process [4]. ....	97
Figure 5.7 Fan-beam and parallel projections [1]. ....	98
Figure 5.8 Generation of a sinogram. ....	98
Figure 5.9 Mapping of parallel and fan beam projections on to sinogram space.	99
Figure 5.10 Geometry for cone beam imaging [4]. ....	101
Figure 5.11 Sequence in an iterative reconstruction algorithm [12].....	102
Figure 5.12 Kaczmarz method for finding the solution to a system of consistent linear equations [12]. ....	104
Figure 5.13 Early projection images and reconstruction results.....	112
Figure 5.14 Representative slices of the CIRS type phantom reconstructed with MOSC. ....	115
Figure 5.15 Representative slices of the CIRS type phantom reconstructed with SART.....	115
Figure 5.16 (a) Contrast and (b) noise as a function of iteration number in the two reconstructions. ....	116

Figure 5.17 A single projection image of the home-made sponge phantom.....	117
Figure 5.18 Slices of the sponge phantom reconstructed with MOSC.....	118
Figure 5.19 A single projection image of the commercial breast phantom.....	119
Figure 5.20 Slices of the commercial breast phantom reconstructed with MOSC. .....	120
Figure 5.21 Reconstructed slices of the breast phantom obtained from the GE tomosynthesis unit. ....	121
Figure 5.22 MTF of the GE scanner as determined using a 100 $\mu\text{m}$ wire (left) and using a 10 $\mu\text{m}$ wire (right). ....	123
Figure 5.23 Slices of the commercial breast phantom reconstructed with MOSC after application of an edge-smoothing mask (projection images from Argus). .....	125
Figure 5.24 Tomographic slices that show two different sets of calcifications in the breast phantom. ....	125

## **1 Introduction**

### **1.1 Breast cancer: incidence and mortality**

According to the National Cancer Institute (NCI), breast cancer is the second most common cancer among women in the United States. There were about 184,450 new cases of breast cancer in 2008 of which 40930 were fatal [1]. The NCI also estimates that 12.7% of women born today will be diagnosed with breast cancer at some point in their lives.

A lot of research has been done to find what causes breast cancer and to find ways to prevent, diagnose and cure it. Despite a long-term increase in the incidence of breast cancer, data from the Surveillance, Epidemiology and End Results (SEER) Program show a decrease in breast cancer mortality rate of 2.3% per year from 1990 to 2001 [2]. The increased incidence of breast cancer is due to the widespread availability of screening mammography [3]. While mammographic screening can identify cancers earlier, and helps with the diagnosis of noninvasive cancers and pre-malignant lesions, it is also fair to say that screening has reduced the breast cancer mortality rate. Other forms of screening include breast-self exam, clinical breast exam, ultrasonography and magnetic resonance imaging but x-ray mammograms continue to be the most widely accepted, approved and cost-effective way to diagnose cancer.

## **1.2 Mammography as a breast cancer screening modality**

Mammography can identify cancers that are too small to find by physical examination in addition to finding ductal carcinoma in situ which is a non-invasive condition. Mammography utilizes ionizing radiation namely x-rays to obtain images of the compressed breast on either an x-ray film or a digital detector. It is routine practice to obtain a medio-lateral oblique (MLO) view and a cranio-caudal (CC) view of the breast. The two views are then used to identify abnormalities in the breast tissue.

The sensitivity of mammography (number of true positives) is about 75% [4], although it may be less sensitive for younger women and women with high breast density [5]. The specificity of mammography is related to a screening test being normal when a cancer is absent. The specificity in conventional or digital mammography is about 90% [4, 5]. A low specificity means a large number of false positives resulting in a number of unnecessary follow-up examinations, not to mention the anxiety associated with it.

### **1.2.1 Digital mammography**

While most screening mammography the world over uses the screen-film technology, the advent of sophisticated digital detectors has made the adoption of digital screening mammography easier. In a digital mammography (DM) system, we have a computer and a digital detector instead of a screen-film cassette. Digital mammography may be more expensive costing about 1.5 to 4 times the screen-film system but it offers ease of data storage, manipulation and

sharing, faster image acquisition and shorter exams, and potentially improved contrast. Many studies have established that DM is at least as accurate as screen-film mammography in terms of image quality. The recent Digital Mammographic Imaging Screening Trial [5] that evaluated a large group of women who underwent both examinations concluded that DM had a higher sensitivity and specificity among pre-menopausal and peri-menopausal women, in younger women and in women with dense breasts. A few other studies have shown that while DM has higher cancer detection rates, it may also have a higher recall rate (the rate at which women screened using mammography are called back again for re-assessment) [6, 7].

### **1.2.2 Problems with conventional mammography**

Although screening mammography is widely accepted around the world and plays a very important role in the early detection of breast cancer, it is still not 100% accurate. It misses about 30% of cancers due to various reasons but foremost is the fact that screening mammography, screen-film or digital, is only a two-dimensional imaging modality wherein compressed projection images of a three-dimensional breast are obtained on a two-dimensional screen. It is possible for some lesions to be obscured by over- and underlying normal tissue because of the intrinsic tissue overlap. This is particularly a problem in radio-dense breasts where super-imposed tissues can either obscure an abnormality leading to decreased sensitivity or they may themselves appear as an abnormality

thereby decreasing the specificity of the examination. In addition, in conventional mammograms, depth information about the lesions is not made available.

### **1.3 Alternatives to conventional mammography**

The shortcomings with conventional x-ray mammography led to an interest in the development of tomographic imaging for breast. In standard tomographic imaging, the x-ray tube and the detector move synchronously around the patient [8] on opposite sides to obtain multiple projection images. It is possible to reconstruct specific planes of interest through the patient's body by shifting and adding these projection images. Tomographic imaging has enabled depth localization. It improves the conspicuity of features by removing overlapping tissues. It can also improve local contrast by restricting the dynamic range to a single slice [8]. Tomographic imaging of the breast can be done using either a dedicated breast computed tomography (DBCT) system or a digital breast tomosynthesis system.

#### **1.3.1 Dedicated breast computed tomography**

The concept of breast CT got started in the 1970s soon after the advent of CT technology [9, 10] but only recently has there been an increased interest in dedicated breast CT systems. The opinion is that CT of the breast may be much better than just projection mammography because CT has the potential to eliminate overlapping structures [11]. In a DBCT system, about 300-500 images of the breast are taken as the scanner rotates 360° around the patient and these

images are then reconstructed to yield high-quality three-dimensional slices through the breast. A design for a DBCT scanner is shown in figure 1.1. CT would be done in the coronal plane. As the patient lies prone on the table with the breast hanging in the pendulant position, the scanner and the detector would rotate around the breast in the horizontal position [11].

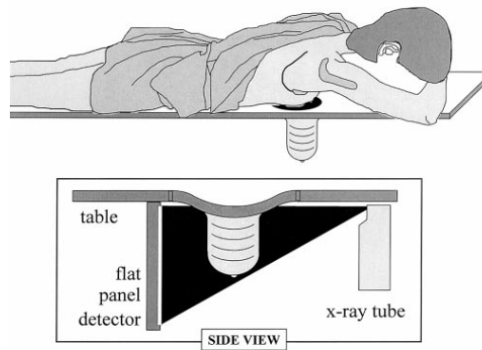


Figure 1.1 A dedicated breast CT scanner [11].

The patient is then typically scanned using x-rays at 80-120 kVp but the tube voltage and tube-current-time product can be adjusted to deliver the same dose to the patient as in a conventional two-view mammogram [12]. About 500 projection images of the patient breast are acquired which are then reconstructed in to 300-500 512x512 images. The breast CT images can then be stacked in the coronal, axial or sagittal planes to show specific lesions if need be. It is possible to adjust section thickness, contrast and brightness.

The first clinical experience [12] with DBCT showed that while the overall performance of DBCT is similar to conventional mammography, it may still have certain limitations. In this first study, micro-calcifications were not well visualized, particularly in dense breasts. With 500 or more projection images, dose is an issue, and often certain tube parameters for a certain breast thickness have to be

chosen after a very careful consideration of a trade-off between patient dose and image noise. The other issue is that DBCT may not be very efficient in imaging the chest wall. In the above clinical study, the pectoralis muscle was seen in only about 18% of the patients. This is a major disadvantage with DBCT although future modifications to the breast CT table may address this shortcoming.

### 1.3.2 Digital breast tomosynthesis

Digital breast tomosynthesis (DBT) is a new kind of imaging modality designed to overcome the major limitation of a conventional mammographic system, that of tissue overlap. In DBT, a limited number of low-dose projection images are acquired so that the total dose to the patient is still comparable to conventional two-view mammography. The geometry of a DBT system is shown in Figure 1.2.

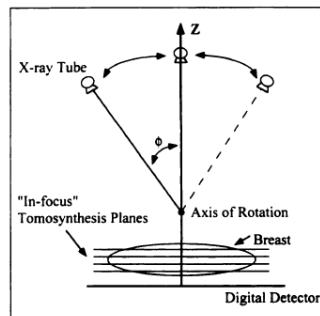


Figure 1.2 Geometry of a DBT system [13].

These two-dimensional images are then reconstructed into a three-dimensional data set with a high isotropic in-plane resolution and a much lower depth resolution. This data set consists of slices that are relatively free of tissue clutter compared to a standard mammogram. Thus DBT allows the radiologist to

see through the “structured noise” of normal breast tissue to aid in the detection and characterization of cancers [13]. Although successful implementation of tomosynthesis was initially delayed because of the lack of digital detectors, the rapid advances in digital imaging technology has now made tomosynthesis a reality. Most of the current DBT systems primarily use a stationary detector and mechanical arms that move the x-ray source in an arc above the detector. Different groups have developed their own reconstruction algorithms to allow image reconstruction for the limited angle tomosynthesis geometry. In one of the earliest studies on tomosynthesis [13], images of a commercial two-dimensional accreditation phantom obtained using tomosynthesis, conventional screen-film imaging, and conventional digital imaging were compared to establish the superiority of tomosynthesis over the conventional methods. The conventional digital and screen-film images of the phantom that show the different features in a plane are shown in figure 1.3 (a) and 1.3 (b) while the tomosynthesis image is shown in Figure 1.3 (c).

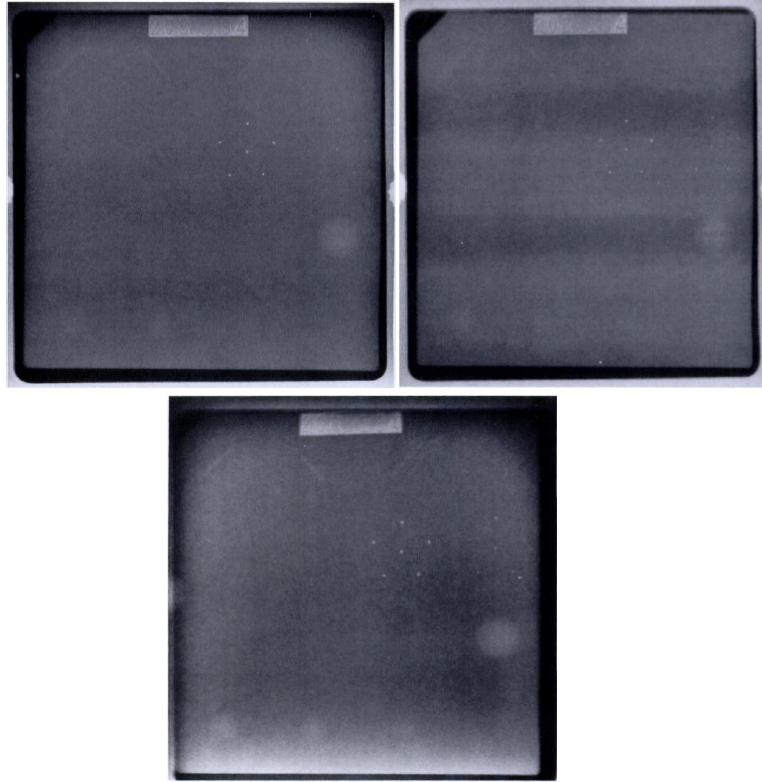


Figure 1.3 Comparison between conventional and tomosynthesis images.

(a) Conventional digital image (b) conventional screen-film image and (c) tomosynthesis image of a commercial accreditation phantom [13]

The masses, fibers and calcifications are seen as well with tomosynthesis as with conventional imaging. This preliminary study concluded that the image quality of the tomosynthesis image is sufficient to pass the American College of Radiology (ACR) criteria for phantom images [13].

#### **1.4 Current digital breast tomosynthesis scanners**

There are currently at least three tomosynthesis systems under development by major medical technology companies. These include the Senographe 2000D from General Electric (GE) [14], the Mammomat Novation

from Siemens [15] and Selenia from Hologic [16]. A brief description of each system's characteristics is in Table 1.

Parameters	GE Senographe 2000D	Siemens Mammomat Novation	Hologic Selenia
kVp, mA	25-30 kVp, ~130 mA	~28 kVp, ~180 mA	24-39 kVp, ~100 mA
Focal spot size	300 $\mu$ m	300 $\mu$ m	300 $\mu$ m
Target/filter	Mo/Mo, Rh/Rh	W/Rh	Mo, W/Al, Rh
Angle coverage	50°	50°	30°
View numbers	11	25/49	11
Gantry motion	Step-and-shoot	Continuous	Continuous
Detector	CsI: a-Silicon	Direct converter	Direct converter
Detector size	18 x 23.4 cm	23.9 x 30.5 cm	24 x 29 cm
Pixel pitch	100 $\mu$ m	85 $\mu$ m	140 $\mu$ m
Readout time	0.3 s	0.3/0.6 s	0.6 s
Integration time	0.4 s	0.2 s	1.0 s
Exposure time	0.1 s	0.03 s	0.073 s
Scan time	7 s for 11 views	20 s for 25 views	18 s for 11 views
Total dose	45 – 143 mAs	80 – 133.4 mAs	80 – 160 mAs
Reconstruction method	Maximum Likelihood - Expectation Maximization	Filtered Back Projection	Filtered Back Projection

Table 1:1 Comparison of the three tomosynthesis scanners being developed by major companies.

All the three systems are modified full field digital mammography systems. The gantry with the x-ray source moves about 15° to 50° around the patient while acquiring 11 to 49 projection views of the breast. These images are reconstructed using different algorithms in each case. The resultant depth resolution is about 1 mm while the in-plane resolution is between 100 and 150  $\mu$ m. A photograph of a commercial prototype DBT scanner is shown in figure 1.4.



Figure 1.4 Mammomat – the prototype tomosynthesis system from Siemens [15].

From the results published by the researchers working on these DBT scanners, it is evident that tomosynthesis offers great promise as an alternative to conventional mammography. Phantom and patient results have demonstrated that tomosynthesis removes structure noise and greatly improves the in-slice low contrast detectability [14, 15, 16]. A comparison between a tomosynthesis image of a patient breast and the corresponding mammogram is shown in figure 1.5.

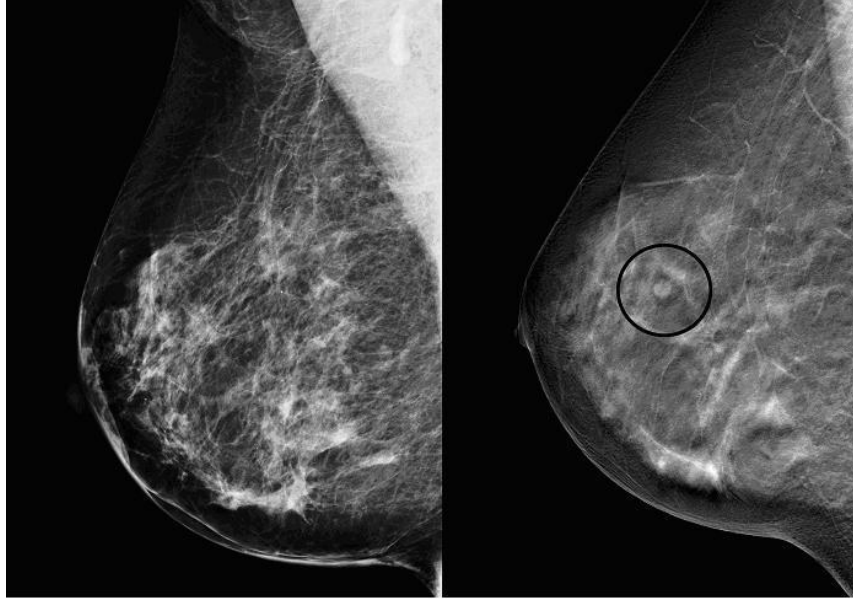


Figure 1.5 Mammogram image versus tomosynthesis slice.

On the left is a mammogram of a patient breast in the MLO view and on right is a tomosynthesis slice showing a lesion that was not seen in the mammogram [16] (which later turned out to be a benign mass)

It is to be noted that the x-ray focal spot size in the three systems is about 300  $\mu\text{m}$ . The imaging time is also about 7 to 40 s, which is larger than the about 1 s imaging time for conventional mammography. It is important to note that each of the three systems has adopted one of two gantry rotation techniques. GE has adopted the step-and-shoot technique wherein the gantry containing the x-ray source makes a full stop at each projection angle to obtain an image before moving on to the next view. Hologic and Siemens have adopted the continuous rotation technique wherein the gantry keeps moving continuously albeit slowly so that x-ray images of the patient are acquired at each projection angle even while the source is moving.

## **1.5 Stationary digital breast tomosynthesis system**

### **1.5.1 Background - problems with current prototype DBT systems**

From the previous discussion about currently available DBT scanners, it is evident that in the step-and-shoot technique where the gantry stops and starts intermittently, the gantry experiences high acceleration and deceleration in each imaging cycle leading to a large vibration of the gantry. The continuous rotation technique on the other hand leads to an enlargement in the effective focal spot size of the x-ray source in the direction of motion. Both techniques therefore lead to significant degradation in image quality. In addition, either kind of rotation requires some additional time which results in a longer scan time. A longer scan time means more blur due to patient motion thus affecting the overall image quality.

From the above discussion about DBT, we can infer that DBT may be better than conventional mammography and has a great potential to replace it for screening and/or diagnostic purposes. The current DBT systems under development have achieved significant results towards greater acceptance of DBT as a viable alternative to conventional mammography. At the same time, from a discussion of the disadvantages with the current systems, it is easy to see that there is great room for improvement. It should be possible to reduce the scan time so that the patient has to endure the pain of compression that much less. To significantly reduce the scan time would require a much faster rotation of the gantry. It may not be as easy as it sounds because a faster gantry is more

expensive and would also cause a significant enlargement of the effective focal spot. However, if images of the patient could be acquired without any rotation of the gantry, then it would definitely be possible to reduce the total scan time. The concept of using a non-rotating gantry with spatially distributed x-ray sources for tomography was investigated before. The Dynamic Spatial Reconstructor [17] developed at the Mayo clinic was one of the first systems to use about 28 x-ray sources and 28 opposing detectors. It was able to obtain a complete volume (about 240 cross-sections) of the patient body from 28 views recorded in  $1/100^{\text{th}}$  of a second and repeated 60 times/s. However, several issues such as cost, size and maintenance led to the eventual demise of the system. Later, the electron-beam computed tomographic system [18] and the scanning-beam digital x-ray system [19] used an electromagnetic field to steer an electron beam to different points on the x-ray target to produce a scanning x-ray beam. Such systems tended to be bulky and generally had a smaller angular coverage because of difficulties with steering the electron beam.

### **1.5.2 Motivation**

Since 2000, several researchers have been extremely interested in using carbon nanotube (CNT) based x-ray sources. Our lab was one of the earliest in 2002 to experiment with x-ray generation using CNT cathodes. Great improvements have since been made in terms of the x-ray tube current, cathode stability and lifetime. Before going into a brief description about CNTs and their properties, it is important to note that the availability of CNT cathodes has made

it possible for us to build a multiple beam field emission x-ray system. Such a system has no mechanical movement of any gantry and is completely stationary. The x-ray sources are all fixed in space and can be individually turned on, either sequentially or simultaneously, to acquire projection images of an object on a fixed detector. Therein lays the motivation to this project. We have the means to build a DBT system that is better than currently available systems and we want to be able to employ those means to demonstrate the feasibility and potential superiority of a truly stationary DBT system.

## **1.6 Carbon nanotubes based x-ray systems**

Carbon nanotubes are considered the fourth allotrope of carbon, in addition to diamond, graphite and fullerene. They were first observed and reported by Iijima [20] who called them microtubules of graphitic carbon. Electron micrographs of these early CNTs are shown in figure 1.6. Carbon nanotubes can be single or multi-walled. They are endowed with exceptional electronic, mechanical, thermal and chemical properties. These properties make them suitable for several applications such as nano-electronics, scanning probe microscopy, chemical and biological sensors, composites, and of course, as electron field emission sources.

### **1.6.1 Electron Emission Theory**

The emission of electrons from a conducting material like a metal is based on Fermi-Dirac statistics. At low temperatures, the energy of most electrons is

lower than the Fermi energy and therefore they remain bound. The electrons can be extracted by two processes – thermionic emission and field emission [21].

These are illustrated in figure 1.7.

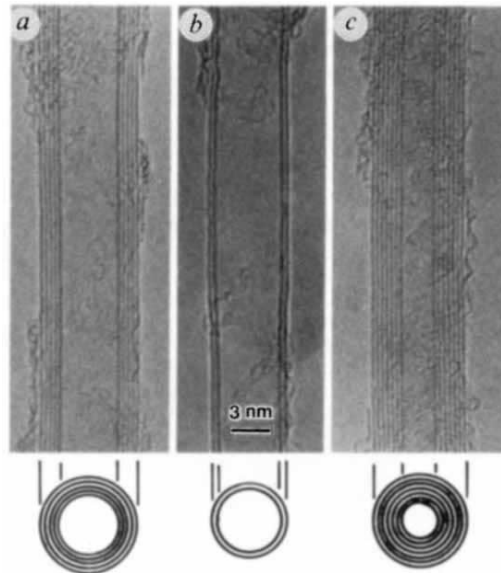


Figure 1.6 Electron micrographs of the early carbon nanotubes.

(a) Tube with five graphitic sheets (b) Two-sheet tube (c) seven-sheet tube [20].

As the temperature is increased, some electrons gain enough energy to overcome the surface potential barrier and become free. This is called thermionic emission because of the involvement of high temperatures. Sometimes, when there is a strong external electric field, it is possible for the electrons to “tunnel” through the surface energy barrier. This process is called field emission as it is aided by the external field.

Although thermionic sources have enabled the development of various applications such as the simple light bulb, picture display tubes, cathode ray tubes, oscillators, rectifiers and electron microscopes, they have some inherent disadvantages. The need to heat the surface to high temperatures to enable

thermionic emission severely affects the lifetime and the size of a potential device. In addition, the slow response time of the thermionic sources limits the temporal resolution achievable. Often, they require complicated electromagnetic optics to accurately focus the random thermal electrons. On the other hand, field emission electron sources need only low operating temperatures. They lend themselves to easy miniaturization and their response time is almost instantaneous.

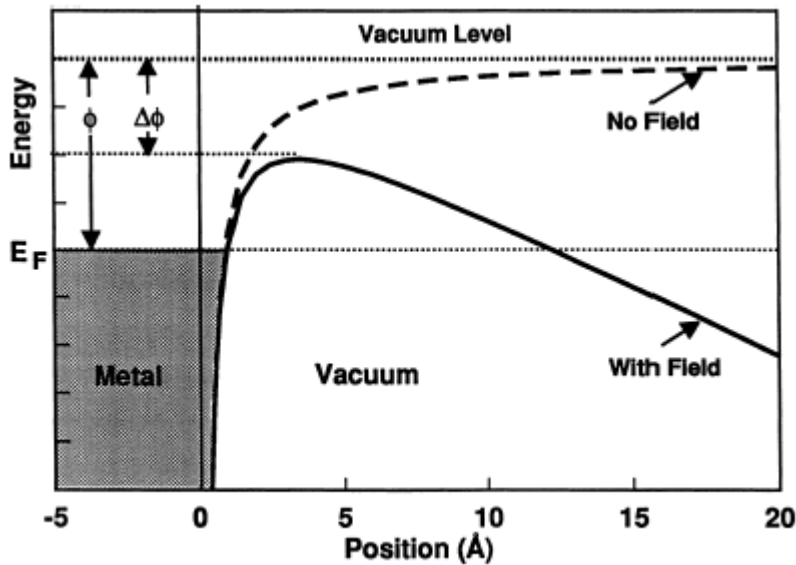


Figure 1.7 Electron potential energy near a metal surface with/without applied field [21]

Field emission is explained by the famous Fowler-Nordheim equation [22 – 24]:

$$J = a\phi^{-1}F^2 \exp\left[-v(f)b\phi^{3/2} / F\right] \quad \text{Equation 1-1}$$

where

$a = 1.54 \times 10^{-6} \text{ A eV V}^{-2}$  and  $b = 6.83 \text{ eV}^{-3/2} \text{ V nm}^{-1}$  and  $v(f)=1- f + (1/6) f \ln f \dots$ ,

and  $f = 1.44 \text{ eV}^2 \text{ V}^{-1} \text{ nm})(F/\phi^2)$

Here,  $F$  is the local field about the emission area. It is related to the applied field as

$$F = \beta \cdot V/d \quad \text{Equation 1-2}$$

$V$  is the total voltage drop between anode and cathode,  $d$  is the distance between the two electrodes, and  $\beta$  is called the field enhancement factor that is determined by the geometry of the cathode. It can be shown from electromagnetic theory that sharper the tip, the larger the enhancement factor and the lower the applied voltage required to achieve the same field emission current.

### **1.6.2 Carbon nanotubes as field emitters**

Carbon nanotubes have atomically sharp tips and a large aspect ratio. So the field enhancement factors of CNTs are much greater than that of conventional Spindt-type emitters. Carbon nanotubes have been widely studied as field emission electron sources for x-ray tubes, display devices and electron microscopes [25 - 27]. The field required to turn on electron emission from CNTs is 1-2 V/ $\mu\text{m}$  [28, 29] which is much lower than other electron emitting materials. Carbon nanotubes are also more stable at high currents and have a long life time [30, 31]. The lifetime and current achieved on the nanotubes made recently in our group are shown in figure 1.8. Field emission cathodes based on CNTs have been fabricated by self-assembly, dielectrophoresis and electrophoretic methods [30-32].

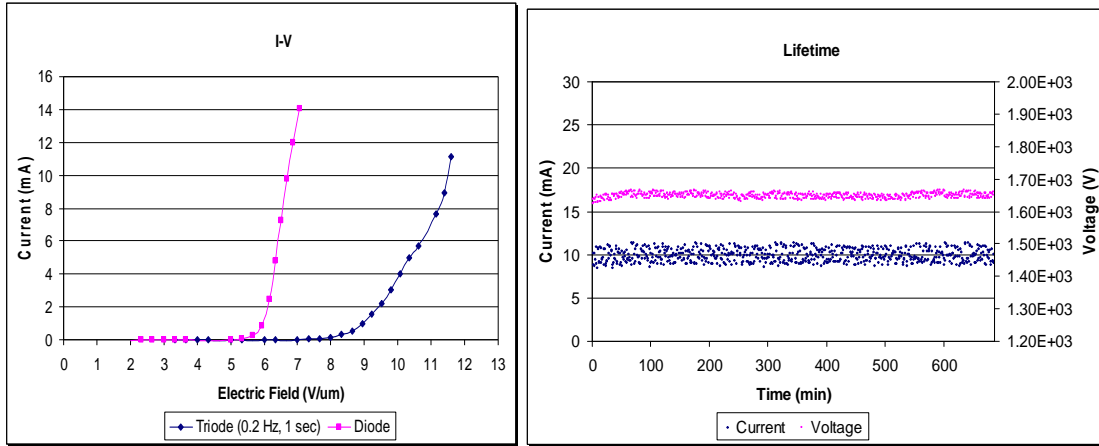


Figure 1.8 I-V and lifetime measurements in new CNT cathodes.

Shown on left is the I-V plot of a recent batch of CNTs. The maximum current in diode mode is about 14 mA. On right is a plot of the lifetime measurement. The CNT cathode stays stable at about 10 mA (0.15 Hz, 1 sec) for nearly 15 hours (data courtesy Xiomara Calderon, manuscript in progress).

### 1.6.3 Carbon nanotube cathodes as x-ray sources

It was reported in 2001 that aligned CNT field emitters could be used as an x-ray source in an x-ray tube [33]. Previously published results from our group have demonstrated the generation of x-rays from a CNT-based triode type field-emission x-ray tube [34-36]. While our early research was focused on the development of a diode type x-ray tube, later research shifted focus on to the triode type field emission x-ray tube in order to meet certain crucial objectives such as high temporal resolution and high spatial resolution. The triode structure incorporates focusing stages so that we have in the x-ray tube the CNT based cathode, a gate, one or two focusing stages and the anode (metal target). A schematic illustration of the triode type x-ray tube is shown in figure 1.9.

The design of the above focusing structure was optimized by means of electron beam simulation using a commercial software program called Vector Fields. An elliptical cathode of dimension 2.35 mm x 0.72 mm was fabricated on silicon wafer using a combined process of photolithography and electrophoresis developed in our laboratory [37 – 39].

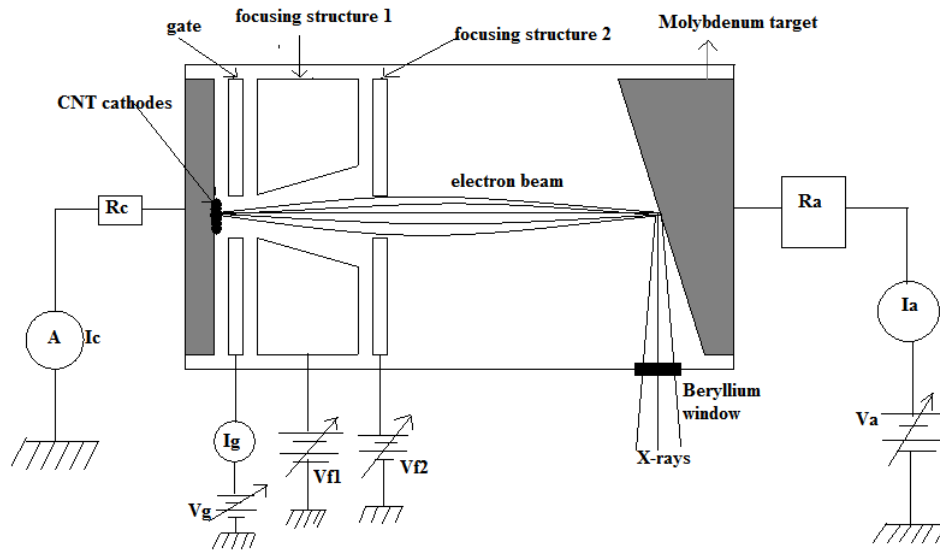


Figure 1.9 Triode type x-ray tube

The tube includes a CNT based field emission cathode, a gate, two focusing structures and a Molybdenum target as the anode. Electrons are extracted from the CNT cathode upon application of a gate voltage. The electron beam is then focused by means of the focusing structure on to the anode. X-ray emitted from the anode exit the chamber via the beryllium window.

The x-ray system was then characterized systematically by measurement of effective focal spot size, system spatial resolution and temporal resolution [40]. Once optimized, the CNT based micro-focus x-ray system was used for in-vivo and ex-vivo micro-computed tomographic animal imaging. The x-ray source is programmed to generate radiation that is readily synchronized and gated with the non-periodic physiological signals from the animal. Efficient gating thus allows

the acquisition of images that are free from motion-blur. The system is usually operated at 40 kVp and 1 mA cathode current. About 600 or 300 projection images of the animal are acquired over either the entire 360° or over about 200°. The pulse width of the x-rays is variable depending on the application but typically the pulses are 100 ms or 50 ms long. The projection views that are obtained are later reconstructed using a commercial reconstruction algorithm and analyzed in the coronal, sagittal or axial planes. Reformatted images of a mouse imaged on our micro-CT system are shown in figure 1.10.

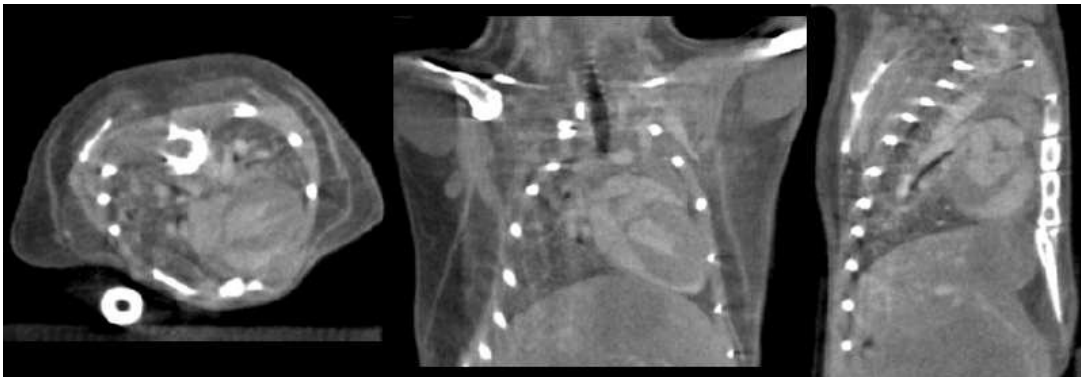


Figure 1.10 Axial, coronal and sagittal views of a mouse obtained with cardiac and respiratory gating on the micro-CT system [40].

In our first version of the micro-computed tomography (micro-CT) system, the detector and the x-ray source were held stationary while the animal is mounted on a rotation stage and rotated. This design involved holding the animal in a vertical (and therefore an unnatural) position for the duration of imaging. In the second and latest version of the micro-CT system, the system is designed such that the x-ray source and the detector are mounted on a rotating gantry while the animal is held flat and stationary on a horizontal animal bed. This CNT based micro-CT system is very unique because it enables the imaging of a free-

breathing animal in its natural position. It is to be noted that no intubation or ventilation of any kind is used on the animal in our micro-CT system.

#### **1.6.4 Multi-beam field emission x-ray source**

As we can infer from the above description of micro-CT scanners, most tomographic scanners involve the rotation of either the source or the object in order to acquire multiple projection views that can then be reconstructed to give back the three-dimensional object. Thus, some kind of mechanical movement becomes an intrinsic part of the tomographic scanners. An alternative way of generating multiple projection views without any rotation is by the use of multiple cathodes, each cathode acting as an x-ray focal point. The field emission x-ray source based on CNT cathodes can be easily miniaturized. Their fabrication process is well understood and the micro-CT system has already been validated. Taking it to the next step, if one fabricated multiple CNT based x-ray sources and placed them all in some fashion, either at regular intervals around a complete circle or in a linear array or some other arrangement, then it would be possible to build a *truly stationary* tomographic scanner that could be used either for micro-CT or tomosynthesis. It was based on this idea that we set out to explore other source geometries. Once a scanner design was finalized, it was built and completely characterized. Images were obtained from this truly stationary x-ray imaging system and reconstructed successfully to demonstrate the feasibility of the multi-beam x-ray source idea. That is the story that will be told in the next four chapters.

## References

1. <http://www.cancer.gov/cancertopics/types/breast>
2. Ries LAG, Eisner MP, et al.: SEER Cancer Statistics Review, 1975-2001. Bethesda, Md: National Cancer Institute, 2004.
3. Hemminki K, Rawal R, et al.: Mammographic screening is dramatically changing age-incidence data for breast cancer. *J Clin Oncol* 22 (22): 4652-3, 2004.
4. Carney PA, Miglioretti DL, et al.: Individual and combined effects of age, breast density, and hormone replacement therapy use on the accuracy of screening mammography. *Ann Intern Med* 138 (3): 168-75, 2003.
5. Pisano ED, Gatsonis C, et al.: Diagnostic performance of digital versus film mammography for breast-cancer screening. *N Engl J Med* 353 (17): 1773-83, 2005.
6. Del Turco MR, Mantellini P, et al.: Full-field digital versus screen-film mammography: comparative accuracy in concurrent screening cohorts. *AJR Am J Roentgenol* 189 (4): 860-6, 2007.
7. Skaane P, Hofvind S, et al.: Randomized trial of screen-film versus full-field digital mammography with soft-copy reading in population-based screening program: follow-up and final results of Oslo II study. *Radiology* 244 (3): 708-17, 2007.
8. Dobbins JT and Godfrey DJ: Digital x-ray tomosynthesis: current state of the art and clinical potential. *Phys Med Biol* 48: R65-R106, 2003.
9. Chang C, Sibala J, et al.: Computed tomographic evaluation of the breast. *AJR Am J Roentgenol* 131: 459-464, 1978.
10. Gisvold J, Reese D, et al.: Computed tomographic mammography (CTM). *AJR Am J Roentgenol* 133: 1143-1149, 1979
11. Boone JM, Nelson TR, et al.: Dedicated breast CT: radiation dose and image quality evaluation. *Radiology* 221: 657-667, 2001
12. Lindfors KK, Boone JM, et al.: Dedicated breast CT: initial clinical experience. *Radiology* 246(3): 725, 2008
13. Niklason LT, Christian BT, et al.: Digital tomosynthesis in breast imaging. *Radiology* 205: 399-406, 1997.

14. Wu T, Stewart A, et al.: Tomographic mammography using a limited number of low-dose cone-beam projection images. *Med Phys* 30(3), 2003
15. Bissonnette M, Hansroul M, et al.: Digital breast tomosynthesis using an amorphous selenium flat panel detector. *Proc. of SPIE* 5745, 2005.
16. Ren B, Ruth C, et al.: Design and performance of the prototype full field breast tomosynthesis system with selenium based flat panel detector. *Proc. of SPIE* 5745, 2005.
17. Bobb RA, Hoffman EA, et al.: High-speed three dimensional x-ray computed tomography: the dynamic spatial reconstructor. *Proc. Of the IEEE* 71(3), 1983.
18. Lipton MJ, Higgins CB, et al.: Cardiac imaging with a high-speed cine-CT scanner: preliminary results. *Radiology* 152(3): 579-582, 1984.
19. Speidel MA, Wilfley BP, et al.: Scanning beam digital x-ray (SBDX) technology for interventional and diagnostic cardiac angiography. *Med. Phys.* 33(8), 2006.
20. Iijima S: Helical microtubules of graphitic carbon. *Nature* 354(7), 1991.
21. Temple D: Recent progress in field emitter array development for high performance applications. *Mater. Sci. Engg. R: Reports*, 24(5): 185-239(55), 1999
22. Spindt CA, Brodie I, Humphrey L, et al.: Physical properties of thin-film field emission cathodes with molybdenum cones. *J. Appl. Phys.* 47: 5248-5263, 1976.
23. Brodie I and Spindt CA: Vacuum Microelectronics. *Advances in Electronics and Electron Physics* 83: 1-106, 1992.
24. Brodie I and Schwoebel PR: Vacuum microelectronic devices. *Proc. of the IEEE* 82(7): 1006, 1994.
25. Saito Y, Uemura S, et al.: Cathode ray tube lighting elements with carbon nanotube field emitters. *Jpn. J. Appl. Phys.* 37: L346-L348, 1998.
26. Choi WB, Jin YW, et al.: Electrophoresis deposition of carbon nanotubes for triode-type field emission display. *Appl. Phys. Lett.* 78: 1547, 2001.

27. Cheng Y, Zhang J, et al.: Dynamic radiography using a carbon-nanotube-based field-emission x-ray source. *Rev. Sci. Instr.* 75(10): 3264-3267, 2004.
28. Collins PG and Zettl A: A simple and robust electron beam source from carbon nanotubes. *Appl. Phys. Lett.* 69(13): 1969-1971, 1996.
29. Zhu W, Bower C, et al.: Large current density from carbon nanotube field emitters. *Appl. Phys. Lett.* 75(6), 1999.
30. Oh SJ, Cheng Y, et al.: Room-temperature fabrication of high-resolution carbon nanotube field-emission cathodes by self-assembly. *Appl. Phys. Lett.* 82(15), 2003.
31. Oh SJ, Zhang J, et al.: Liquid-phase fabrication of patterned carbon nanotube field emission cathodes. *Appl. Phys. Lett.* 84(19), 2004.
32. Zhang J, Tang J, et al.: Efficient fabrication of carbon nanotube point electron sources by dielectrophoresis. *Adv. Mater.* 16(14), 2004.
33. Sugie H, Tanemura M, et al.: Carbon nanotubes as electron source in an x-ray tube. *Appl. Phys. Lett.* 78(17), 2001.
34. Yue GZ, Qiu Q, et al.: Generation of continuous and pulsed diagnostic imaging x-ray radiation using a carbon-nanotube-based field-emission cathode. *Appl. Phys. Lett.* 81(2), 2002.
35. Zhou O and Lu JP: X-ray generating mechanism using electron field emission cathode. U.S. Patent 6,553,096, 2003.
36. Zhou O and Lu JP: X-ray generating mechanism using electron field emission cathode. U.S. Patent 6,850,595, 2005.
37. Gao B, Yue GZ, et al.: Fabrication and electron field emission properties of carbon nanotube films by electrophoretic deposition. *Adv. Mater.* 13(23), 2001.
38. Oh SJ, Zhang J, et al.: Liquid-phase fabrication of patterned carbon nanotube field emission cathodes. *Appl. Phys. Lett.* 84(19), 2004.
39. Liu Z, Yang G, et al.: Carbon nanotube based microfocus field emission x-ray source for microcomputed tomography. *Appl. Phys. Lett.* 89, 103111, 2006.

40. Cao G, Lee YZ, et al.: Respiratory-gated micro-CT using a carbon nanotube based micro-focus field emission x-ray source. Proc. of SPIE 6913, 691304, 2008.

## **2 Design Simulation**

### **2.1 Simulation**

Computer simulation makes use of theoretical models to predict the performance of a real system. In general, the simulation could be statistical or analytical. Statistical simulation is based on random number generation and uses the physical properties of the interaction process to predict system performance. Often problems that are too complex to solve analytically can be solved numerically. The most well known statistical simulation process is the Monte Carlo simulation which is used in various fields such as economics, physics and engineering. Analytical simulations model and solve for systems using analytical equations. An example would be the generation of projection images of theoretical phantoms. The projection can be calculated based on the line integrals of attenuation coefficients of objects whose shape can be described by closed-form equations, that is, the phantom consists of say, cylindrical, spherical or cubical objects. For a certain source and detector position, the line integral through the object can be calculated accurately. The final result would be a weighted summation of the integrals [1].

Computer simulation is vastly applicable in designing the optics of a system. For example, it helps understand the effect of say focal spot size,

detector size, source-to-detector distance etc on the final system resolution. Simulation is a very useful tool when designing a new x-ray tomographic system. In order to design a new system, the right set of parameters is required. The process of finding the optimum parameters is not an easy one. It is generally not possible or feasible to use real components to build and optimize a system repeatedly. On the other hand, if all the programs are in place, then a simple computer simulation will not only enable the researchers to find the optimum set-up but aid them in the analysis of the effect of various factors on the system performance.

In a tomographic imaging set-up, the first step is the production of x-rays. The two important things about the generated x-rays are the x-ray spectrum and the x-ray flux. The x-ray photons generated in a tube often pass through additional filtration such as beryllium, molybdenum, etc before reaching the target and this affects the flux. The x-ray spectrum has a significant effect on the resulting image contrast and more importantly, the dose to the patient. In general, for mammography, the mean energy of the x-ray spectrum is chosen to be less than 20 keV in order to improve low-contrast detectability. Computer simulations can help the designer achieve a good balance between x-ray flux and x-ray spectrum [2, 3]. The second step is the interaction between the x-ray photons and the object that is scanned. This includes energy dependent attenuation (beam hardening), scatter, etc. Many of these processes have been thoroughly analyzed using computer simulation studies [4-6]. The third step is the detector and its associated electronics. Since detector manufacturing is very

time-consuming and expensive, computer simulation studies can greatly help in predicting the required detector geometries, the detection quantum efficiency and noise characteristics before the production of the actual system [7].

Simulations are also crucial in the development of reconstruction algorithms. It would take much longer for a system to be fully operational if the reconstruction algorithm development were to start after the system is built. It will also be difficult to separate the non-exact nature of the reconstruction algorithm from the non-ideal behavior of a system. Many algorithms for the newer CT system geometries were developed based on the results of computer simulation studies [8-10]. It is easy to see that computer simulations help a great deal in the successful setting up and characterization of a tomographic imaging system. It is a complicated topic and it is not possible to describe all aspects of a simulation study here. However, one of the most commonly used techniques in simulation is to divide complicated geometries into small elements so that their response could be considered a point response. For example, the x-ray focal spot and the detector are both divided into matrices of finer elements. Each element in the source matrix is called a source-let and each element in the detector matrix is called the detector-let [1]. For each source-let and detector-let, the x-ray path can be approximated by a pencil beam of very small width. The source-let, the path-let and the detector-let are illustrated in figure 2.1. In simulations, a phantom is usually a complex object formed by combining spheres, ellipsoids, rectangles, etc. Each component can be divided into elements and each element is called object-let. The line integral along a path-let for each object-let can be calculated

analytically by solving for the length of intersection of the ray with each object-let. The total signal received by a detector is the weighted sum of all the path-lets through the object-lets and is expressed as

$$p = \sum_{i=1} w_i \sum_{k=1} \mu_k l_{i,k} \quad \text{Equation 2.1}$$

Here,  $l_{i,k}$  is the length for object  $k$  intersecting path-let  $i$  and  $w_i$  is the weighting factor for path-let  $i$  [1].

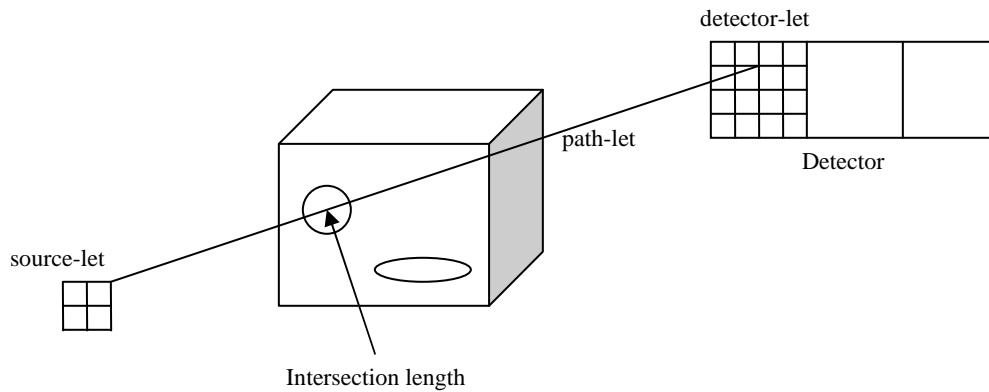


Figure 2.1 Illustration of source-let, object-let and detector-let [1].

From the above figure, we see that sixteen path integrals need to be calculated for each source-let when each detector channel is divided into a 4 x 4 matrix. There are 48 integrals for four source-lets. Since we have a cubical object with two ellipsoids inside, 3 cord lengths need to be calculated for each path-let so that we have a total of 144 length calculations. For a detector with 1000 channels, this means 144,000 calculations. The above calculations must be repeated for all projection views as well. It is easy to see the increasing computational complexity even for such a simple scenario. Nevertheless, the

sophisticated hardware available today can very well manage such complex simulations.

## **2.2 Geometry simulation for tomosynthesis**

When the idea of a multi-beam field emission x-ray source came up, the first step was to decide on how these x-ray sources should be arranged in order to achieve our goals of image quality and scan time. It was important to decide how many of these sources were required for the specific application in mind and to explore the different possible geometries using those sources. Before building the actual system, it was essential to optimize the geometric parameters so as to achieve the desired spatial resolution, noise performance and speed. There are many possible geometry configurations for a tomosynthesis set-up including the selection of parameters such as continuous tube motion or step-and-shoot, number of projection views, total angular coverage, detector operation modes, etc. It is important to investigate the effect of many of these factors on image quality. However our goal was to set up and characterize a carbon nanotube based *stationary digital breast tomosynthesis* system. The fact that our DBT system is going to be stationary meant that we did not have to study the effect of motion. The availability of individually addressable carbon nanotube (CNT) based x-ray sources meant that we could use the computer simulations platform to study the effect of different source arrangements. We were most interested in looking at the effect of arranging the independent sources in a one-dimensional array as well as in a two-dimensional matrix. In addition, we wanted to use the

simulations to find the optimum number of projection views as well as to find the effects on image quality of the total angular coverage. In DBT systems in general a limited number of views (less than 50) are acquired over a limited angular range (less than  $50^\circ$  and due to the incomplete sampling nature of DBT, there are bound to be artifacts. There has been a lot of research on image artifacts in DBT and their dependence on system geometry and reconstruction parameters [11-13]. However our system geometry is unique and it is vital to optimize the geometry in our stationary DBT system. The CNT sources are independent and separately fixed in space. It is easier to arrange the individually programmable CNT sources in a linear chamber as opposed to a curved path of the source that is commonly seen in the commercial systems containing their one conventional x-ray source. Design, manufacture and cost issues prompted us to consider the use of a linear chamber containing the CNT based sources rather than the sources-in-an-arc type of arrangement that would technically result in our scanner being the exact equivalent of the other DBT scanners under development [14-16] as far as source geometry is concerned. The difference is illustrated in figure 2.2. Thus our DBT system is unique because in addition to being completely stationary, it is defined by a novel source geometry.

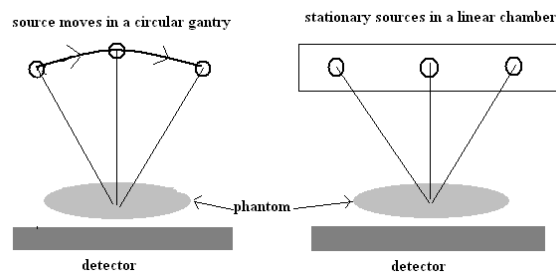


Figure 2.2 The geometry in other DBT systems (left) and the geometry in our DBT system (right)

In the simulation studies that were carried out, the physical characteristics of a commercial detector were adopted. Projection images of different phantoms were created assuming certain other fixed parameters such as dose. These projection images were then reconstructed using an iterative reconstruction method called Ordered-Subsets Convex (OSC) details of which are in chapter 5. To analyze the image quality, the contrast from profiles through reconstructed objects and the standard deviation in regions of interest were used to calculate the signal difference to noise ratio (SDNR). Various other studies have used the modulation transfer function (MTF), the artifact spread function (ASF), ripple etc to describe the in-plane resolution and out-of-plane artifacts [11, 17-19].

### **2.2.1 Early Results**

In the first test that was performed to study the effect of geometry on image quality, a simple simulated phantom was generated. This phantom included seven small spheres, each of diameter 400  $\mu\text{m}$  embedded in a uniformly absorbing background of thickness 5 cm (in the x-direction in figure 2.3). Five of these created a “plus” sign at a depth of 2.5 cm and were 4 cm apart while two other spheres were placed at depths of 1.5 cm and 3.5 cm and diagonally offset 2.5 cm from the center in the y- and z-directions. The projections of this phantom were created on a 20 cm detector. The projection images were generated for a 1 x 11 array (one-dimensional) of sources as well as for a 3 x 11 matrix of sources (two-dimensional). The projection images were reconstructed using the version of OSC algorithm available at that time.

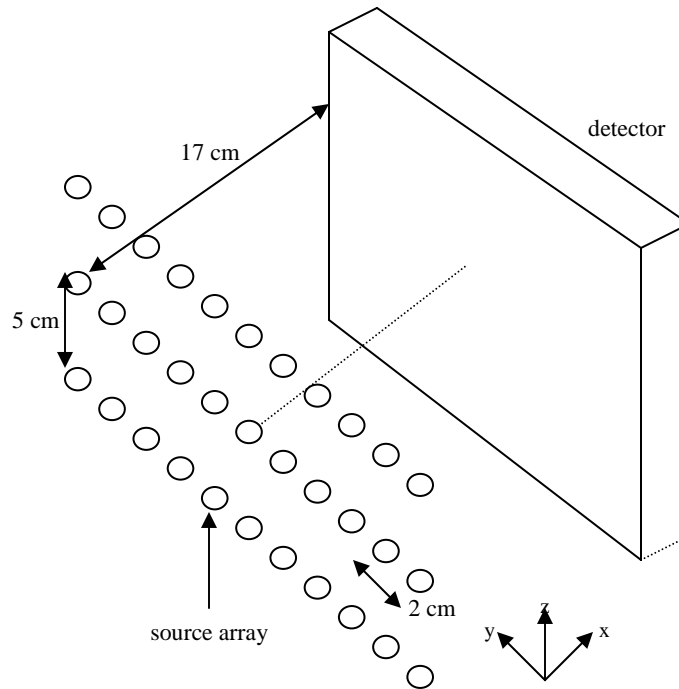


Figure 2.3 Geometry of the tomography system used in simulation.

The contrast to noise ratio was evaluated on the reconstructed slices. The same total exposure was assumed for both the one-dimensional and the two-dimensional cases. Poisson noise was simulated in the raw projection images and the standard deviation in a chosen region of interest in the reconstructed slices was calculated to represent noise.

Results indicated that the two-dimensional (2D) matrix of sources provided about 20-45% more contrast in the spheres than the one-dimensional (1D) array, the image noise was also higher at all locations in the 2D case [20]. The resultant CNR was about 5-17% higher in the 2D case (figure 2.4).

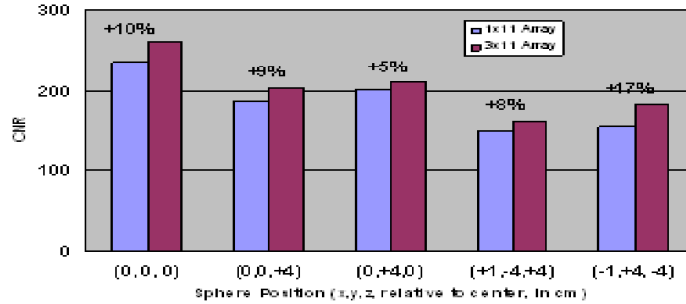


Figure 2.4 The CNR in the 1x11 and the 3x11 arrays.

From the percent increase in the CNR for spheres at various locations in the 3x11 array, it is seen that the 2D array provides improved CNR.

Although the results were encouraging, it is to be noted that the phantom used in this simulation study was too simple. In order to be more conclusive, it would be essential to simulate projection images of a slightly more complex and realistic phantom. In addition, although this specific geometry with three arrays of eleven sources provided an improvement in the CNR over the 1x11 array, the results of comparing a 3x5 matrix with a 3x9 matrix (the extra sources added on in the y-direction) in order to study the effect of source spacing in the y-direction, or the results of comparing a 3x5 matrix with a 5x5 matrix (extra sources in the z direction) in order to study the effect of increased angular coverage in the z-direction were not conclusive or consistent. It was also at this point that the reconstruction algorithm underwent a major upgrade that made it more efficient and resulted in better images. It was therefore essential to re-assess the results of the geometry simulation using a newer and more realistic phantom with the modified version of the reconstruction algorithm.

## 2.2.2 Mammography phantom

For the new study, projection images of a tissue-equivalent mammography phantom, referred to as the CIRS phantom, were created to test multiple geometric arrangements of the x-ray sources. The CIRS phantom is 4.5 cm thick and the background material simulated the average glandular breast tissue composition. The objects included in the phantom represent calcifications, fibers and masses. The size of the different objects varies from the barely visible to the clearly visible. For instance, the smallest calcifications are about 150  $\mu\text{m}$  in diameter while the largest are about 400  $\mu\text{m}$ . A picture of the original CIRS phantom [21] and the simulated CIRS phantom are shown in figure 2.5 for comparison.

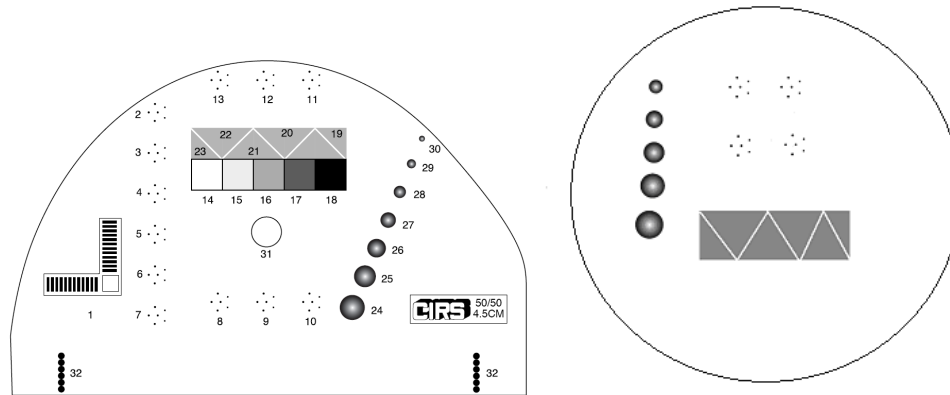


Figure 2.5 The original CIRS phantom (left) and the simulated CIRS-type phantom (right).  
In both phantoms, there are objects that represent masses, fibers and calcifications.

A single noise-free projection image of the simulated phantom is shown in figure 2.6. Noise was simulated in the projection images for the various

geometries that were analyzed. The following section gives the details of the simulation as well as the results from each of the geometries.

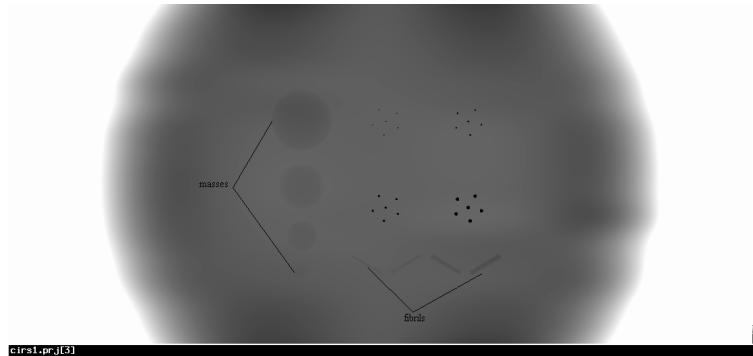


Figure 2.6 A single noise-free projection image of the simulated CIRS type phantom. The image has been windowed to show the smaller calcifications and fibers.

## 2.3 Simulated geometries

### 2.3.1 1D versus 2D array of sources

As described before, the availability of individually addressable CNT based x-ray sources means that the sources could theoretically be arranged in many ways, some of which have the potential to increase the available field of view in addition to improving image quality. Towards this end, the first geometry that was tested with the simple phantom was the 1D array of sources against the 2D matrix of sources. The same test was repeated with the CIRS type phantom. This time, the 1D array of sources had one row of 25 equally spaced sources while the 3D matrix had 3 rows of 25 equally spaced sources each. The array-to-array distance was initially fixed at 2 cm. A second test with an array spacing of 5 cm was also carried out to examine the effects of increasing the angular coverage in the z-direction (figure 2.3). In addition, the source to detector

distance was more realistically set at about 69 cm, like in the commercial full-field digital mammography systems. Projection images of the CIRS type phantom were obtained for both cases. Noise was included in the raw images so that the total exposure in the 2D case was comparable to the exposure in the 1D case. In addition, noise-free blank scans were created for both cases. The projection images were reconstructed using the modified version of the OSC algorithm and the resultant reconstructed slice containing the features of interest was subjectively and quantitatively evaluated. The contrast in the largest and the second largest centrally-located calcification was obtained by taking a profile through the objects. The noise was calculated as the standard deviation in a specific region of interest that was uniform across the 1D and the 2D scenarios. The SDNR was evaluated as  $(I_{obj}-I_{bkg})/(\text{noise})$  where  $I_{obj}$  and  $I_{bkg}$  are the intensities in the object and the background obtained by taking horizontal profiles through the objects of interest in the reconstructed image. The SDNR for the largest and the second largest calcifications were thus found at 20 iterations. Table 2.1 summarizes the results of the comparison between 1D and the 2D cases.

From the SDNR results, it is seen that given the same exposure conditions (75 mAs total), with a distance of only 2 cm between the arrays, the 3x25 case does not provide any improvement in the SDNR of the largest calcification but provides a minimal improvement in the SDNR of the second largest calcification. However, when the distance between the arrays is increased to 5 cm, the SDNR improves for both sets of calcifications, with the percentage

increase being less than 5% for the larger ones and about 10% in the case of the smaller calcifications. This improvement in SDNR is despite the noise being larger at all locations in the 3x25 case than in the 1x25 case. Thus, keeping the total exposure constant, increasing the angular coverage in the z-direction by increasing the spacing between the arrays does seem to improve the contrast, especially of the smaller objects.

Distance between arrays	Test case	Average noise	SDNR for the largest calcification	SDNR for the second largest calcification
	1x25	0.00344	136.1	50.6
2 cm	3x25	0.00374	131.2	53.7
	1x25	0.00272	109.0	3.5
5 cm	3x25	0.00299	112.8	9.9

Table 2:1 SDNR results for the one and two dimensional array of sources.

The SDNR is given for the 1x25 and the 3x25 array of sources for two different distances between the arrays.

### 2.3.2 Number of projection views

Next, the effect of the number of projection views used in a tomosynthesis set-up on the resultant image quality was studied by simulating projection images of the CIRS type phantom with varying number of sources. The total exposure is always fixed at 75 mAs, which is distributed equally among the sources. The total angular range was fixed at 48° and within that angle 7, 13, 19, 25, 31, 37 and 42 equally spaced sources were used to create the projection images. The SDNR

and the noise in each case are listed in table 2.2. It is seen that increasing the number of projection views within a fixed angle is advantageous only to a certain limit beyond which it becomes a case of diminishing returns because of the increase in noise.

Number of projection views	SDNR for largest calcification	SDNR for the second largest calcification	Noise
7	72.2	38.4	0.00307
13	110.9	43.9	0.0032
19	116.8	43.9	0.0034
25	133.1	50.6	0.0036
31	142.4	55.2	0.0036
37	135.6	59.8	0.0036
42	120.1	53.9	0.0037

Table 2:2 SDNR results for different number of projection views.

The effect of increasing projection views on the SDNR is illustrated in figure 2.7.

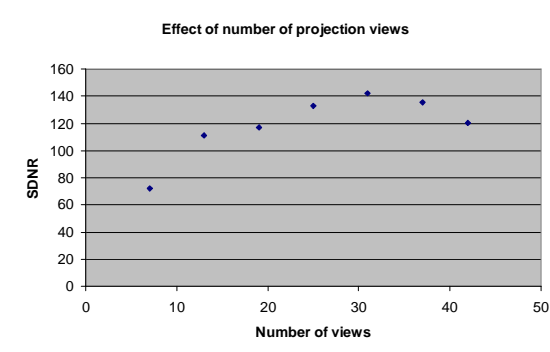


Figure 2.7 Effect of the number of projection views within a fixed angle.

Increasing the density of sources within a fixed angular range may be detrimental after a certain optimal density is reached.

### 2.3.3 Angular range

Tomosynthesis is a limited angle imaging technique that was developed in order to overcome the tissue overlap problem encountered in conventional mammography. In the several DBT prototypes that have been developed, the angular range is between 15° to 50°. The angular range determines the region that is sampled in Fourier space. A limited angle means that the Fourier space that is sampled will be reduced too. In order to study the effect of the angular range on the image quality, four scenarios were simulated under conditions of constant exposure and equally spaced sources. These are (i) 7 sources over 12°, (ii) 13 sources over 24°, (iii) 19 sources over 36° and (iv) 25 sources over 48°. Projection images of the CIRS type phantom were simulated for each case and the SDNR in the largest and the second largest calcifications were evaluated as described in the previous sections. Table 2.3 lists the SDNR results for the four cases. When the angular range is increased, the SDNR increases too, despite a higher noise in the wider angular range.

Angular range	SDNR for largest calcification	SDNR for the second largest calcification	Noise
12	66.2	38.5	0.0019
24	102.8	50.6	0.0026
36	117.1	55.2	0.0031
48	133.1	50.6	0.0034

Table 2:3 SDNR results for increasing angular range.

The effect of increasing the angular range is shown in figure 2.8. Reconstructed image from the angular range of 48° is shown in figure 2.9.

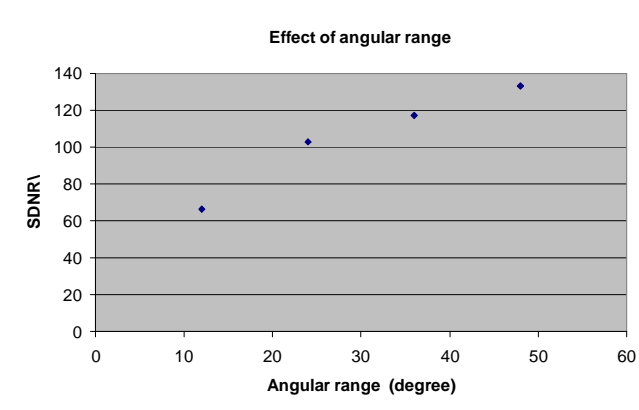


Figure 2.8 Effect of angular range on the image quality.

Increasing the angular range increases the SDNR by increasing the region sampled in Fourier space.

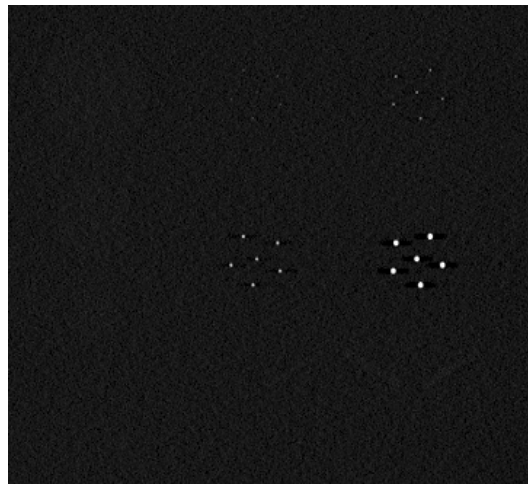


Figure 2.9 Reconstructed slice of the CIRS type phantom (with 25 sources over 48°)

The image has been windowed to show the masses, fibers and calcifications.

### 2.3.4 Number of iterations

Although the parameter number of iterations does not strictly fall under geometry, it is nevertheless essential to estimate the number of iterations required to achieve optimal image quality. In order to do this, the CIRS type phantom was reconstructed using 25 sources and the results of every other

iteration up to 20 iterations of the modified reconstruction algorithm were saved and evaluated for SDNR in the biggest calcification. The result is shown in figure 2.10. A similar trend was visualized when the second biggest calcifications were evaluated. The optimum number of iterations for good and sufficient image quality with our reconstruction algorithm is about 6.

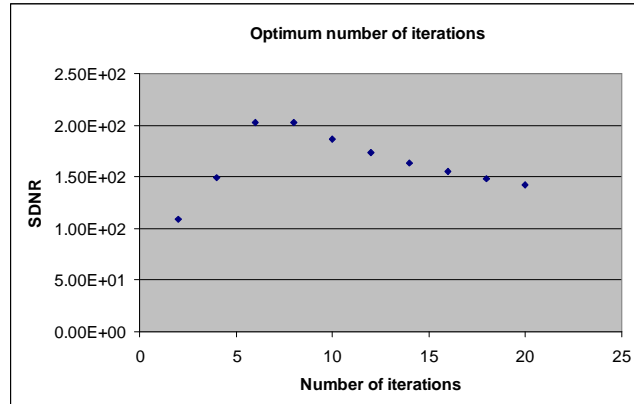


Figure 2.10 Effect of the number of iterations.

## 2.4 Discussion of results

The effect on image quality of the limited angle acquisition in DBT was investigated. Projection images of a CIRS type phantom were reconstructed using the modified OSC algorithm and the SDNR in the reconstructed images was used to compare various geometries. It is believed that the intensity of a reconstructed object is spread throughout the slice thickness so that the in-plane contrast or signal difference to noise ratio is a good indication of the depth resolution or blurring as well. The availability of novel x-ray sources allowed us to explore the possibilities of arranging them in a two-dimensional matrix as

opposed to a simple 1D arrangement. From the results of this comparison, it appears that a 2D arrangement of sources may provide a marginal improvement in the image quality and increase the available field of view for imaging. However, in terms of design and development, a chamber with 2D arrangement of sources would be far more difficult to build and characterize. Considering this trade-off, it may be worthwhile to design a simple chamber that can accommodate sources in a linear array. An analysis of the effect of number of projection views indicated that between 25 and 35 projection views should be adequate to achieve good image quality. It was also seen that increasing the density of sources beyond the optimal number only degraded image quality because of associated increase in the noise. Also, our simulations confirmed the idea that an increased angular range is more important as it allows the sampling of a larger region in Fourier space. It was also determined that 6 iterations of our reconstruction algorithm should be enough to achieve superior image quality. Although more number of iterations improves the contrast, the SDNR does not improve. Only 6 iterations can provide the necessary contrast and high SDNR and is computationally efficient as well.

## References

1. Hsieh J: Computed Tomography: Principles, Design, Artifacts, and Recent Advances, SPIE Press, 2003.
2. Ruth C and Joseph PM: Estimation of a photon energy spectrum for a computed tomography scanner. *Med. Phys.* 24(5), pp. 695-702, 1997.
3. McKinley RL, Tornai MP, et al.: Simulation study of a quasi-monochromatic beam for x-ray computed mammography. *Med. Phys.* 31(4), pp. 800-813, 2004.
4. De Man B, Nuyts J, et al.: Reduction of metal streak artifacts in x-ray computed tomography using a transmission maximum a posteriori algorithm. *Nuclear Science Symposium*, 1999.
5. Boone JM: Monte Carlo simulation of the scattered radiation distribution in diagnostic radiology. *Med. Phys.* 15(5), pp. 713-720, 1988.
6. Endo M, Tsunoo T, et al.: Effect of scattered radiation on image noise in cone beam CT. *Med. Phys.* 28(4), pp.469-474, 2001.
7. Badano A, Kyrianiou IS, et al.: Anisotropic imaging performance in indirect x-ray imaging detectors. *Med. Phys.* 33(8), pp. 2698-2713, 2006.
8. Taguchi K, Aradate H, et al.: Algorithm for image reconstruction in multi-slice helical CT. *Med. Phys.* 25(4), pp. 550-561, 1998.
9. Guan H, Yin F, et al.: Adaptive portal CT reconstruction: A simulation study. *Med. Phys.* 27(10), pp. 2209-2214, 2000.
10. Zou Y and Pan X: Exact image reconstruction on PI-lines from minimum data in helical cone-beam CT. *Phys. Med. Biol.* 49, pp. 941-959, 2004.
11. Mertelmeier T, Orman J, et al.: Optimizing filtered backprojection reconstruction for a breast tomosynthesis prototype device. *Physics of Medical Imaging, Proc. of SPIE*, 6142, 61420F, 2006.
12. Zhou J, Zhao B, et al.: A computer simulation platform for the optimization of a breast tomosynthesis system. *Med. Phys.* 34(3), pp. 1098-1109, 2007.
13. Hu YH, Zhao B, et al.: Image artifact in digital breast tomosynthesis: Investigation of the effects of system geometry and reconstruction

- parameters using a linear system approach. Med. Phys. 35(12), pp. 5242-5252, 2008.
14. Wu T, Stewart A, et al.: Tomographic mammography using a limited number of low-dose cone-beam projection images. Med Phys 30(3), 2003
  15. Bissonnette M, Hansroul M, et al.: Digital breast tomosynthesis using an amorphous selenium flat panel detector. Proc. of SPIE 5745, 2005.
  16. Ren B, Ruth C, et al.: Design and performance of the prototype full field breast tomosynthesis system with selenium based flat panel detector. Proc. of SPIE 5745, 2005.
  17. Li B, Saunders R, et al.: Measurement of slice thickness and in-plane resolution on radiographic tomosynthesis system using modulation transfer function (MTF). Med. Imag. 2006: Phys. Med. Imag. 6142, 61425D-61410, 2006.
  18. Li B, Avinash GB, et al.: Optimization of slice sensitivity profile for radiographic tomosynthesis. Med. Phys. 34 (7), pp. 2907-2916, 2007.
  19. Deller T, Jabri KN, et al.: Effect of acquisition parameters on image quality in digital tomosynthesis. Med. Imag. 2007: Phys. Med. Imag. 6510, 6510L, 2007.
  20. Lalush DS, Rajaram R, et al.: 3D tomosynthesis reconstruction from 1D and 2D x-ray source arrays. Nuclear Science Symposium Conference Record, IEEE, 2006.
  21. [http://www.cirsinc.com/011a\\_mammo.html](http://www.cirsinc.com/011a_mammo.html)

### **3 System**

#### **3.1 Multiple beam field emission x-ray source**

As was described in Chapter 1, x-ray imaging applications such as computed tomography and tomosynthesis require the acquisition of multiple two-dimensional projection views of the object/patient that are then reconstructed to give back three-dimensional object information. Most of the commercial tomographic scanners have a design where a single x-ray source (and a corresponding detector) rotates about the stationary object. The mechanical movement involved in such a source design greatly affects total scan time and image quality.

While other novel systems have been tried and tested, like the electron beam CT [1], they have not been altogether successful because of issues of size and cost. In addition, the angular range offered by these systems is often limited. The other alternative is to use many spatially distributed cathodes that then combined with their corresponding anodes can act as separate and possibly individually addressable x-ray sources. As was discussed in Chapter 1, carbon nanotubes (CNTs) are excellent field emitters and it is also easy to miniaturize the CNT based x-ray sources. Based on this idea and the development of a

single CNT cathode based system, we were able to build a multi-beam x-ray source.

The multi-beam field emission x-ray (MBFEX) source consists of five CNT cathodes, focusing stages and a molybdenum anode target. The whole set-up was arranged in a vacuum chamber with a beryllium window. The set-up of the linear MBFEX source based system is shown in figure 3.1. Multiple metal-oxide semiconductor field effect transistors (MOSFETs) were used to individually control the x-ray sources. This preliminary system was characterized by measuring the field emission current from the sources in triode mode and by focal spot size measurements [2].

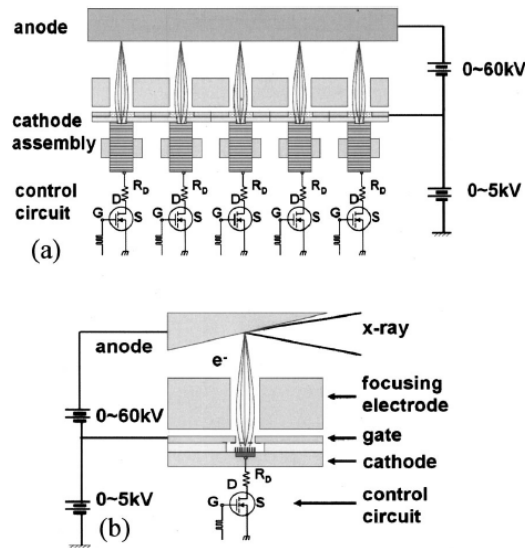


Figure 3.1 The multi-beam field emission x-ray system and schematic of a single source (below)  
 (a) The system has five cathodes, focusing electrodes and a molybdenum target. The cathode current was uniformly 1 mA with varying gate voltages across the sources and the system was operated at 40 kVp. (b) A single x-ray source consists of a 1.5 mm cathode on a metal disk, a 150  $\mu\text{m}$  dielectric spacer, an extraction gate, focusing electrode and a metal anode target [2].

Further, the MBFEX system was then used to obtain five projection images of a blade from a surgical scalpel placed behind a metal rod [2]. Imaging

was done at 40 kVp using a digital x-ray detector (Hamamatsu C7921) running at 16 frames/second. From these images, it could be seen that while the blade and the metal rod appeared as one in the central projection view, the other projection views were able to separate out the two objects. The acquisition time for the images in this system was only determined by the x-ray exposure time as there is no mechanical movement and electrical switching time is really negligible only. Another set of nine MBFEX sources over a larger angular range was used to demonstrate potential tomosynthesis applications. This system comprised of nine x-ray sources, a flat-panel detector, and a computer to synchronize the x-ray source and detector and to save the projection images. A schematic of the nine-beam system together with three of the nine projection views acquired of a commercial full size stereotactic needle biopsy tissue equivalent phantom are shown in figure 3.2.

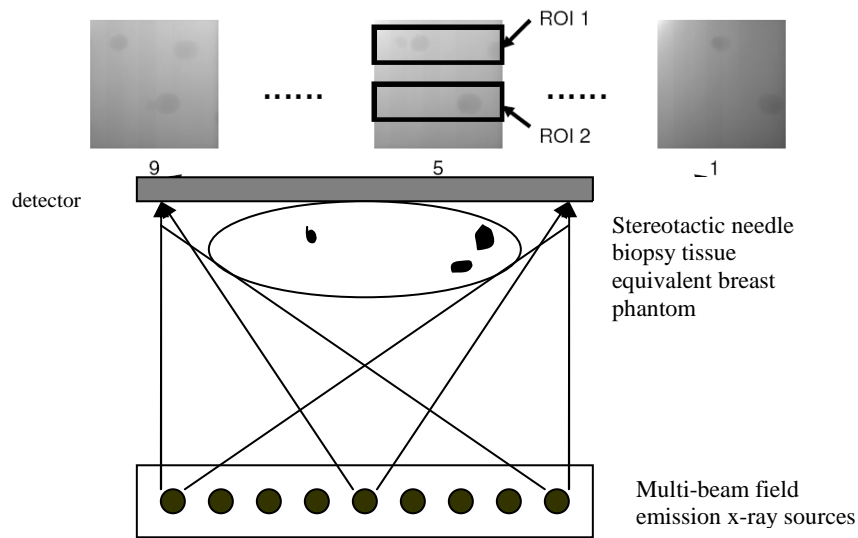


Figure 3.2 The nine-beam imaging system and projection images.

A schematic of the nine-beam imaging system with three of the nine projection images acquired of a mammography phantom showing some of the mass-like objects.

At that time, due to the limited field of view afforded by the small detector, only a portion of the breast phantom containing the masses and calcifications was imaged. The nine sources were spaced 1.14 cm apart and the source to detector distance was about 19.3 cm. The total angular coverage is therefore about 25°. About 200 pixels in the depth direction from the nine projection images of the phantom (1000 x 200 x 9) were reconstructed with non-cubic voxels of 1 mm x 0.1 mm x 0.1 mm using an appropriate algorithm [3]. The reconstructed slices through the phantom are shown in figure 3.3.

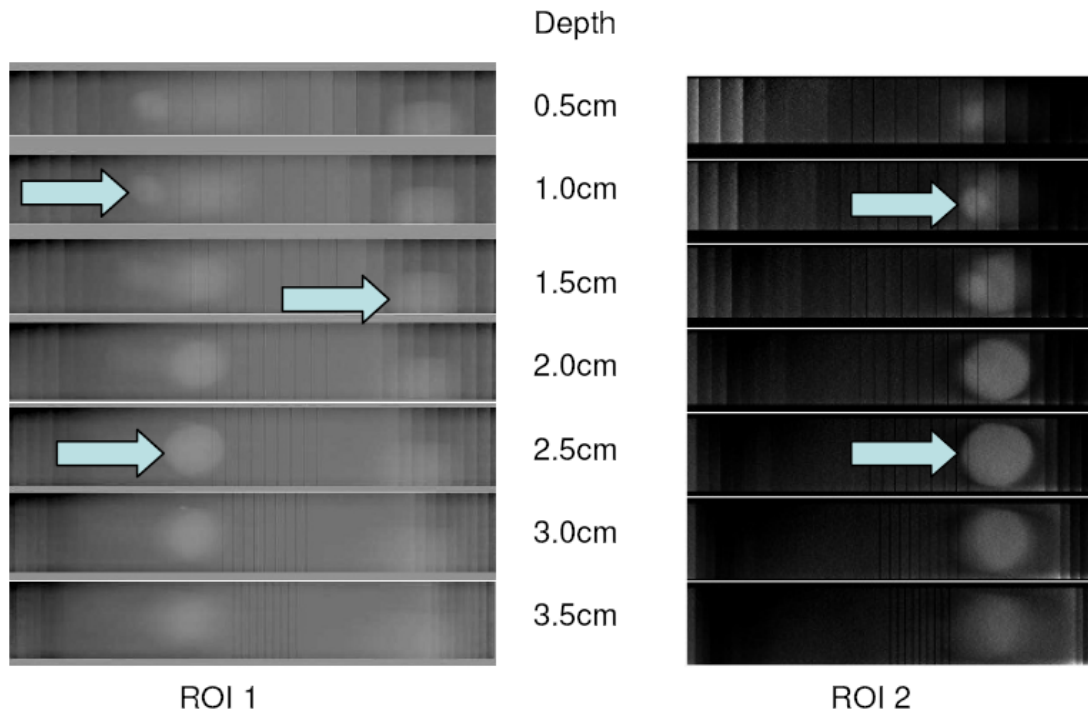


Figure 3.3 Reconstructed slices of the breast phantom obtained from the preliminary system. The slices through the breast phantom (from two different regions of interest) show how the overlapping masses in the raw projection images are resolved at their true depths. The vertical lines in the reconstructed slices are artifacts due to blank scan inconsistencies [3].

Thus the above imaging test using stationary MBFEX sources successfully established the great potential for tomosynthesis. It was evident that the system could be greatly improved – in terms of source stability, angular coverage and detector specifications – so as to make it a full-field stationary digital breast tomosynthesis (DBT) system. It is essential to set a full-scale system up in order to make a fair comparison to other commercial systems.

### 3.2 Stationary digital breast tomosynthesis system – Argus

#### 3.2.1 System overview

Our stationary digital breast tomosynthesis system based on carbon nanotube field emission x-ray sources, called Argus [4], consists of 25 individually addressable x-ray pixels, a flat-panel detector, and an interfacing computer. The system geometry is illustrated in figure 3.4.

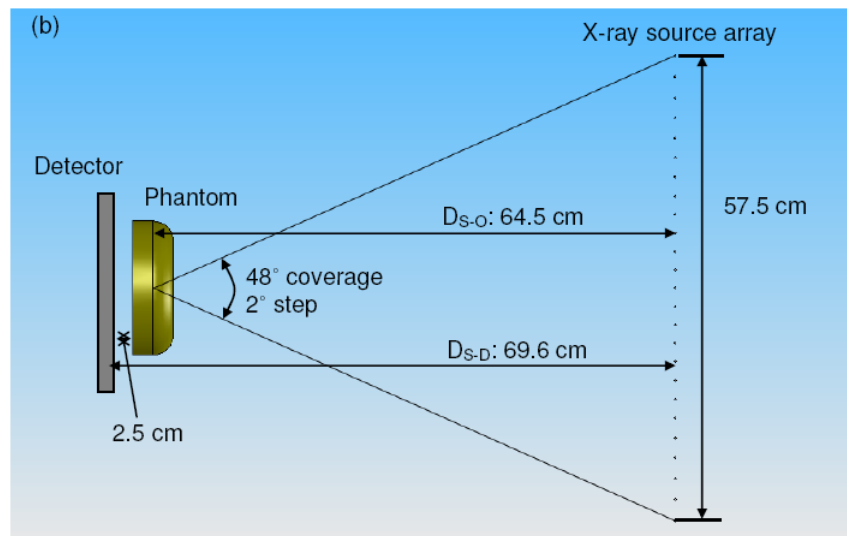


Figure 3.4 Argus system geometry showing the 25 x-ray sources and the flat panel detector [4].

The design of Argus is similar to other commercial systems. The flat panel detector used is Varian Paxscan 2520 which has a field of view of 19.5 cm x 24.4 cm. Under full resolution (pixel size is 0.127 mm), the detector readout time is 0.128 s whereas in the binned mode (pixel size is 0.254 mm), the readout time is 0.032 s. The 25 x-ray sources are evenly angularly separated and provide a total angular coverage of 48°. A picture of the assembled system is shown in figure 3.5. The system does not have any gantry rotation or movement and this enables us to reduce the scan time to as little as 9 s with sequential operation of the x-ray sources. The targeted total exposure is 80 mAs which is comparable to other systems as well.

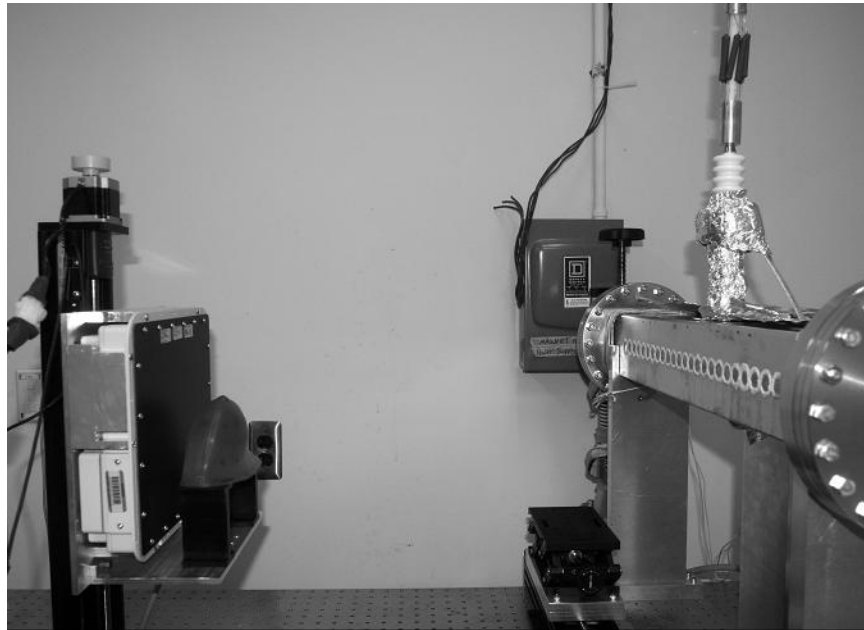


Figure 3.5 Photo of a completely assembled Argus system

The most important component is of course the cathodes. The system has 25 cathodes arranged in a linear fashion so as to form an iso-center at the center of the breast phantom. The first batch of cathodes used had CNTs covering an

elliptical area of dimensions 0.72 mm x 2.5 mm. A tungsten mesh is used as the gate to extract the electrons from the cathodes. Mica is used as the spacer between the cathode and the gate. There are two focusing stages the design of which were decided after extensive simulations and based on previous experience with the one-pixel micro-CT system. The anode is molybdenum and has a tilt angle of 16°. We used molybdenum as the window through which x-rays exit the chamber. Molybdenum serves both as a vacuum seal as well as a filter. A control circuit consisting of a computer and a field-programmable gate array (FPGA) data acquisition board enables us to synchronize the detector and the x-ray sources [4].

### **3.2.2 Comparison with other systems**

Argus is thus a truly stationary DBT system and it may well be superior to other systems. A comparison of the features in Argus with those in other systems is provided in table 3.1. Since other DBT scanners from major companies are still under development and are not yet fully clinically approved, the information provided in the table here and elsewhere has been obtained from associated published scientific literature.

	UNC: Argus	GE: Senographe 2000D	Siemens: Mammomat Novation	Hologic: Selenia
X-ray kVp, mA	25-35kVp, 10mA	25-30kVp, ~130mA	~28kVp, ~180mA	24-39kVp, ~100mA
Focal spot size	200 $\mu$ m	300 $\mu$ m	300 $\mu$ m + blur*	300 $\mu$ m + blur*
Target/filter	Mo/Mo	Mo/Mo, Rh/Rh	W/Rh	(Mo, W)/(Rh, Al)
Angle coverage	48 degrees	50 degrees	50 degrees	30 degrees
View numbers	25	11	25/49	11
Gantry motion	Stationary	Step and shoot	Continuous rotation	Continuous rotation
Flat-panel Detector	A-silicon	Cs:I a-silicon	Direct converter a-selenium	Direct converter a-selenium
Detector size	19.5 x 24.4 cm pixel pitch: 127 $\mu$ m	18.00 x 23.04 cm pixel pitch: 100 $\mu$ m	23.9 x 30.5 cm pixel pitch: 85 $\mu$ m	24 x 29 cm pixel pitch: 70 $\mu$ m (140 $\mu$ m for DBT)
Readout time	0.128s/0.032s	0.3s	0.6s/0.3s	0.6s
Integration time	0.32s	0.4s	0.2s	1.0s
Exposure time	0.32s	~0.1s	~0.03s	0.073s
Total scan time**	11.2s for 25 views	7s for 11 views	20s/39.2s for 25/49 views	18s for 11 views
Reconstruction method	ordered subsets convex (maximum likelihood)	ML-EM	FBP: filtered back projection	FBP: filtered back projection

\*: Additional focal spot blur due to the gantry movement during exposure.

\*\* : Total scan time = (view number) x (cycle time); cycle time = (readout time) + (integration time).

Table 3:1 Argus system specification and comparison with the other systems [4]

Since Argus is completely stationary, there is no undesirable vibration due to gantry motion. The system enables us to utilize the x-ray power more efficiently and shorten the imaging time because the x-ray exposure time matches the detector integration time. The system resolution, which is often limited by the detector resolution, is still better than the other systems.

### 3.2.3 Required system characterization

It is very important that an imaging system be completely characterized before any actual imaging is done. The usual quality assurance tests for x-ray systems include estimation of the focal spot size, the system resolution, calibration of dose and calibration of geometry. In our case, each of the above

tests is even more significant because of the presence of multiple x-ray sources and the need to establish that their performance is uniform across all x-ray pixels.

The next chapter is devoted to a description of the various methods adopted for the characterization of Argus while Chapter 5 gives details about the image reconstruction technique adopted for reconstructing the images from our stationary DBT system.

## References

1. Lipton MJ, Higgins CB, Farmer D, et al.: Cardiac imaging with a high-speed cine-CT scanner: preliminary results. *Radiology* 152(3): 579-582, 1984.
2. Zhang J, Yang G, et al.: Stationary scanning x-ray source based on carbon nanotube field emitters. *Appl. Phys. Lett.* 86, 184104, 2005.
3. Lalush DS, Quan E, et al.: Tomosynthesis reconstruction from multi-beam x-ray sources. *Proc. IEEE International Symposium on Biomedical Imaging*, 2006.
4. Yang G, Rajaram R, et al.: Stationary digital breast tomosynthesis system with a multi-beam field emission x-ray source array. *Proc. of SPIE, Medical Imaging*, 6913, 69131A, 2008.

## 4 Characterization

### 4.1 Focal spot size

In an x-ray chamber, the anode angle is defined as the angle that the target makes with the central axis of the x-ray tube output direction. The true focal spot size is the area on the anode that is struck by the electrons from the cathode. The effective focal spot size is the length and the width of the emitted x-ray beam as projected along the central axis of the x-ray tube. This is illustrated in figure 4.1. The anode angle is usually between 7° and 20°, so the projected focal spot is less than the true focal spot [1]. If the anode angle is  $\theta$ , the true and the effective focal spot size are related by the line focus principle:

$$\text{Effective focal length} = \text{True focal length} * \sin \theta$$

The true focal spot size is determined by cathode dimensions and other focusing or biasing circuits present in the system and is independent of the anode angle.

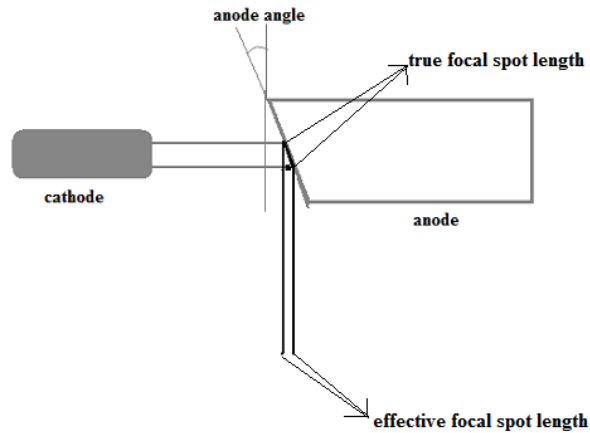


Figure 4.1 True versus effective focal spot size.

Anode angle is the angle of the target with respect to the central beam of x-rays. The projected focal spot size is determined by the line focus principle.

While a smaller anode angle will yield a smaller effective focal spot for the same actual focal area by reducing the projected length by the sine of the angle (the projected width does not change), it will also limit the size of the usable x-ray field because of the attenuation of x-rays parallel to the anode surface. The optimal choice of the anode angle often depends on the application. It is important to remember that the focal spot size has a major influence on the spatial resolution of the system, particularly when there is a large magnification. Common tools used to measure focal spot size are the slit method, the pinhole method and the resolution bar pattern. The pinhole method uses a very small circular aperture (10-30  $\mu\text{m}$ ) in a thin, highly attenuating metal disk. The slit camera consists of a small slit made of a highly attenuating material mounted on a support. The image of the pinhole or the slit is used to estimate the effective focal spot size.

#### 4.1.1 Initial imaging test and results

The first batch of cathodes used in our stationary DBT system Argus was elliptical in shape, with dimensions of 2.5 mm along the major axis and 0.72 mm along the minor axis. Simulation results predicted that with the combined effect of the two focusing stages in the system, there would be a demagnification of approximately 3.6 of the cathode size resulting in the actual (true) focal spot size on the anode being about 0.694 mm along the major axis and 0.2 mm along the minor axis. Since the major axis would then be projected because of the anode angle, this would result in an effective isotropic focal spot size of about 200  $\mu\text{m}$ .

In order to measure the focal spot size for all the 25 x-ray pixels in Argus, it was decided to adopt the slit method. The protocol as described in European Standard EN 13543-5 [2] that describes the measurement of the effective focal spot size in micro and mini x-ray tubes was followed. This method is applicable to cathode sizes up to 300  $\mu\text{m}$  and is based on an indirect estimation of the focal spot size using the geometric unsharpness. The test object or phantom used was a 1 mm tungsten cross wire mounted on a suitable support. This phantom was placed as close to the source as possible to achieve the large magnification necessary for the measurement as specified in the standard. The set-up is as shown in figure 4.2.

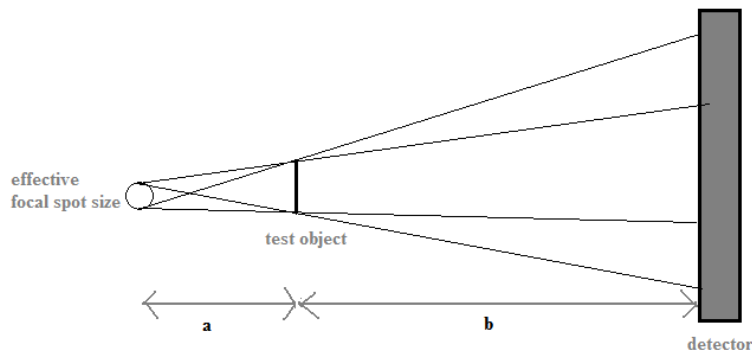


Figure 4.2 Estimation of the effective focal spot size by using the geometric unsharpness method. The magnification  $(a+b)/a$  is made as large as possible by placing the test object very close to the source [2].

A schematic of the cross wire phantom that we designed and used for the purpose is shown in figure 4.3 along with a typical projection image.

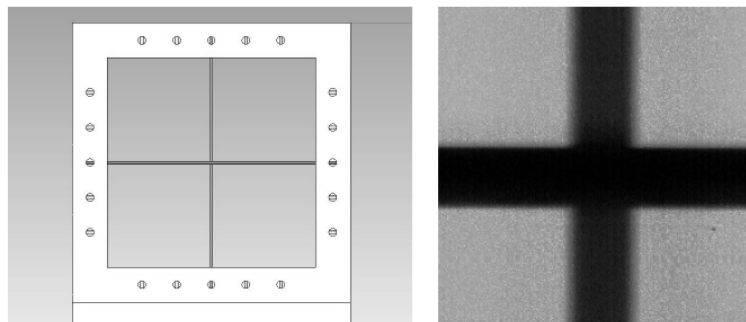


Figure 4.3 Design of the cross-wire phantom used to estimate the focal spot size (left) and a single projection image of the phantom (right)

Once the image is obtained, the procedure outlined in the standard was followed in order to estimate the focal spot size along the projected side (that side of the true focal spot that is projected by the anode angle and which is termed the long side) and the un-projected side (which is the short side). The entire procedure was repeated for various combinations of voltages on the first and the second focusing stages in order to find the right set of values at which

the focal spot size is the smallest. Our experimental results indicated that the gate voltage had little effect on the focal spot size. The results from nine pixels are shown in table 4.1. It can be seen that the typical focal spot size is isotropically 0.2 mm with an uncertainty of 0.02 mm [3].

X-ray source #	$F_x$ : parallel to x-ray source array	$F_y$ : perpendicular to x-ray source array
1	0.20mm	0.20mm
2	0.20mm	0.17mm
3	0.18mm	0.19mm
4	0.19mm	0.19mm
5	0.20mm	0.19mm
6	0.19mm	0.17mm
7	0.18mm	0.17mm
8	0.19mm	0.19mm
9	0.18mm	0.19mm

Table 4:1 Focal spot sizes along the long and the short sides of nine x-ray beams in Argus.

#### 4.1.2 Pinhole imaging and results

From literature and discussions with clinical experts, we figured that resolution in terms of focal spot size may not be as much of a concern in a tomosynthesis scenario as the total scan time. In that case, it is possible to increase the current output of a CNT cathode simply by increasing its size. An increased current from each one of the 25 x-ray pixels can help reduce the total scan time significantly. In order to do this, a batch of circular cathodes of diameter 3 mm was fabricated and assembled in the system. As per simulation results and earlier experience, the expected effective focal spot size is 600  $\mu\text{m}$  (short side) x 170  $\mu\text{m}$  (long side). Since the European standard is only valid for focal spot sizes up to 300  $\mu\text{m}$ , a different method that might be more commonly

used for diagnostic x-ray tubes was to be adopted. The pinhole method was our method of choice.

The pinhole phantom is a 5 mm diameter disk made of an alloy of gold and platinum. It contains a 100  $\mu\text{m}$  pinhole that is 500  $\mu\text{m}$  long. This is illustrated in figure 4.4. This commercial phantom ([www.oegussa.at](http://www.oegussa.at)) was mounted within one hole of many on a large disk. The other holes are of varying diameters. The entire disk is mounted on a goniometer so that fine angular adjustment is possible. The goniometer with the phantom was placed as close to the x-ray source as possible and used the holes of larger diameters for initial alignment. The detector is placed so as to ensure a magnification of about 4 as suggested in the National Electrical Manufacturers Association standard [4] (for pinhole imaging).

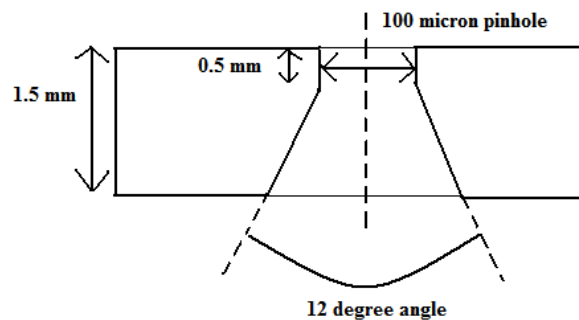


Figure 4.4 The pinhole phantom with the 100  $\mu\text{m}$  pinhole.

After initial alignment it becomes easier to align the 100  $\mu\text{m}$  pinhole in the path of the x-ray beam. An image of the pinhole obtained using the central x-ray pixel for a particular combination of focusing voltage is shown in figure 4.5.

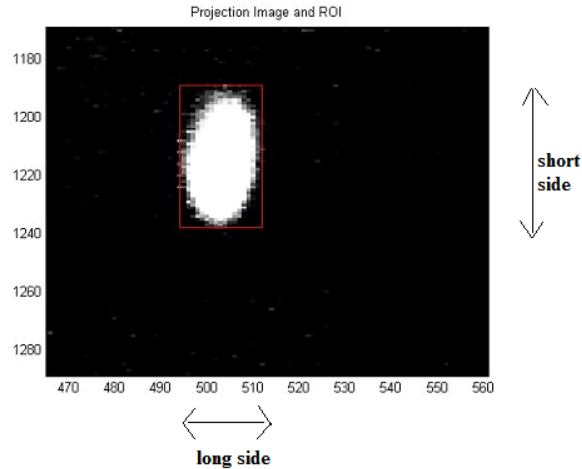


Figure 4.5 An image of the pinhole.

From the intensity distribution of the pinhole, we estimated the focal spot size as follows: The intensity distribution along the long and the short sides are integrated separately across columns or rows as the case may be. The integrated intensity is then plotted as a function of the number of pixels. This is illustrated in figure 4.6. The integrated intensity data was then fitted to a Gaussian function. As per industry standard, the 80% area under the Gaussian curve is taken as the effective focal spot size. The 80% value is given in terms of the standard deviation of the Gaussian,  $\sigma$ , as  $1.28 \cdot \sigma$ . This value was then expressed in terms of distance units and scaled for magnification to yield the effective focal spot size.

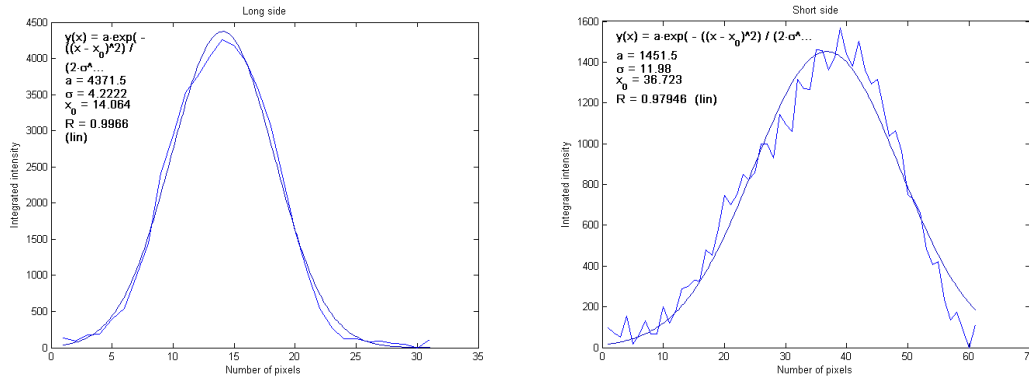


Figure 4.6 Integrated intensity of the long and the short side of the effective focal spot.

Overlaid on the raw data is a Gaussian fit to the data. The  $\sigma$  of the fitted Gaussian is used to calculate the effective focal spot size.

The above procedure was repeated for various combinations of voltages on the two focusing stages in order to find the optimum set of focusing voltages. This set of focusing voltages was then used to verify the effective focal spot sizes of the other x-ray pixels. The focal spot sizes obtained for the central x-ray pixel are shown in table 4.2.

Focusing voltages (V)	1200	1300	1400	1500	1600	1700
900	0.1708x0.5719	0.1548x0.5195	0.147x0.4951	0.1469x0.4847	0.1496x0.4903	0.1511x0.4938
1000	0.1708x0.5445	0.155x0.5277	0.1499x0.5011	0.1456x0.4718	0.1507x0.4749	0.153x0.4801
1100	0.1587x0.5023	0.1587x0.5099	0.1487x0.4915	0.1496x0.4904	0.1492x0.4964	0.1529x0.4883

Table 4:2 Focal spot sizes for various combination of focusing voltages.

Focal spot sizes in units of 'mm' are estimated using the pinhole method for various combinations of focusing voltages. The focal spot size on the long side is about 0.15 mm while on the short side is about 0.50 mm.

Thus, the pinhole method enabled us to measure the focal spot size. It can be seen from the experimental results that the focal spot sizes in the long and the short side are approximately 0.15 mm x 0.50 mm. The uncertainty in the measurements is about 0.02 mm. While the values are comparable to the values predicted by simulation (0.17 mm x 0.60 mm), the difference could be attributed to variation in the demagnification factor. In addition, simulation assumes a parallel anode whereas there is an anode angle of 16° in the experimental set-up.

## **4.2 System resolution**

Spatial resolution of a system determines how good it is in producing images of very small objects [5-7]. Many different physical mechanisms can cause loss of resolution in imaging systems. In other words, these mechanisms cause the sharp point input to the imaging system to spread and create a blurred version of the input. The lateral spread of the output itself is a measure of the spatial resolution of the system and is measured in terms of the point spread function (PSF), the line spread function (LSF), or the edge spread function (ESF). These functions describe blurring caused in an imaging system in the spatial domain. Another way of describing resolution mathematically is by the use of functions in the frequency domain [1, 8-12]. The Fourier transform is the mathematical operation that allows the conversion from the spatial domain to the frequency domain.

### 4.2.1 Modulation Transfer Function

The modulation transfer function or MTF is a graphical description of the resolution capabilities of an imaging system. A typical MTF is illustrated in figure 4.7. The x axis of the MTF plot represents the size of the object. Low spatial frequencies correspond to big objects while higher frequencies correspond to smaller objects. For most imaging systems, the MTF is close to 1 at low spatial frequencies and gets smaller at higher spatial frequencies.

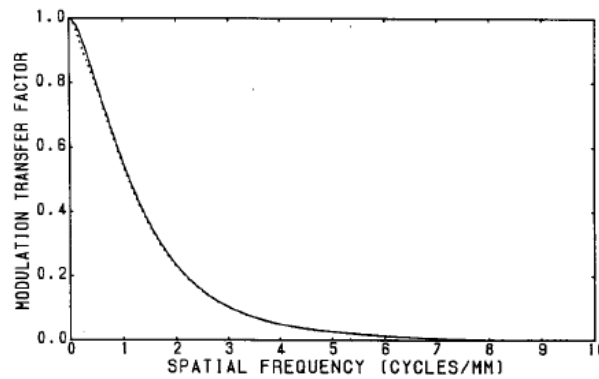


Figure 4.7 Spatial resolution in terms of modulation transfer function (MTF).

The MTF is a plot of the contrast transfer properties of an imaging system as a function of the size of the object.

### 4.2.2 Method for determining the MTF

To determine the MTF of our system, we have adopted the method described by Fujita, et al. [13]. This is a method for measuring the MTF by taking the Fourier transform of a “finely sampled” line spread function (LSF). The LSF is obtained from the image of a slightly angulated slit in the spatial domain. The small angulation of the wire helps by providing an effective sampling distance that is much smaller than the original sampling distance of the imaging system,

thus avoiding the effects of aliasing. For example, with a slit that is placed at an angle less than  $2^\circ$  perpendicular to the scan direction, the following four LSFs are obtained from locations A, B, C and D as shown in figure 4.8 (a & b). While each LSF has five discrete data with the same sampling distance, they can be combined to generate a composite finely sampled LSF with a smaller sampling distance as shown in figure 4.8 (c). The Fourier transform of the composite LSF gives the presampling MTF value of the digital imaging system.

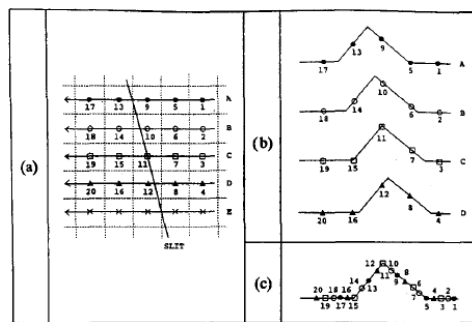


Figure 4.8 Generation of a composite LSF.

On the left is a slightly angulated slit whose LSFs corresponding to various alignments (b) are used to generate a composite “finely sampled” LSF (c). The Fourier transform of the composite LSF gives the MTF of the system. [13]

### 4.2.3 Experiment

In the phantom that was designed for the purpose of estimating the MTF, a  $100\ \mu\text{m}$  tungsten wire was placed inside a plastic holder so that the vertical angle of the wire is less than about  $2^\circ$ . The phantom was then placed on the stage at the same distances from the source and the detector that would normally be used for breast imaging. The combination of focusing voltages that gave the smallest focal spot size was then used to obtain images of the MTF phantom. The MTF due to the central pixel and two extreme x-ray pixels were

measured in this manner. Once the image was obtained, a sufficiently large region of interest (ROI) encompassing the wire was chosen to yield the oversampled LSF. The angle of the wire was estimated from the ROI and used to generate a composite LSF. A Gaussian was fitted to the composite LSF after subtraction of the background. This Gaussian LSF was then Fourier transformed and normalized to give the MTF. The MTF at 10% is quoted in units of lp/mm as the presampling MTF of the digital imaging system. Since the effective focal spot size in our system is anisotropic, the above experiment was repeated to find the MTF in the other direction by placing the phantom horizontally on the stage.

Since it is important to determine and separate out the contributions of various components of the imaging system to the total presampling MTF, the detector MTF was also measured by placing a slightly angulated 100  $\mu\text{m}$  tungsten cross wire directly on the surface of the detector. This enabled us to correlate the focal spot size of the CNT cathodes with the corresponding MTFs.

#### **4.2.4 Results**

The MTF for three representative x-ray sources was measured by the above method by placing the phantom on the stage to ensure a magnification of about 1.1. We chose the central x-ray source as well as two of the extreme sources to characterize the spatial resolution. It is known that in the other clinical tomosynthesis systems under development, either the source or the detector or both are moving during the finite x-ray exposure period. This motion causes a degradation of the MTF compared to a stationary case [14]. Choosing the

sources that are at the extreme ends of the chamber (similar to the full range of c-arm motion in the other DBT systems) will allow us to make a more useful and fair comparison of our system MTF with that of the other systems.

The region of interest chosen from the image of the phantom, the binned LSF and the fitted Gaussian are shown in figure 4.9 for the central x-ray source (# 13).

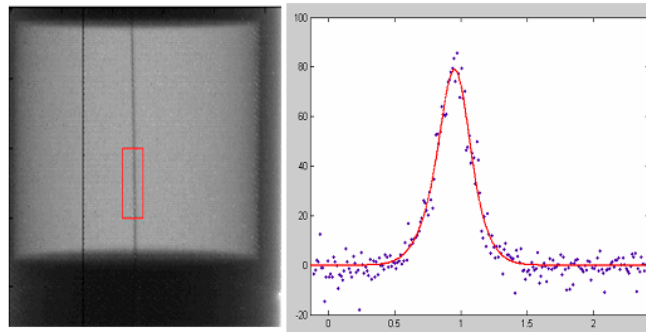
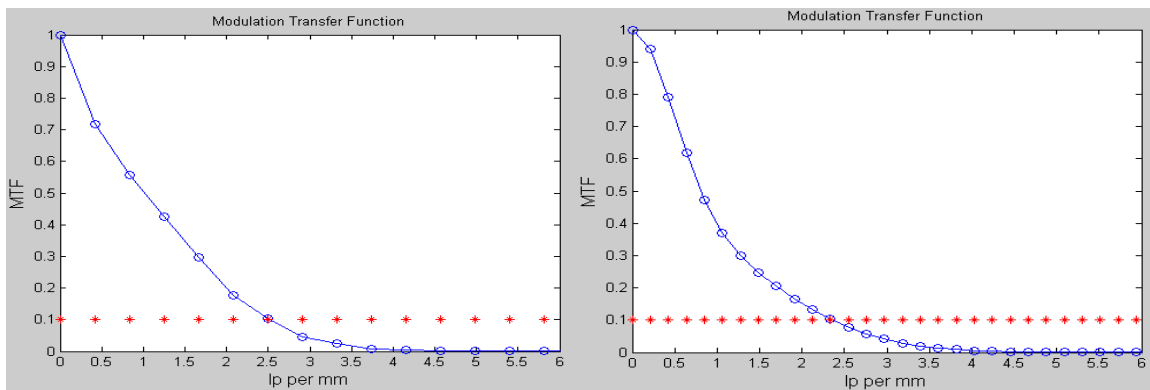


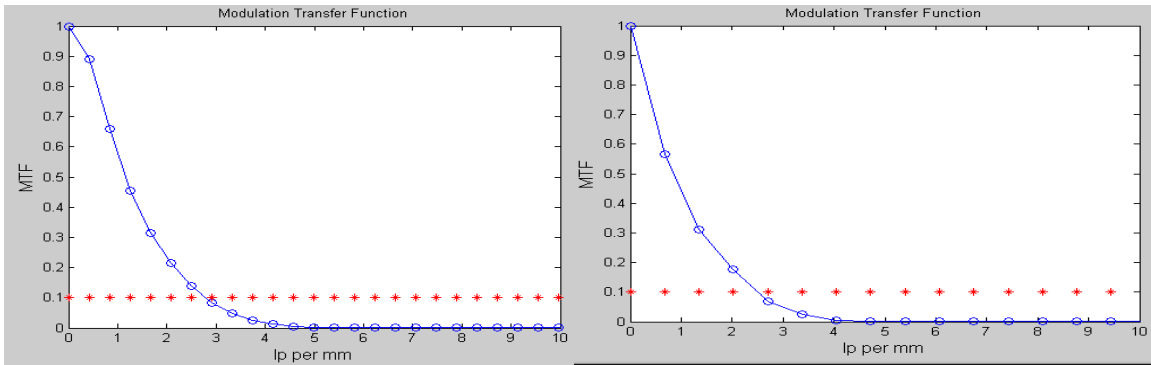
Figure 4.9 Calculation of the MTF.

The region on interest chosen to calculate the MTF is shown on the image of the phantom. On right is the binned LSF (data points in blue) fitted to a Gaussian (red).

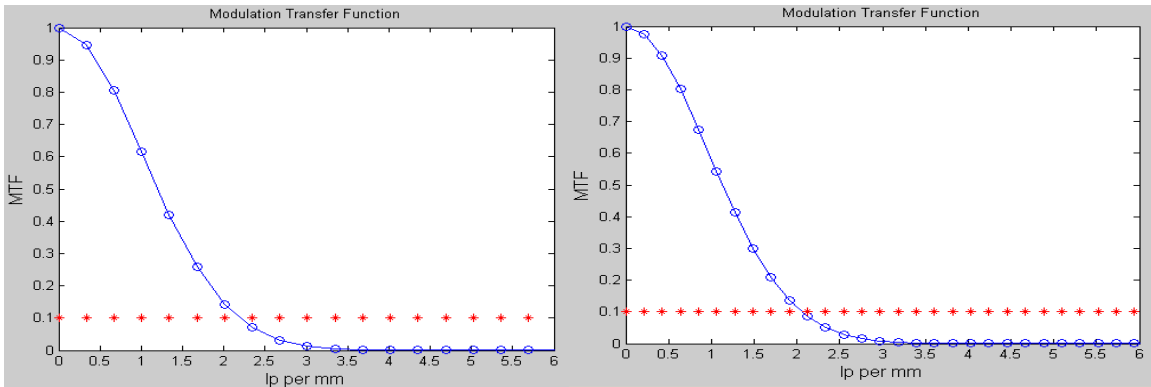
The calculated MTF for the three x-ray sources along the long (projected) and the short side are shown in figure 4.10. It is evident that the system MTF on the long side is better than the MTF for the short side across the three x-ray sources that were tested.



(a) MTF on the long side (left) and on the short side (right) for x-ray source 1



(b) MTF on the long side (left) and on the short side (right) for x-ray source 13



(c) MTF on the long side (left) and on the short side (right) for x-ray source 25

Figure 4.10 MTF plots for the three x-ray sources.

The detector MTF measured by placing the wire directly on the surface of the detector is shown in figure 4.11 corresponding to both the long and the short side of the cathode.

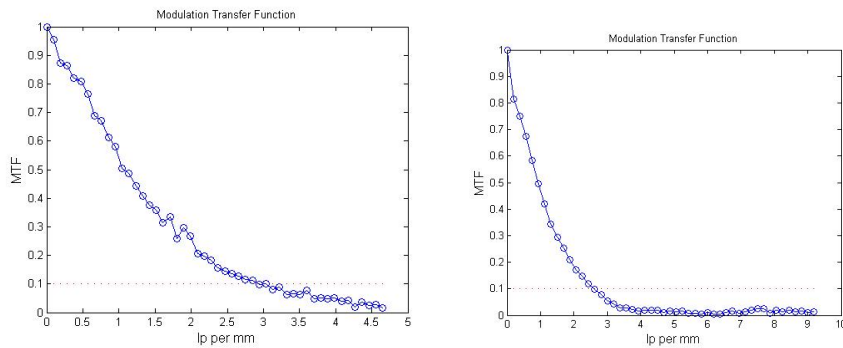


Figure 4.11 Plot of the detector MTF.

The detector MTF is given along the long side (left) and along the short side (right) of the cathode

#### 4.2.5 Discussion of results

The system MTF values along the long and the short sides of the cathode for each of the three x-ray sources tested are summarized in table 4.3. The optimum effective focal spot size was estimated to be about 0.145 x 0.490 mm. The MTF of the Varian Paxscan detector as quoted by a technical representative of the company is 3.1 lp/mm for the 1x1 binning mode. We have measured the detector MTF along the long side to be 3 lp/mm and the detector MTF along the short side to be a little less at about 2.7 lp/mm. So, a detector MTF of 3.1 lp/mm actually corresponds to a spatial resolution of  $(0.5/3.1) = 0.161$  mm even though the detector pixel size is given to be 0.127 mm.

The contribution of the effective focal spot size at the detector is  $(M-1)*FSS$ , where M is the magnification used and FSS is the effective focal spot size. Based on the experiment, we have  $M=1.1$  so that the effective focal spot size contributes about 10% to the system MTF.

X-ray source number	10% MTF along the long side in lp/mm	10% MTF along the short side in lp/mm
1	2.5	2.3
13	2.8	2.4
25	2.3	2.1

Table 4:3 MTF for the different x-ray beams.

The effective FSS along the long side is 0.15 mm so that we have at the detector a resolution of  $(0.161 + 0.015) = 0.176$  mm. This is equivalent to a

limiting MTF of  $0.5/0.176 = 2.85$  lp/mm. Similarly, the effective FSS along the short side is 0.5 mm so that we have at the detector a resolution of  $(0.161 + 0.05) = 0.21$  mm. This is equivalent to a limiting MTF of  $0.5/0.21 = 2.4$  lp/mm. The MTF values obtained for the central x-ray source along the long and the short sides are very close to the limiting values. The extreme x-ray sources 1 and 25 are at an angle of  $24^\circ$  compared to the central source. The x-rays from these sources have a larger path length, that is they travel an extra distance of about  $\cosine 24^\circ (= 0.91)$  compared to x-rays from the central source. This causes an increase in the spatial blur in the detector scintillator screen and introduces a degradation of about 10% in the system MTF for the extremely located x-ray sources as seen in table 4.3. Thus, we can conclude that it is really the detector that is limiting the resolution and an improved detector resolution will allow us to achieve better system spatial resolution.

It is important that in the estimation of the MTF, the oversampling angle is calculated accurately. A modification to the existing program was implemented to calculate the angle by fitting a straight line to the minimum intensity values corresponding to the wire from every row in the selected region of interest. In addition, care should be taken to fit a good Gaussian to the line spread function before obtaining the Fourier transform. Flat-field corrected images are recommended to be used for the MTF estimation. In any case, the Gaussian fit should be able to account for any non-uniformity in the background. The thickness of the wire used in the method should in general be smaller than the detector pixel pitch. The phantom containing the wire should be a low attenuating

material and at the same time be able to hold a wire that is long enough to cover as much of the field of view of the detector as possible.

### **4.3 Geometry Calibration**

The purpose of geometric calibration in a cone beam tomographic system is to estimate the geometry parameters of the system that would be required for accurate and artifact-free image reconstruction. Often, the geometric calibration method is tightly linked to the algorithm hypothesis used in the particular set-up [15]. There are many methods for geometric calibration such as alignment [16], projection matrix estimation [17] and global estimation methods using sets of projection images [18, 19]. Accurate scanner calibration is required in order to avoid reconstruction artifacts [15] and even small errors in one geometric parameter can have visible bad effects on the reconstructed image.

#### **4.3.1 Method**

The method that was used to calibrate the geometry of the DBT system is an analytic method based on identification of ellipse parameters as first described by Noo, et al [20]. In this method of calibration, a simple phantom consisting of two highly attenuating ‘point’ objects is used. Multiple projection views of the phantom are obtained as it rotates over the entire 360°. It is easy to see that as each object rotates, it traces an ellipse on the detector. From a parametric description of the ellipse, it is possible to analytically derive the geometry parameters through the use of explicit formulas that link the two. In

general, seven parameters are sufficient to calibrate a cone beam scanner where the source and the detector move in a circle [15]. In this method, it is assumed that the detector is parallel to the rotation axis and the remaining six geometry parameters are estimated.

It is easy to understand the geometry of the system by using a Cartesian system of coordinates where the z-axis is along the rotation axis and the x-axis is along the perpendicular line from the source to the rotation axis. This is shown in figure 4.12.

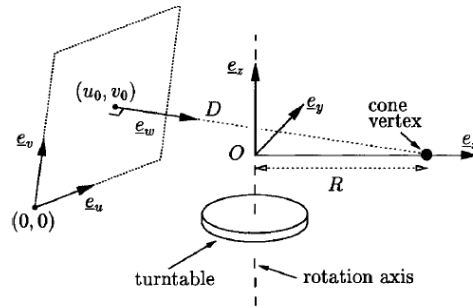


Figure 4.12 Illustration of the scanner geometry for estimation of geometric parameters [20]

In figure 4.12,  $R$  is the distance from the cone vertex to the rotation axis and  $D$  is the shortest distance from the vertex to the plane of the detector. If  $e_w$  is the unit vector that specifies the direction of the shortest line connecting the detector to the source,  $\theta$  is the co-polar and the  $\varphi$  is the azimuthal angle in the  $(x, y, z)$  plane while  $\eta$  is used to define the two orthogonal unit directions  $e_u$  and  $e_v$  along the detector plane. The orthogonal projection of the source on the detector plane is represented by  $(u_0, v_0)$ .

In this method, the assumption is that  $\theta = 0$  and so the method estimates the remaining six geometry parameters, namely  $R$ ,  $D$ ,  $\eta$ ,  $\varphi$  and  $(u_0, v_0)$ . In our case, the most important parameters needed for tomosynthesis image reconstruction (reconstruction is described in Chapter 5) are the source locations in space. Each of the 25 sources in our system is fully described in  $(x, y, z)$  space by  $(u_0, v_0)$  and  $D$ . The value of  $\eta$  should be as small as possible as it describes an undesirable detector tilt. The value of  $\varphi$  should reflect the angular location of the x-ray source, that is,  $\varphi = 0^\circ$  for the central x-ray beam whereas  $\varphi = 24^\circ$  for the extremely located x-ray sources.

Earlier methods relied on non-linear parameter estimation, required reasonable initial estimates and had issues of uniqueness and stability. Noo's method [20] avoids those difficulties by introducing an intermediate set of parameters to analytically derive the geometry parameters from the ellipse parameters. Here,  $N$  uniformly spaced projection images of a calibration phantom consisting of two point objects are obtained over  $360^\circ$ . The two point objects are placed as far away from rotation axis as possible with one object on each side of the source plane. System calibration is done in three steps:

1. Determine whether rotation axis is projected onto the detector and find  $\eta$ .
2. The cone beam projection of the two point objects yields two ellipses on the detector. The projection data are used to determine the ellipse equations. A fitting is done on the two ellipses and the ellipse parameters are estimated.

3. The ellipse parameters and the distance between the two point objects are used to set up equations for the unknowns. These equations are then solved analytically to yield the geometry parameters.

#### **4.3.2 Testing**

The calibration method described above was implemented in Matlab (The Mathworks™). Our implementation basically followed the three steps outlined above. The two balls are segmented out based on a threshold intensity value. The centroids of the projection of the two balls are identified for all projection views. A least squares ellipse fit is done on the centroids to derive the ellipse parameters. Using the intermediate equations given in the reference [20], the geometric parameters are calculated from the ellipse parameters. In order to validate the above geometric calibration method as applied to our stationary DBT system, it was first tested using computer simulations. The simulation test was done in two parts: 1) simulate projection images of the two-ball phantom based on certain geometry parameters, test the calibration method implemented in Matlab on the simulated images, extract the geometry parameters, compare the calibrated values with the input (designed) values. 2) Reconstruct a CIRS type phantom with the calibrated set of values as well as with the designed set of values to demonstrate differences, if any, between the two.

The calibration method was then applied to preliminary experimental images of a home-made two-ball phantom. For the initial calibration, nine x-ray sources in Argus were used to generate either 6 or 12 projection images of the

phantom. For the second test, the geometries of the central x-ray beam and the two extreme x-ray beams were calibrated first and then the calibration was validated by repeating for two other x-ray beams in between. More details on the simulation tests and the experiment are given in the following sections.

#### **4.3.2.1 Simulation Tests & Results**

For the first simulation test, a calibration phantom containing two highly attenuating balls embedded in a low-attenuating background was created using a NURBS modeling software called Rhinoceros®. The balls are each 2 cm in diameter and if the center of the phantom is taken as (0, 0), the centers of the balls are located at (-2, 2) and (2, -2). There are nine equally spaced x-ray sources whose offset distances from the center are listed in table 4.4. These are the theoretical (designed) locations of the sources along the direction of the chamber (x-direction) and are designated as  $u_0$ . The theoretical  $v_0$  (offset along the direction perpendicular to the chamber – the y-direction) for all the sources is zero. The phantom was placed close to the detector so that the magnification is nearly 1. The source to detector distance (SDD) was fixed at 69.06 cm (thus SDD will be along the z-direction). For each of the nine sources, thirty projection images of the calibration phantom were obtained over full rotation. A single simulated projection image from the central x-ray beam is illustrated in figure 4.13. All the simulated projection images were then extracted out and the geometric calibration technique which had been implemented in Matlab was tested on the simulated images. The relevant geometric parameters are ( $u_0, v_0$ )

and the SDD. The values of these parameters obtained from calibration are listed together with the theoretical values in table 4.4. From the table, it is evident that the difference between the calibrated and the theoretical  $u_0$  values is about 2 mm (at worst) while the difference between the calibrated and theoretical  $v_0$  values is about 0.7 mm (at worst). The largest difference between the calibrated and designed SDD is about 1.2 cm, however, this variation is still less than 2 % of the actual SDD.

For the second part of the simulation test, a CIRS type phantom as described in Chapter 2 was set up and noise-free projection images of the phantom were simulated using the designed geometric parameters. The projection views were then reconstructed using our iterative reconstruction algorithm (described in Chapter 5). The reconstruction was first done with the designed geometry values and then repeated using the experimentally calibrated geometry values. The same slice containing the features of interest were extracted from both reconstructions and analyzed for differences in contrast and/or resolution.

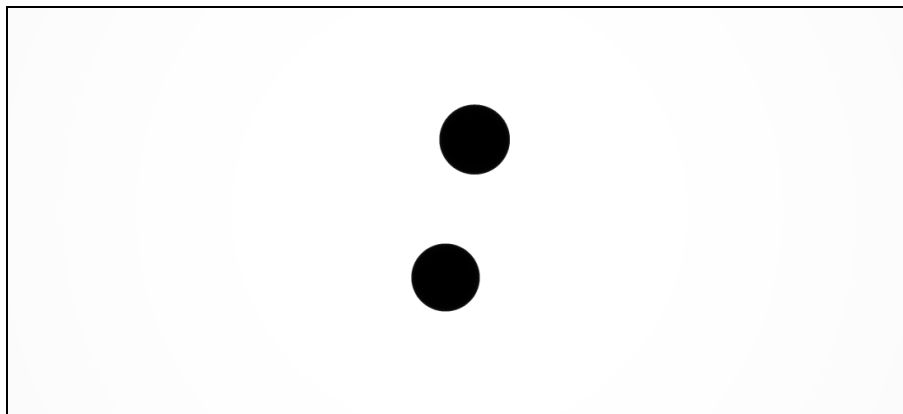


Figure 4.13 A single projection image of the simulated calibration phantom. Image shows the two highly attenuating balls in a low-attenuating background.

Exp. $u_0$ (mm)	Theory $u_0$ (mm)	$\Delta u_0$ (mm)	Exp. $v_0$ (mm)	Theory $v_0$ (mm)	$\Delta v_0$ (mm)	Exp. SDD (mm)	Theory SDD (mm)	$\Delta$ SDD (mm)
286.1	287.4	1.3	0.013	0	-0.013	678.2	690.06	11.86
213.84	215.55	1.7	-0.061	0	0.061	688.7	690.06	1.36
142.9	143.7	0.74	0.14	0	-0.14	683	690.06	7.06
71.56	71.85	0.28	0.09	0	-0.09	690.3	690.06	0.24
0	0	0	0	0	0	680.5	690.06	9.56
-72.89	-71.85	1.04	-0.37	0	0.37	688.7	690.06	1.36
-143.6	-143.7	-0.10	0.38	0	-0.38	683.4	690.06	6.66
-213.41	-215.55	-2.14	0.72	0	-0.72	690.9	690.06	0.84
-288.4	-287.4	1.04	-0.05	0	0.05	681.6	690.06	8.46

Table 4:4 Calibrated and theoretical geometric parameters.

The phantom was imaged at a magnification 1. The difference between the two sets ( $\Delta$  = theory – experiment) is also included.

A slice showing the masses, fibers and calcifications, reconstructed using the experimentally calibrated geometric parameters is shown in figure 4.14 next to the same slice from the reconstruction using theoretical parameters. The image quality in the two cases appears to be similar in general but a closer look reveals that the calcifications are slightly smeared out, especially the smallest and the second smallest set of calcifications, in the calibrated reconstruction. The fibers also seem to be fuzzier in the calibrated case than in the theoretical case.

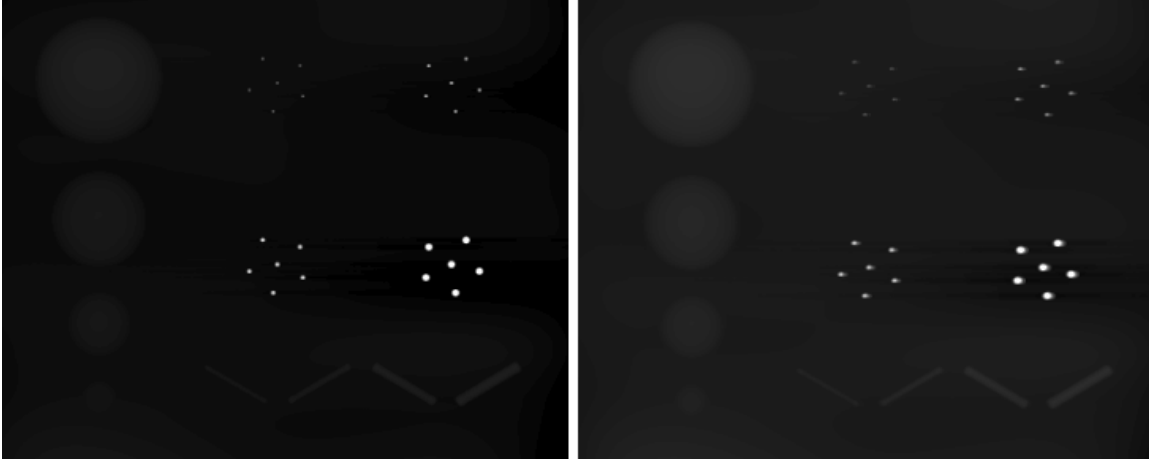


Figure 4.14 Reconstruction using the theoretical and the calibrated geometric parameters.

On left is the slice reconstructed using theoretical geometric parameters and on the right is the same slice reconstructed using the calibrated geometric parameters. The two images were separately windowed and zoomed to show the objects of interest and the difference in gray scale is most likely a result of minor variations in the windowing.

The comparison is further illustrated in figure 4.15 by taking two horizontal profiles through the central object, one profile for the top two sets and another profile through the bottom two sets of calcifications. From the profiles, it is evident that there is only a very negligible difference in intensity in the calibrated case compared to the experimental case, and even that is more so for the smallest calcifications. In addition, there is a small spread (resolution) associated with the tail side of the calibrated profile, which again is worst for the smallest calcifications.

Similar profiles taken through the fibers in both sets of reconstructed slices did not show any difference in intensity or the resolution. Same was the case with the masses. It is fair to conclude that the reconstruction is not very sensitive to small variations in the source locations or the source to detector distance.

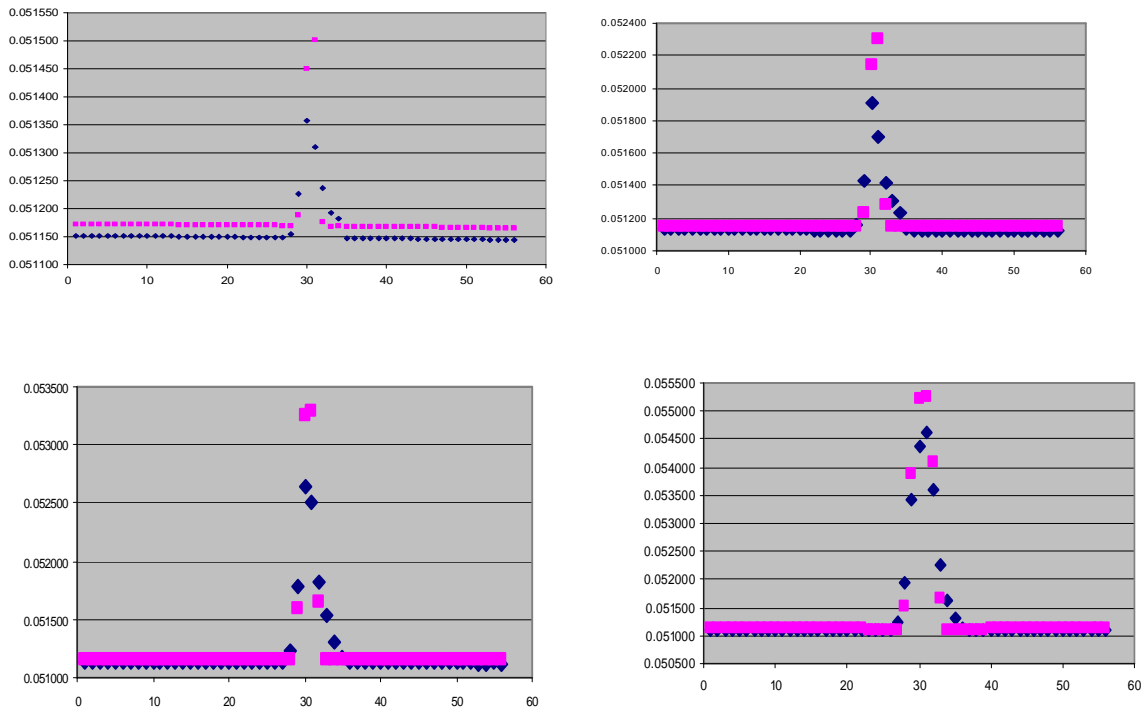


Figure 4.15 Intensity profiles for the theoretical and the calibrated reconstruction sets.

Horizontal profiles taken through the central object for the two sets of calcifications at the top (top) and through the central object for the two sets of calcifications at the bottom (bottom) from the theoretical reconstruction (purple squares) and the from the calibrated reconstruction (blue diamonds)

It was still important to test the calibration technique to see if it could provide more accurate results. For this, projection images of the two ball phantom were simulated under a magnification of 2. Thirty projection views of the phantom were obtained for each of three equally spaced sources. Following the same procedure as before, the geometric parameters were calculated from these images. The results are in table 4.5.

Exp. $u_0$ (mm)	Theory $u_0$ (mm)	$\Delta u_0$ (mm)	Exp. $v_0$ (mm)	Theory $v_0$ (mm)	$\Delta v_0$ (mm)	Exp. SDD (mm)	Theory SDD (mm)	$\Delta$ SDD (mm)
47.9	46.9	1.0	0.05	0	-0.05	690.9	690.06	-0.84
0	0	0	0	0	0	690.4	690.06	-0.34
-47.9	-47.45	-0.45	0.03	0	-0.03	690.2	690.06	-0.14

Table 4:5 Geometry parameters for magnification 2.

Listed above are the calibrated values and the theoretical values of the geometric parameters when the phantom was imaged at a magnification 2. The difference between the two sets ( $\Delta = \text{theory} - \text{experiment}$ ) is also included.

Table 4.6 shows results of the calibration when a phantom with smaller beads was imaged under similar conditions (bead size was reduced to 1/10<sup>th</sup> its original size).

Exp. $u_0$ (mm)	Theory $u_0$ (mm)	$\Delta u_0$ (mm)	Exp. $v_0$ (mm)	Theory $v_0$ (mm)	$\Delta v_0$ (mm)	Exp. SDD (mm)	Theory SDD (mm)	$\Delta$ SDD (mm)
47.5	47.9	0.4	0.05	0	-0.05	689.5	690.06	0.56
0	0	0	0	0	0	689	690.06	1.06
-46.1	-47.9	-1.8	-0.02	0	-0.02	690.2	690.06	-0.14

Table 4:6 Geometry parameters for a phantom with smaller beads.

Listed above are the calibrated values and the theoretical values of the geometric parameters when a phantom with smaller beads was imaged at a magnification 2. The difference between the two sets ( $\Delta = \text{theory} - \text{experiment}$ ) is also included.

Other simulation tests that varied the detector pixel pitch, number of projection views, threshold segmenting intensity, etc were also carried out, the results of which are summarized in the discussion.

### 4.3.2.2 Experiment & Results

For the first experimental calibration, six projection views of a home-made phantom were obtained over full rotation from each of eight x-ray sources by placing the phantom at a magnification of 1.1. The detector was operated in the 2x2 binning mode so that the detector pixel pitch was 254  $\mu\text{m}$ . The geometric parameters obtained from this first test are listed in table 4.7. The results show that there is a large variation in the some of the sources' location in terms of  $(u_0, v_0)$ . Based on the reference and using the simulation results, the phantom was redesigned so that it could now be imaged under a magnification greater than 1.

Exp. $u_0$ (mm)	Theory $u_0$ (mm)	$\Delta u_0$ (mm)	Exp. $v_0$ (mm)	Theory $v_0$ (mm)	$\Delta v_0$ (mm)	Exp. SDD (mm)	Theory SDD (mm)	$\Delta\text{SDD}$ (mm)
-209.3	-209.6	-0.3	-1.5	0	1.5	681.0	690	9.0
-185.8	-185	0.8	-2.5	0	2.5	685.1	690	4.9
0	0	0	0	0	0	690.5	690	-0.5
12.8	22.5	9.7	0.12	0	-0.12	689.9	690	0.1
108.1	113.7	5.6	1.8	0	-1.8	688.2	690	1.8
125.6	137.1	11.5	2.8	0	-2.8	687.6	690	2.4
156.7	160.9	4.2	3.2	0	-3.2	687.8	690	2.2
185.1	185	-0.1	1.9	0	-1.9	686.8	690	3.2

Table 4:7 Geometric parameters from initial calibration test (magnification 1.1) on Argus

In the second calibration experiment, thirty projection images of the newly designed phantom were obtained by running the detector at full resolution over

full rotation for the central x-ray source, the two sources at each end of the chamber, and two sources in between. The new results are shown in table 4.8.

Exp. $u_0$ (mm)	Theory $u_0$ (mm)	$\Delta u_0$ (mm)	Exp. $v_0$ (mm)	Theory $v_0$ (mm)	$\Delta v_0$ (mm)	Exp. SDD (mm)	Theory SDD (mm)	$\Delta$ SDD (mm)
-285.0	-287.24	-2.23	2.5	0	-2.5	683.1	685	1.9
-164.29	-160.86	3.43	2.6	0	-2.6	682.1	685	2.9
0	0	0	0	0	0	682.1	685	2.9
162.59	160.86	-1.73	-2.58	0	2.58	679.1	685	5.9
285.0	287.24	2.24	-3.36	0	3.36	676.5	685	8.5

Table 4:8 Geometric parameters obtained using a new phantom (magnification 1.5)

### 4.3.3 Discussion

From the simulation tests, it could be confirmed that better estimates of the geometric parameters are possible if the phantom is imaged at a magnification of 2. This is due to two factors: (i) at a higher magnification, the projection of the beads on the detector covers sufficiently large number of pixels. (ii) Higher magnification aids in obtaining a better fit to the ellipses. If the projection of the beads on the detector covers too few pixels, the results may not be accurate. This was later confirmed using the experimental results. The selection of the threshold intensity is also very important. Different thresholds cause the beads to be segmented out differently thus affecting the centroid location and the calculation of the other parameters that are derived from the centroids. Also, the use of more number of projection images increased the accuracy in the estimate of the geometric parameters. The most important

conclusion of the simulation tests is that the inherent sensitivity of the particular calibration technique limits the accuracy of the source location in the  $x$ -direction to about 1 mm (uncertainty calculated as the standard deviation of the  $\Delta u$  values). The reconstruction algorithm requires the source locations in the  $x$ - and  $y$ -directions and the SDD but it may be most sensitive to the source location in the  $x$ -direction. Even so, the reconstruction of the CIRS type phantom demonstrated that even a variation up to 2 mm in the source 'x' location does not significantly affect either the contrast or the resolution in the reconstructed slices in a tomosynthesis set-up. This can be further explained using the simple geometry shown in figure 4.16. If the 'x' location of the source is off by 2 mm, it translates to a displacement in the projection of a feature on the detector by about 120  $\mu\text{m}$ . This displacement is less than the detector pixel size normally used in tomosynthesis and therefore does not significantly impact the reconstruction either.

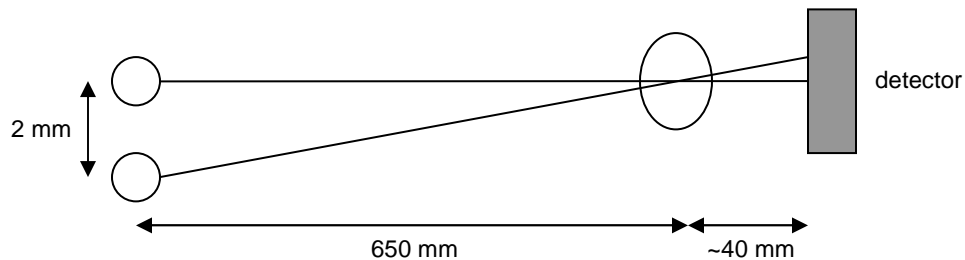


Figure 4.16 Typical imaging geometry in tomosynthesis.

Geometry used to illustrate how a small variation in the  $x$  location of the source will negligibly affect the reconstructed images.

## References

1. Bushberg JT, Seibert JA, et al.: The essential physics of medical imaging. Williams & Wilkins, 1994.
2. European Standard EN 12543-5, 1999.
3. Yang G, Rajaram R, et al.: Stationary digital breast tomosynthesis system with a multi-beam field emission x-ray source array. Proc. of SPIE, Medical Imaging, 2008.
4. National Electrical Manufacturers Association (NEMA) Standards publication XR 5-1992 (R1999)
5. Morgan RH, Bates LM, et al.: The frequency response characteristics of x-ray films and screens. Am. J. Roentgenol. **92**, 426–440, 1964.
6. Rossmann K: Point spread-function, line spread-function, and modulation transfer function, tools for the study of imaging systems. Radiology **93**, 257–272, 1969.
7. Doi K, Bunch PC, et al.: Modulation Transfer Function of Screen-Film Systems Bethesda, MD, 1986.
8. Sones RA and Barnes GT: A method to measure the MTF of digital x-ray systems. Med. Phys. **11**, 166–171, 1984.
9. Hillen W, Schiebel U, et al.: Imaging performance of a digital storage phosphor system. Med. Phys. **14**, 744–751, 1987.
10. Morishita J, Doi K, et al.: Comparison of two methods for accurate measurement of modulation transfer functions of screen-film systems. Med. Phys. **22**, 193–200, 1995.
11. Giger ML and Doi K: Investigation of basic imaging properties in digital radiography. 1. Modulation transfer function. Med. Phys. **11**, 287–295, 1984.
12. Neitzel U, Maack I, et al.: Image quality of a digital chest radiography system based on a selenium detector. Med. Phys. **21**, 509–516, 1994.
13. Fujita H, Tsai DY, et al.: A simple method for determining the modulation transfer function in digital radiography. IEEE Trans. Med. Imag. 11(1), 1992.

14. Ren B, Ruth C, Stein J, et al.: Design and performance of the prototype full field breast tomosynthesis system with selenium based flat panel detector. Proc. of SPIE 5745, 2005.
15. Rizo Ph, Grangeat P, et al.: Geometric calibration method for multiple-head cone-beam SPECT system. IEEE Trans. Nucl. Sci. 41(6), 1994.
16. Sire P, Martin M, et al.: X-ray cone beam CT system calibration. Proc. X-ray Detector Physics and Applications II, pp. 229-239, 1993.
17. Rougée A, Picard C, et al.: Geometrical calibration of x-ray imaging chains for three dimensional reconstruction. Proc. 14<sup>th</sup> Annu. Int. Conf. IEEE EMBS, pp. 47-51, 1992.
18. Gullberg GT, Tsui BMW, et al.: Estimation of geometrical parameters for fan beam tomography. Phys. Med. Biol. 32, pp. 1581-1594, 1987.
19. Gullberg GT, Tsui BMW, et al.: Estimation of geometrical parameters and collimator evaluation for cone beam tomography. Med. Phys. 17(2), pp.264-272, 1990.
20. Noo F, Clackdoyle R, et al.: Analytic method based on identification of ellipse parameters for scanner calibration in cone-beam tomography. Phys. Med. Biol. 45, pp. 3489-3508, 2000.

## **5 Image Reconstruction**

### **5.1 Introduction to reconstruction**

Tomographic imaging deals with the reconstruction of an object from its projection images. A projection refers to the information derived from the energies transmitted through the object when it is illuminated from a particular angle. A projection at a certain angle is the integral of the image in the direction specified by that angle [1]. By using an external source of radiation, a transmission picture of the three-dimensional object is obtained on a two-dimensional surface such as an x-ray film. The reconstruction problem is then defined as obtaining an estimate of the object's internal density distribution given a subset of all possible projections of an object [2]. All algorithms for reconstruction take as input the projection data and produce as output an estimate of the original object. The solution to the problem of reconstruction of an object function from its projections was first described by Radon in 1917 but since the invention of computed tomography (CT) by Hounsfield in 1972 [3], there has been a renewed interest in image reconstruction techniques. It is now possible to compute high-quality cross-sectional images with great accuracy despite projection data not strictly satisfying the theoretical models that are required by the reconstruction algorithms.

A little introduction to x-ray physics is required before starting off about reconstruction. Computed tomography is based on measurement of x-ray flux at different angles. If we assume a mono-energetic beam of x-ray photons, and measure the intensities of the x-rays before and after impinging an object of thickness  $x$  that has a uniform attenuation  $\mu$ , then by Lambert-Beers law, we have

$$I = I_0 e^{-\mu x} \quad \text{Equation 5.1}$$

In the above equation,  $I_0$  is the incident intensity and  $I$  is the transmitted intensity. The attenuation coefficient  $\mu$  is a material property that is a function of energy. Objects with a higher  $\mu$  (bones) attenuate x-rays more than objects with a lower  $\mu$  (eg., soft tissue). In a non-uniform object, the attenuation coefficient is calculated by dividing the object into very small elements. Equation 5.1 is then modified to give

$$p = -\ln\left(\frac{I}{I_0}\right) = \int_L \mu(x) dx \quad \text{Equation 5.2}$$

Here  $L$  is the path length traveled by the x-ray beam through the object and  $p$  is the projections measured in CT. The CT problem is to estimate the attenuation distribution of the object given a set of measured line integrals in the form of projection data (often non-ideal because of poly-energetic x-ray beam, scatter, beam hardening and other effects).

### 5.1.1 Sampling geometry

Since the discovery of CT, there have been at least four different generations of CT scanners [4]. The data collected in the first and the second generation scanners consist of parallel ray projections while the data collected in the third and the fourth generation scanners have projections that go forth from a single point. This focal point is the x-ray source and this type of data collection refers to the fan-beam geometry. Another type of data collection is the cone-beam geometry which uses many fan beams to cover a volume. It is seen from figure 5.1 that the sampling geometry gets increasingly complicated as we move from parallel beam to cone-beam.

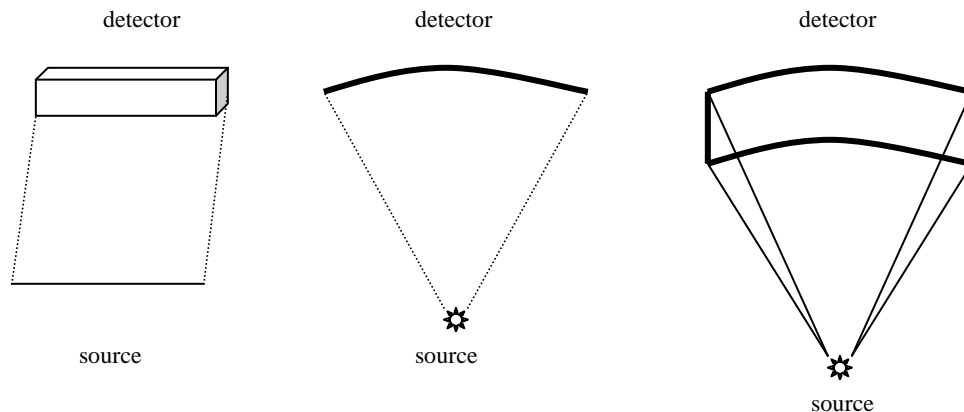


Figure 5.1 Different data sampling geometries.

On the left is simple parallel projection, in the middle is fan-beam sampling and on the right is cone-beam geometry.

It is easy to understand cone beam geometry by starting with parallel beam projections. Projection data set acquired over a  $2\pi$  angle is commonly presented in the form of a sinogram. In a sinogram, the horizontal axis represents the detector channels while the vertical axis represents the projection

angle. A single projection is therefore represented in the sinogram space as shown in figure 5.2. The data collected over all the angles forms a two-dimensional image with intensities representing the magnitude of the projections. Any object can be approximated by a collection of points in space so that its projection is a set of overlapping sine or cosine curves in sinogram space [4].

A simplified object having four homogenous blocks with attenuation coefficients  $\mu_1$ ,  $\mu_2$ ,  $\mu_3$ , and  $\mu_4$  can be used to discuss the various CT reconstruction methodologies. This is illustrated in figure 5.3. Line integrals of this object are available in the horizontal, vertical and diagonal directions. The diagonal equation and three others form a set of independent equations. Thus, we have four equations for four unknowns and therefore a unique solution is possible.

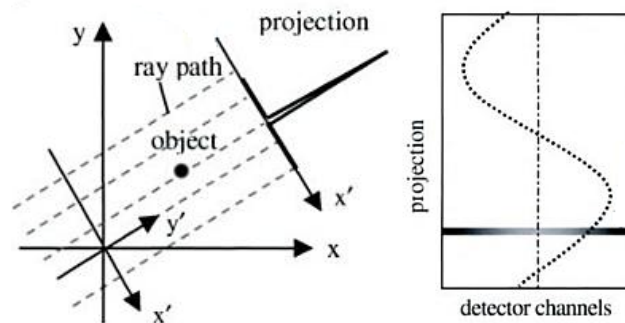


Figure 5.2 Object space (left) and the sinogram space (right).

A sinogram is formed by stacking the projections from all angles. A single projection is represented by a horizontal line in the sinogram space.

In the general case, for an object that is divided into  $N \times N$  small elements, at least  $N^2$  measurements are required in order that a unique solution be possible. Solving such a large set of equations such as this simultaneously is a challenge. Not all the  $N^2$  measurements will be independent and in addition,

there may be errors in some measurements. A possible solution to this problem is iterative reconstruction. More details follow later but the gist of it is that it is a technique that requires repeated updates to the reconstructed pixels based on the difference between measured and calculated projections.

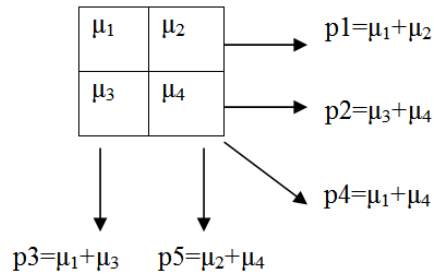


Figure 5.3 An example of an object and its projections.

### 5.1.2 Fourier Slice Theorem

The most important principle in tomographic image reconstruction is the Fourier Slice Theorem that relates the measured projection data to the two-dimensional Fourier transform of the object cross-section [1]. Projections of an object are basically line integrals through the object and by finding the Fourier transform of a projection taken along parallel lines, it is possible to derive the Fourier Slice Theorem. The attenuation of x-rays as they propagate through objects or biological tissue generates line integrals after a log transform [1]. If the object is represented by a two-dimensional function  $f(x, y)$  and each line integral through the object is represented by the parameters  $(\theta, t)$  as shown in figure 5.4.

The equation of the line AB is

$$x \cos \theta + y \sin \theta = t \qquad \text{Equation 5.3}$$

The line integral  $P_\theta(t)$  is written as

$$P_\theta(t) = \int_{(\theta,t)\text{line}} f(x,y) ds. \quad \text{Equation 5.4}$$

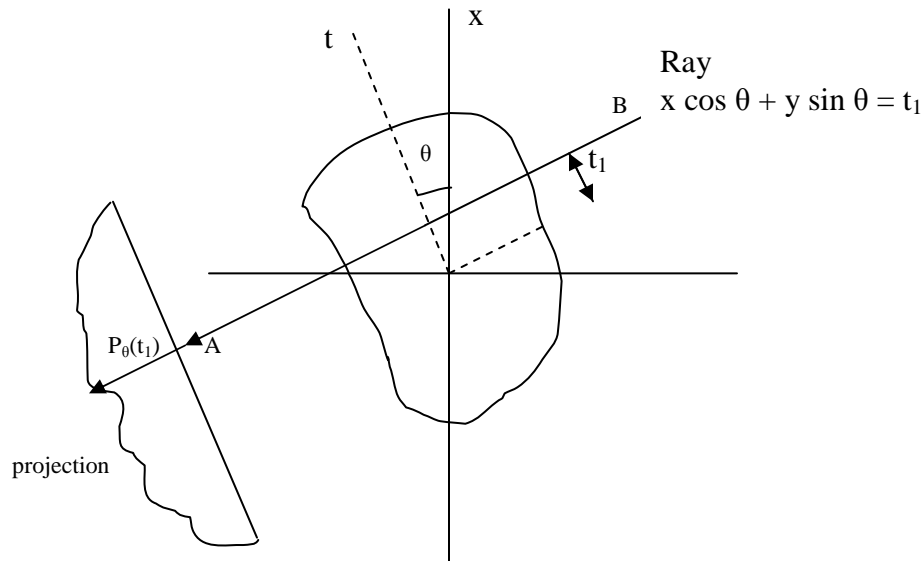


Figure 5.4 An object  $f(x,y)$  and its projection  $P_\theta(t_1)$  are shown for an angle  $\theta$  [5]

Using a delta function, this can be written as

$$P_\theta(t) = \int_{-\infty}^{\infty} \int_{-\infty}^{\infty} f(x,y) \delta(x \cos \theta + y \sin \theta - t) dx dy \quad \text{Equation 5.5}$$

The function  $P_\theta(t)$  is known as the Radon transform of the function  $f(x, y)$  [1]. A collection of parallel ray line integrals forms a parallel projection and is formed by moving an x-ray source and detector along parallel lines on opposite sides of the object. A fan beam projection is formed when a single source is fixed in place relative to a line of detectors.

Now, the two-dimensional Fourier transform of the object function is written as

$$F(u, v) = \int_{-\infty}^{\infty} \int_{-\infty}^{\infty} f(x, y) e^{-j.2\pi(ux+vy)} dx dy \quad \text{Equation 5.6}$$

Similarly, the Fourier transform of  $P_{\theta}(t)$ , the projection at an angle  $\theta$ , is given by

$$S_{\theta}(w) = \int_{-\infty}^{\infty} P_{\theta}(t) e^{-j.2\pi wt} dt \quad \text{Equation 5.7}$$

For a projection at an angle  $\theta = 0$ , the Fourier transform simplifies to

$$F(u, 0) = \int_{-\infty}^{\infty} \int_{-\infty}^{\infty} f(x, y) e^{-j.2\pi ux} dx dy \quad \text{Equation 5.8}$$

The above integral can be split into two parts,

$$F(u, 0) = \int_{-\infty}^{\infty} \left[ \int_{-\infty}^{\infty} f(x, y) dy \right] e^{-j.2\pi ux} dx \quad \text{Equation 5.9}$$

The term in brackets is the equation for a projection along lines of constant x or

$$P_{\theta=0}(x) = \int_{-\infty}^{\infty} f(x, y) dy. \quad \text{Equation 5.10}$$

Substituting this in equation 5.9, we have,

$$F(u, 0) = \int_{-\infty}^{\infty} P_{\theta=0}(x) e^{-j.2\pi ux} dx \quad \text{Equation 5.11}$$

The right-hand side of this equation represents the one-dimensional Fourier transform of the projection  $P_{\theta=0}$ ; thus we have the following relationship between the vertical projection and the two-dimensional transform of the object function:

$$F(u, 0) = S_{\theta=0}(u) \quad \text{Equation 5.12}$$

The above result is the Fourier Slice Theorem and is independent of the orientation between the object and the coordinate system. The Fourier Slice Theorem is therefore stated as follows:

The Fourier transform of a parallel projection of an image  $f(x, y)$  taken at an angle  $\theta$  gives a slice of the two-dimensional transform,  $F(u, v)$ , subtending an angle  $\theta$  with the  $u$ -axis [1]. The Fourier transform of  $P_\theta(t)$  gives the values of  $F(u, v)$  along line  $BB$  as shown in figure 5.5.

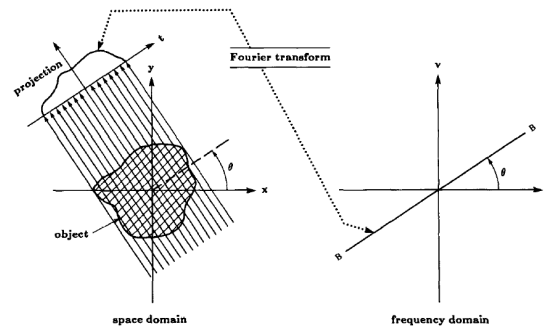


Figure 5.5 The Fourier Slice Theorem.

The theorem relates the Fourier transform of a projection to the Fourier transform of the object along a radial line [6].

In the  $(t, s)$  coordinate system a projection along lines of constant  $t$  is given as

$$P_\theta(t) = \int_{-\infty}^{\infty} f(t, s) ds \quad \text{Equation 5.13}$$

From equation 5.7, its Fourier transform is given by

$$S_\theta(w) = \int_{-\infty}^{\infty} P_\theta(t) e^{-j.2\pi wt} dt. \quad \text{Equation 5.14}$$

Substituting equation 5.13 into 5.14, we obtain

$$S_\theta(w) = \int_{-\infty}^{\infty} [f(t, s) ds] e^{-j.2\pi wt} dt \quad \text{Equation 5.15}$$

In the  $(x, y)$  coordinate system,

$$S_{\theta}(w) = \int_{-\infty}^{\infty} \int_{-\infty}^{\infty} f(x, y) e^{-j.2\pi\omega(x \cos \theta + y \sin \theta)} dx dy \quad \text{Equation 5.16}$$

The right-hand side of this equation represents the two-dimensional Fourier transform at a spatial frequency of ( $u = \omega \cos \theta$ ,  $v = \omega \sin \theta$ ).

$$S_{\theta}(w) = F(\omega, \theta) = F(\omega \cos \theta, \omega \sin \theta) \quad \text{Equation 5.17}$$

The above result shows that by taking the projections of an object function at angles  $\theta_1, \theta_2, \dots, \theta_k$  and Fourier transforming each of these, it is possible to determine the values of  $F(u, v)$  on radial lines as shown in figure 5.5. If an infinite number of projections are taken, then  $F(u, v)$  would be known at all points in  $uv$ -plane. Knowing  $F(u, v)$ , the object function  $f(x, y)$  can be recovered using the inverse Fourier transform [1].

$$f(x, y) = \int_{-\infty}^{\infty} \int_{-\infty}^{\infty} F(u, v) e^{j.2\pi(ux+vy)} dudv \quad \text{Equation 5.18}$$

Thus, it follows from the Fourier Slice Theorem that with each projection a line in the two-dimensional Fourier transform of the object is obtained by performing the Fourier transform of the projection. It is possible to fill the entire Fourier space by collecting enough projections. Then, once the Fourier transform is obtained, the object itself can be recovered using the inverse Fourier transform.

### 5.1.3 Filtered Backprojection

The most popular implementation of the Fourier Slice Theorem is in the form of the filtered back projection algorithm. In order to derive the simplest form of the filtered backprojection formula, we start with equation 5.18. We can use

the coordinate transformation  $u = \omega \cos \theta$ ,  $v = \omega \sin \theta$  so that equation 5.18 becomes

$$f(x, y) = \int_0^{2\pi} d\theta \int_0^{\infty} F(\omega \cos \theta, \omega \sin \theta) e^{j.2\pi\omega(x \cos \theta + y \sin \theta)} \omega d\omega \quad \text{Equation 5.19}$$

Using Fourier Slice Theorem, we get

$$f(x, y) = \int_0^{2\pi} d\theta \int_0^{\infty} S_{\theta}(\omega) e^{j.2\pi\omega(x \cos \theta + y \sin \theta)} \omega d\omega = \int_0^{\pi} d\theta \int_0^{\infty} S_{\theta}(\omega) e^{j.2\pi\omega(x \cos \theta + y \sin \theta)} \omega d\omega \\ + \int_0^{\pi} d\theta \int_0^{\infty} S_{\theta+\pi}(\omega) e^{-j.2\pi\omega(x \cos \theta + y \sin \theta)} \omega d\omega \quad \text{Equation 5.20}$$

In parallel beam geometry, projections that are  $180^\circ$  apart represent the same set of x-ray paths so that

$$S_{\theta+\pi}(\omega) = S_{\theta}(-\omega) \quad \text{Equation 5.21}$$

Using the above relation, we get

$$f(x, y) = \int_0^{\pi} d\theta \int_{-\infty}^{\infty} S_{\theta}(\omega) |\omega| e^{j.2\pi\omega(x \cos \theta + y \sin \theta)} d\omega \quad \text{Equation 5.22}$$

$S_{\theta}(\omega)$  is the Fourier transform of the projection at an angle  $\theta$ . The inside integral in equation 5.22 is simply the inverse Fourier transform of  $S_{\theta}(\omega)|\omega|$ . In the spatial domain, it is the projection filtered by a function whose frequency domain response is  $|\omega|$ . This is called the filtered projection. If the filtered projection is represented by  $g(t, \theta) = g(x \cos \theta + y \sin \theta)$ , then we have

$$f(x, y) = \int_0^{\pi} g(x \cos \theta + y \sin \theta) d\theta \quad \text{Equation 5.23}$$

Thus the reconstructed image  $f(x, y)$  is the summation of all filtered projection samples passing through the point  $(x, y)$ . The value of the filtered projection is

smearred along the entire straight line path of x-rays. This is the backprojection process illustrated in figure 5.6 [4].

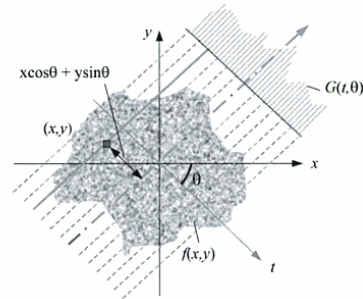


Figure 5.6 Illustration of the backprojection process [4].

Without going into great details about the exact steps involved in filtration and backprojection, we can summarize the reconstruction steps for parallel projections as follows: obtain projection images for various angles, Fourier transform the projections, multiply by a suitable filter to obtain  $G(\omega, \theta)$ , take the inverse Fourier transform to obtain filtered projection  $g(t, \theta)$  and finally backproject  $g(t, \theta)$  and add to the image  $f(x, y)$ .

#### 5.1.4 Fan beam and cone beam reconstruction

A much faster way to generate projections is by using fan beams as shown in figure 5.7. Fan-beam geometry could be either equiangular fan beam or equally-spaced fan beam [4].

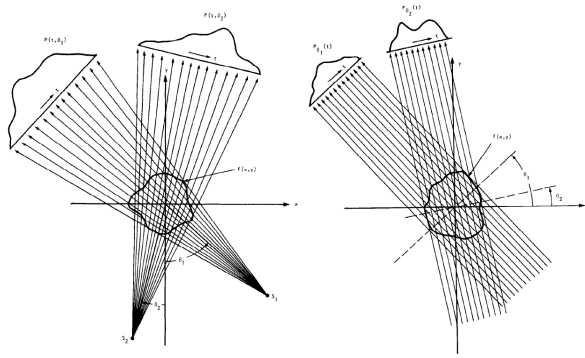


Figure 5.7 Fan-beam and parallel projections [1].

In fan-beam geometry, the fan-beam projections are re-binned to parallel beam projections so that reconstruction algorithms can be applied on them directly. In order to understand re-binning, we will look first at the sampling pattern of a set of parallel projections in the sinogram space. Figure 5.8 shows a single projection ray mapped onto the sinogram space. For parallel projections, all the samples fall onto a uniformly spaced rectangular grid as shown in figure 5.9 where each parallel projection is represented by a single row of dots.

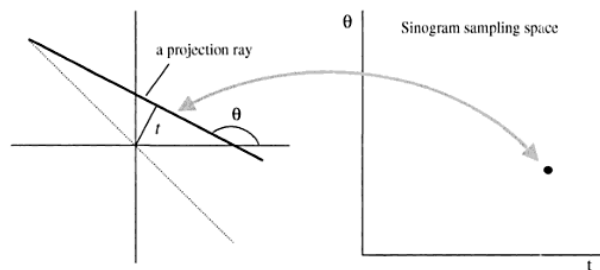


Figure 5.8 Generation of a sinogram.

A projection sample in real space is mapped onto a point in the sinogram space. The graph on the left has on its horizontal axis the distance of a ray to the iso-center and on its vertical axis the angle of the ray with respect to the x-axis.

If a set of fan beam samples are mapped onto the same sinogram, they will appear as dots that do not fall on to the rectangular grid [4]. They will map to

a slanted row of dots because the different fan beam rays make different angles with the x-axis. Similarly, the distance from the fan beam rays to the iso-center does not change uniformly. However, we can see that the fan-beam sampling can be equated to the parallel beam sampling grid by interpolation (either linear or non-linear). It is evident that a parallel projection ray located at an intersection of the grid can be estimated by simply interpolating the neighboring fan beam samples. Once a set of parallel projections are obtained by such interpolation, parallel beam reconstructions can be applied to the images directly. Thus fan-beam reconstructions are more complex than simple parallel beam reconstruction.

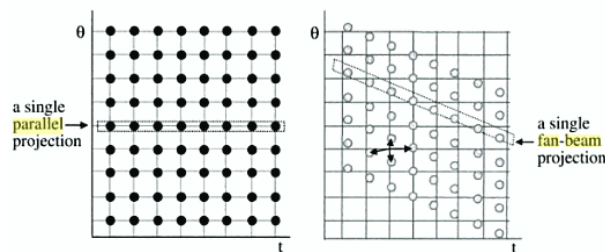


Figure 5.9 Mapping of parallel and fan beam projections on to sinogram space.

Parallel projections are mapped onto the solid parallel dots in the sinogram space (left). Fan-beam projections are not necessarily parallel (right) and are mapped onto slanted rows of dots in the sinogram space [4].

The discussions so far have been limited to simple one-dimensional projections (line integrals of a slice through the object). However it is possible and advantageous to collect projection images on a two-dimensional array. A large organ or a significant portion of the patient can be imaged at once with a large area detector. This enables isotropic resolution and also reduces probability of patient motion during acquisition. Also, a larger detector means efficient use of

the x-ray photons generated in the x-ray tube. This type of data collection with the use of a two-dimensional flat or curved detector is called cone-beam scanning [4]. Cone-beam scanning is one step beyond fan-beam scanning and therefore is a very complex area of study. There has been significant research on this topic [7-11]. The algorithms developed for cone-beam reconstructions are either exact or approximate but the most popular and well-known reconstruction is the FDK reconstruction for cone-beam reconstruction with a flat-panel detector [7]. It could be considered a natural extension of the fan-beam reconstruction method.

The cone beam geometry is shown in figure 5.10. Just like in the fan beam and the parallel beam cases, the iso-center is the rotation axis of the system. The rotated coordinate system is  $(x', y', z')$  in which the detector is parallel to the  $x'$  axis. A point to be reconstructed  $(x', y', z')$  is mapped to  $(s, v)$  on the imaginary detector [4]. This location is obtained by calculating the intersection of the imaginary detector with a straight line that connects the x-ray source and the point  $(x', y', z')$ . Without going into the entire derivation, the FDK formula for cone beam reconstruction is given as

$$f(x, y, z) = \frac{1}{2} \int_0^{2\pi} \left( \frac{D}{D + yx'} \right)^2 d\beta \int_{-\infty}^{\infty} \cos(\xi) q(s, v, \beta) h(s'-s) ds \quad \text{Equation 5.24}$$

The FDK formula is only an approximate formula for cone beam reconstruction. A single circular trajectory does not provide sufficient sampling for an exact cone beam reconstruction. The algorithm performs reasonably well for small cone angles. Many new versions of the FDK algorithm require different source trajectories to compensate for incomplete sampling.

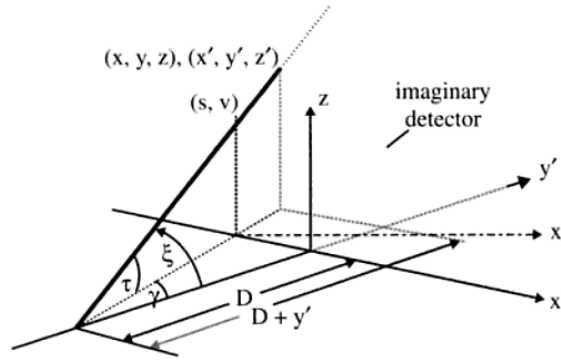


Figure 5.10 Geometry for cone beam imaging [4].

## 5.2 Iterative algorithms

The reconstruction algorithms commonly used in CT are analytical in nature where the data are weighted, filtered and backprojected. The projection process is expressed as  $\mathbf{g} = \mathbf{H}\mathbf{f}$ , where  $\mathbf{g}$  is the measured projection data and the matrix  $\mathbf{H}$  is a model of the projection process used to estimate the image pixels  $\mathbf{f}$ . In order to find  $\mathbf{f}$ , we need to find the inverse solution but direct matrix inversion is difficult to solve and very sensitive to noise. This is what happens in filtered backprojection (FBP).

Iterative algorithms offer a different approach to the reconstruction problem. In iterative algorithms, the reconstruction is started with some initial estimate of the image pixels. This initial estimate is projected by using the matrix  $\mathbf{H}$  to generate a set of estimated projections. The difference between the estimated and the measured projections gives the error projections that are then backprojected to the image space. This image space error is used to update the image estimate and create a new current estimate. The whole process is

repeated until terminated. The general process of the iterative algorithm is shown in figure 5.11 [12].

Iterative algorithms in general can model the projection process more accurately. They perform better than analytical algorithms with truncated data sets and in limited angle imaging such as tomosynthesis. They also offer improved metal artifact reduction and noise performance whereas analytical algorithms are often very sensitive to noise. They used to be considered computationally intensive because of multiple projections and backprojections. However, with modern computers and improved algorithms, iterative reconstruction often turns out to be at least as fast as the analytical techniques.

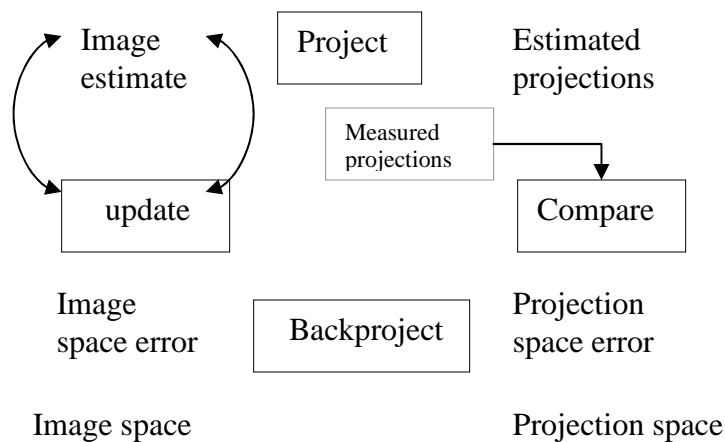


Figure 5.11 Sequence in an iterative reconstruction algorithm [12]

Iterative algorithms can still further be classified into either algebraic or statistical algorithms. The following two sections discuss the two types of iterative algorithms in detail.

The other thing in projection modeling is the use of a matrix-based model to compute the matrix  $\mathbf{H}$ . This poses big storage and computational efficiency issues especially when three-dimensional imaging is involved. The alternative is to use a projection operator. In this case, the projections of an image are computed without any explicit computation and storage of the individual elements of the matrix  $\mathbf{H}$ . This method is more flexible and computationally efficient than the matrix based method [12].

### 5.2.1 Algebraic iterative algorithms

The algebraic reconstruction algorithms are based on a simple procedure proposed by Kaczmarz [13] to solve a system of consistent linear equations. The projection process as given by  $\mathbf{g} = \mathbf{H}\mathbf{f}$  is a set of linear equations [12]. The solution space is an N-dimensional hyperspace, where N is the number of pixels to be estimated. Each point in the solution space defines a particular solution image. Each equation defines a hyperplane in the solution space, that is, only those images that solve the given equation lie on the hyperplane. All the hyperplanes intersect at a point in the solution space when there is a unique solution to the set of equations. For multiple solutions, the hyperplanes will intersect in a line or a hyperplane. The Kaczmarz procedure is illustrated in figure 5.12 where the current estimate is successively projected onto each equation by finding an estimate obtained from solving the equation that lies closest to the current estimate [12]. It is easily seen that the convergence rate of the above method depends on the orthogonality of the successive equations. For a set of

orthogonal equations, the solution is reached within a few iterations whereas for a non-unique solution the hyperplanes never intersect and the iterative process does not converge to a unique solution.

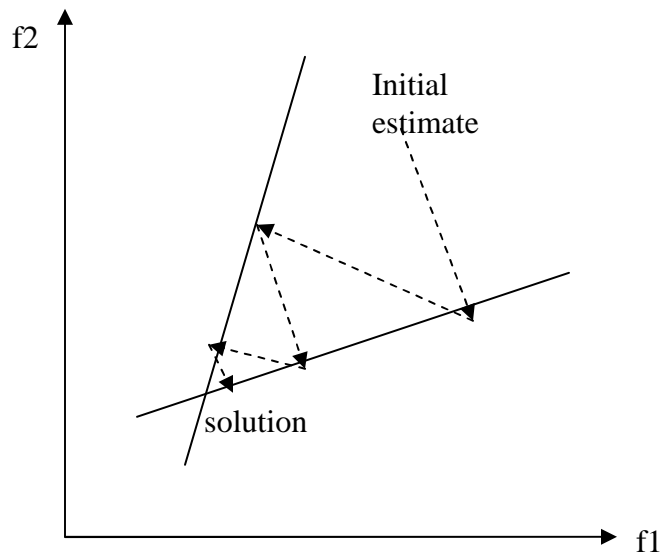


Figure 5.12 Kaczmarz method for finding the solution to a system of consistent linear equations [12].

The Algebraic Reconstruction Technique (ART) first proposed by Gordon, Bender and Herman [15] is based on the Kaczmarz method. The ART method is sequential. ART implements a correction to the estimated image vector so that the updated estimate will satisfy a single ray-sum equation representing a ray integral [12].

The disadvantage with ART is that updates are made for one equation or one projection bin at a time. In addition because of the inconsistencies in the set of equations representing the forward process, the discrete formulation based on Kaczmarz method does not accurately represent the continuous nature of the

image function. Thus, the result is likely to be a noisy looking image. This is caused because solving a single equation results in a noticeable stripe along that particular ray and when repeated for all the rays in different directions, this results in a noisy reconstructed image [16].

A simultaneous algebraic reconstruction technique (SART) was developed with the goal of reducing the noise associated with ART [16]. Equations corresponding to many points in the discrete image are solved simultaneously. Fewer rays are used per view to average the errors in the correction process. The computation time increases with the use of more number of rays. Another way to reduce the noise is the use of a relaxation factor ( $\lambda < 1$ ). Also, the pixel-based method is discarded in favor of an approximate bilinear-elements approach [17] to model the forward projection process. The basic correction strategy of ART is still used in SART but the correction terms are applied to all the rays in a particular projection view simultaneously instead of sequentially. In ART, the image estimate is updated using the error terms from each ray. A single iteration of the ART method is complete when all the rays in a view have been used once. In the case of SART, the error terms from each ray are computed and saved until all rays in that view are considered. Then the average correction is computed and used to update the image estimate with the idea that a simultaneous correction for all the rays in a view represents the continuous nature of the image function [18].

In ART, the new image estimate is given as follows:

$$\hat{f}_{ij}^{(q+1)} = \hat{f}_{ij}^{(q)} + \lambda^{(q)} w_{ijmn} \left[ \frac{p_{mn} - \sum_{i=1}^I \sum_{j=1}^J w_{ijmn} \hat{f}_{ij}^{(q)}}{\sum_{i=1}^I \sum_{j=1}^J w_{ijmn}^2} \right] \quad \text{Equation 5.25}$$

The new estimate  $\hat{f}_{ij}^{(q+1)}$  is obtained by using the update factor on the old estimate  $\hat{f}_{ij}^{(q)}$ . The numerator in the update correction factor is the error term between the estimated and measured projections ( $p_{mn}$ ) while the denominator is the normalization term. The old estimate is updated according to the weighting coefficients  $w_{ijmn}$  and the relaxation factor  $\lambda^{(q)}$ . The subscripts  $m$  and  $n$  represent the projection index for a total of  $M$  projections and the ray index for a total of  $N$  rays in each projection view [16, 19].

In SART, the correction terms from all rays within a projection view are combined to update the image estimate as follows [19-21]:

$$\hat{f}_{ij}^{(q+1)} = \hat{f}_{ij}^{(q)} + \lambda^{(q)} \cdot \left[ \frac{\sum_{n=1}^N w_{ijmn} \left[ \left[ p_{mn} - \sum_{i=1}^I \sum_{j=1}^J w_{ijmn} \hat{f}_{(ij)}^{(q)} \right] / \sum_{i=1}^I \sum_{j=1}^J w_{ijmn} \right]}{\sum_{n=1}^N w_{ijmn}} \right] \quad \text{Equation 5.26}$$

In equations 5.25 and 5.26,  $\lambda^{(q)}$  is the relaxation factor. It could be set to be a constant or it can be varied between steps in the reconstruction algorithm. It is generally chosen to be between 0 and 2. Under-relaxation ( $\lambda < 1$ ) can often reduce the noise in the reconstruction at the cost of increase in the time for converging to a solution.

## 5.2.2 Statistical Iterative Algorithms

A projection process is represented by the following form:

$$g = H\hat{f} \quad \text{Equation 5.27}$$

The projection data is said to be consistent if there exists either a unique solution  $\hat{f}$  or in the case of an under-determined solution, more than one solution to the above equation. However, if the data is inconsistent, then no image solution is possible. Most of the reconstruction algorithms assume the data to be consistent however, the real data obtained from experiments is corrupted by noise or there may be inaccuracies in the projection model  $\mathbf{H}$  that make the data inconsistent. That is the reason the reconstruction algorithms suffer noise issues. Statistical reconstruction algorithms use some known information about the statistical nature of the projection data to choose the likely or most probable solution, even in cases where no exact solution to the above equation exists [12].

Statistical reconstruction algorithms have two parts: a criterion and an algorithm. While a criterion is the statistical basis for selecting a possible solution to the above equation, the algorithm represents the method to use to get to the solution specified by the criterion. There are many criteria and algorithms, and in general, various combinations of the two are possible. The most common criterion is the Poisson-based maximum likelihood criterion. Commonly used algorithms include the expectation-maximization, convex, steepest descent algorithm, etc.

Maximum likelihood (ML) is a well known criterion in which the image estimate is one for which the measured projection data has the highest probability. A Poisson distribution is written as

$$L(\hat{f}) = \text{Prob} [g|f:H] = \prod_j \exp \left[ - \sum_k h_{jk} \hat{f}_k \right] \left( \sum_k h_{jk} \hat{f}_k \right)^{g_j} (g_j!)^{-1} \quad \text{Equation 5.28}$$

The ML solution is the  $\hat{f}$  that maximizes equation 5.28. The same  $\hat{f}$  maximizes the natural logarithm of equation 5.28. For simplification, the log-likelihood criterion is thus written as:

$$\log L(\hat{f}) = \log(k) + \sum_j - \sum_k h_{jk} \hat{f}_k + g_j \log \left( \sum_k h_{jk} \hat{f}_k \right) - \log(g_j!) \quad \text{Equation 5.29}$$

Taking the derivative of the above equation with respect to each parameter and equating to zero will solve the above equation. This leads to the following case:

$$\frac{\partial}{\partial \hat{f}_i} \log L(\hat{f}) = \sum_j h_{ji} \left( \frac{g_j}{\sum_k h_{jk} \hat{f}_k} - 1 \right) = 0 \quad \text{Equation 5.30}$$

An iterative algorithm is required to be used to solve for  $\hat{f}$ . There is a unique solution to the above Poisson based log likelihood function for consistent data and at least one solution in the case of inconsistent data [12].

The most commonly used ML based algorithm in emission and transmission tomography has been the Expectation Maximization (EM) algorithm [22]. The EM algorithm is applied when the data to be estimated is in the form of pixel intensities in the projection views. In the expectation (E) step of the algorithm, the conditional expectation  $E \{ \log \text{Prob} [\mathbf{q}|\mathbf{g}, \mathbf{f}:H] \}$  is developed. In the maximization (M) step, the new image estimate that maximizes the above

expectation is found. The two steps are performed iteratively to increase the log likelihood function and eventually achieve the solution. The details and the derivation of the EM algorithm are not presented here but the algorithm in its final form is given as:

$$\hat{f}_i^{new} = \frac{\hat{f}_i^{old}}{\sum_j h_{ji}} \sum_j h_{ji} \frac{g_j}{\sum_k h_{jk} \hat{f}_k^{old}} \quad \text{Equation 5.31}$$

The ML-EM algorithm is a relatively simple algorithm whose convergence behavior is known. The ML-EM algorithm constrains non-negativity and allows pixels to be set to zero. It can also model non-uniform attenuation. However, the main disadvantage is that the convergence of ML-EM is slow and a solution may take several iterations. This leads to the other issue with ML-EM - image noise – the noise increases with iterations. Often, noise reduction filters are used after terminating the ML-EM reconstruction after a certain number of iterations.

The most effective methods that were applied to overcome the problems of slow convergence are the block-iterative methods making use of subsets [23]. In these methods, projection data is divided into a many independent subsets so that the reconstruction is applied to each subset sequentially. With the use of subsets, the image estimate is updated more often and thus results in acceleration of the reconstruction algorithm.

In the ordered subsets (OS) method, projection data are grouped into an ordered sequence of mutually exclusive subsets and these subsets could in general be processed with any kind of iterative algorithms such as EM. An iteration of OS-EM is defined as one pass through all the subsets, while using the

correction terms from each subset to update the image estimate [24]. The OS-EM algorithm, with the back projections done only for the projection bins in subset  $S_n$ , could be written as follows [12]:

$$\hat{f}_i^{new} = \frac{\hat{f}_i^{old}}{\sum_{j \in S_n} h_{ji}} \sum_{j \in S_n} h_{ji} \frac{g_j}{\sum_k h_{jk} \hat{f}_k^{old}} \quad \text{Equation 5.32}$$

In the other algorithm similar to EM called the convex algorithm, the log likelihood function (as given in equation 5.29) is re-written using the strictly convex functions  $f_i(t) = d_i e^{-t} + Y_i t$  where  $d_i$  is the expected number of photon counts leaving the source along a projection  $i$  and  $Y_i$  is the measured number of photons [25]. With the convex functions, the maximization of the log-likelihood function results in a form slightly more complex than that represented by equation 5.30. Although this form has a unique and positive solution, it cannot be solved exactly but can be solved quickly using Newton's method. The convex algorithm has been shown to be considerably more efficient than the EM algorithm and its convergence behavior is also better understood. The convex algorithm adapts well to array and parallel processing.

The application of ordered subsets to the convex algorithm results in the ordered-subsets convex (OSC) algorithm [26]. Similar to OS-EM, OSC uses subsets of projections with the convex algorithm so that the update of the iterant is used as the starting image for the processing of the next subset. The OSC algorithm is written as follows [27]:

$$\mu_i^{new} = \mu_i^{old} + t \cdot \mu_i^{old} \left( \frac{\sum_{j \in S_n} h_{ij} (I_{0j} \exp[-\sum_k h_{jk} \mu_k^{old}] - I_j)}{\sum_{j \in S_n} h_{ij} \left( \sum_k h_{jk} \mu_k^{old} \right) \left( I_{0j} \exp[-\sum_k h_{jk} \mu_k^{old}] \right)} \right) \quad \text{Equation 5.33}$$

Here,  $\mu_i^{old}$  and  $\mu_i^{new}$  are the attenuation coefficients in pixel  $i$  before and after update. The elements of the matrix  $\mathbf{H}$  that maps the image space to the projection space are represented by  $h_{ij}$ .  $I_j$  is the measured data and  $I_{0j}$  is the blank data (data measured without the subject in place). The numerator in the above expression is the error between the measured and estimated projection data while the denominator is called the normalization term. The normalization term is the back projection of the product of the estimated projection data and the estimated  $\mu$  detection intensity, and is usually updated every iteration. The parameter  $t$  is a step-size parameter that could be varied while  $S_n$  denotes the  $n$ th subset of projections.

### 5.3 Development of Ordered-Subsets Convex algorithm

When the idea of the stationary digital breast tomosynthesis system was first tested using nine multi-beam field emission x-ray (MBFEX) sources, the OSC algorithm was employed in the reconstruction of the preliminary images. Nine equally spaced MBFEX sources generated projection images of the breast phantom as shown in figure 5.13. These were reconstructed using the OSC algorithm as described by equation 5.33. The first results were able to show that the OSC technique is effective in resolving objects at different depths and could be useful in a novel array-based stationary imaging system such as Argus.

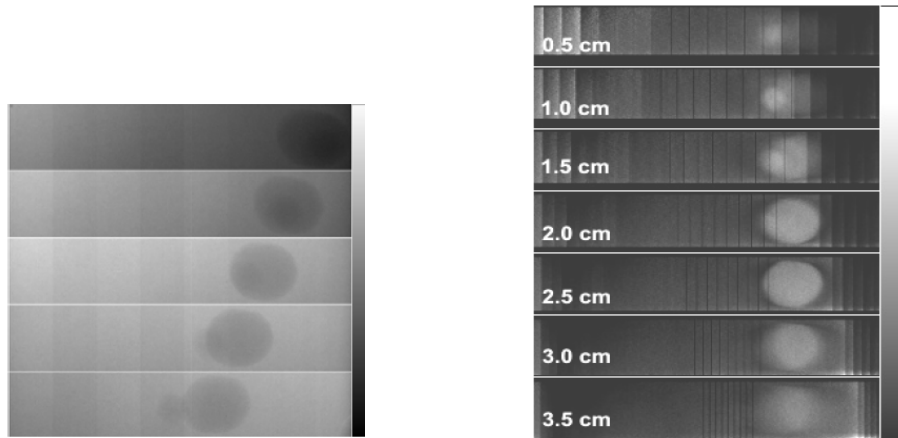


Figure 5.13 Early projection images and reconstruction results.

Five sample projection images of a breast phantom obtained from preliminary MBFEX sources are shown on left. On right are the slices reconstructed using OSC that show two distinct objects getting resolved at different depths [27].

As the stationary DBT system was getting ready, modifications were made to the OSC algorithm to reconstruct images obtained from sources that are equally angularly spaced. In addition, the algorithm was made considerably faster by implementing the use of a projection operator instead of the earlier matrix-based model to calculate  $\mathbf{H}$  during the projection modeling process.

In the OSC algorithm represented by equation 5.33, there are one projection and two backprojection operations for every projection view. One of the two backprojection operations is to calculate the normalization term, and so nearly a third of the total computation time is spent on it. However, the normalization term does not change significantly after the first few updates. In order to improve the computational efficiency of the algorithm, it was modified so that the normalization term is only calculated once at the beginning of the iterations [28]. The modified OSC (MOSC) is then written as follows:

$$\mu_i^{new} = \mu_i^{old} + \frac{t}{\sum_{j \in \mathcal{S}_n} h_{ij} I_j \log\left(\frac{I_{0j}}{I_j}\right)} \mu_i^{old} \sum_{j \in \mathcal{S}_n} h_{ij} \left( I_{0j} \exp\left[-\sum_k h_{jk} \mu_k^{old}\right] - I_j \right) \quad \text{Equation 5.34}$$

MOSC has been tested on simulated mouse images as well as preliminary experimental images. It was demonstrated that MOSC was faster than OSC by about 30% while maintaining similar noise-resolution characteristics [28].

## 5.4 Comparison of algorithms

The iterative MOSC reconstruction technique was applied to reconstruct simulated as well as preliminary experimental phantom images obtained on the Argus system. The simulated CIRS phantom as described in Chapter 2 has four sets of calcifications (with  $\text{AlO}_2$  specifications) of varying grain size, four nylon fibers of varying diameters, and four masses (75% adipose/25% glandular) of varying thicknesses all embedded in an uniform background. For the simulation, the system is assumed to have nine sources arranged linearly with a flat-panel detector placed about 64.5 cm away from the center of the object to be imaged. The object is assumed to lie directly on the detector. The projection and blank images (1100 x 500 x 9) simulated with a 32 kVp polychromatic Mo spectrum were reconstructed on non-cubic voxels of size 1.27 mm x 0.127 mm x 0.127 mm. The images were reconstructed using MOSC and a version of SART written by another graduate student. The performance of the two algorithms was compared by evaluating image quality parameters such as contrast and noise in the reconstructed images.

Representative slices from the simulated phantom reconstructed using MOSC are shown in figure 5.14. In our implementation of MOSC, the step-size parameter was set to 1 and the subsets option was not utilized. The images show that the features are resolved well at their true depths. Similar representative slices from the simulated phantom reconstructed using SART are shown in figure 5.15. In SART, the variable parameter  $\lambda$  was set to increase sinusoidally from 0.04 to 0.2. The two figures show the differences in the contrast and the noise between the two algorithms. SART also introduces inaccuracies at the edge of the phantom where truncation occurs and therefore results in a smaller effective field of view than MOSC [29].

To evaluate the image quality, the contrast in the calcifications was calculated as  $(I_{obj} - I_{bkg}) / (I_{obj} + I_{bkg}) * 100$  where  $I_{obj}$  and  $I_{bkg}$  are the intensities in the object and the background obtained by taking a horizontal profile through the objects of interest in the reconstructed image. Since Poisson noise was simulated in the projection data, a small and uniform region of interest (ROI) was chosen in the reconstructed images and the standard deviation of the pixel values in the selected ROI was calculated to evaluate noise.

The contrast of the largest calcification was estimated and used for all comparison studies. The contrast and the noise as a function of iteration number in the MOSC and SART reconstructions are illustrated in figure 5.16. Although the contrast in SART starts out being higher, MOSC is able to reach the same or better contrast after only the second iteration. The noise also grows much faster with iterations in the case of SART than in the case of MOSC.

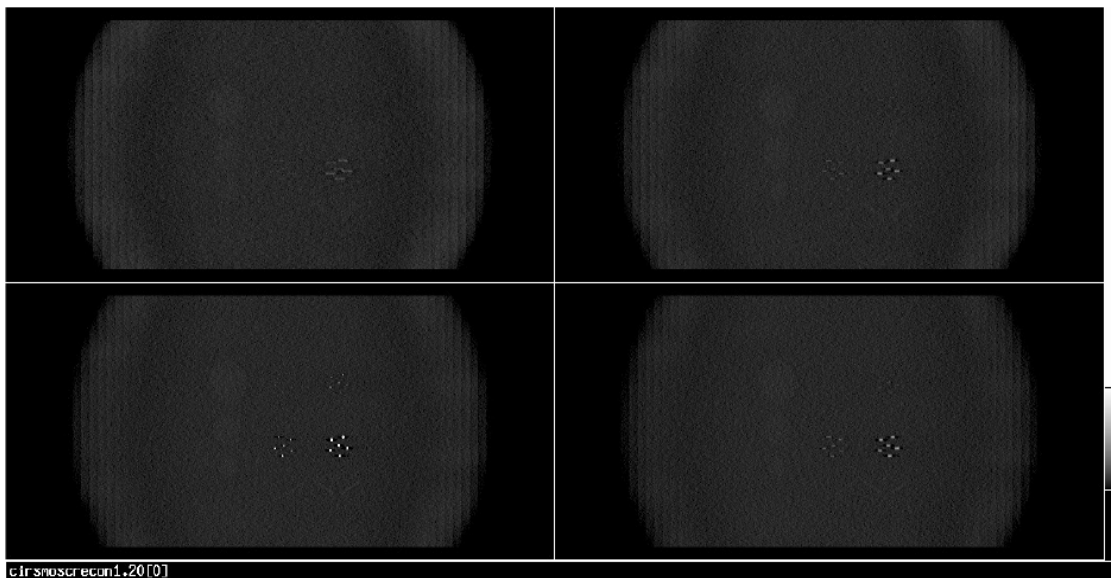


Figure 5.14 Representative slices of the CIRS type phantom reconstructed with MOSC. The slices show how the different features get focused at their true depths (3.81 mm).

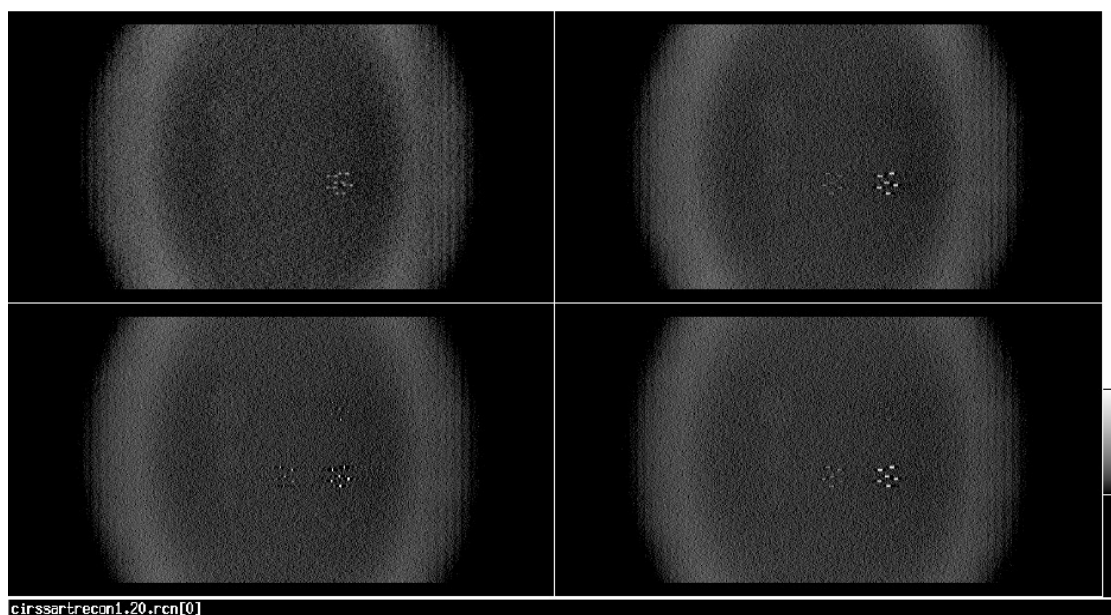


Figure 5.15 Representative slices of the CIRS type phantom reconstructed with SART.

The plot of noise as a function of contrast shows that SART achieves similar contrast as MOSC but at the cost of a large increase in noise.

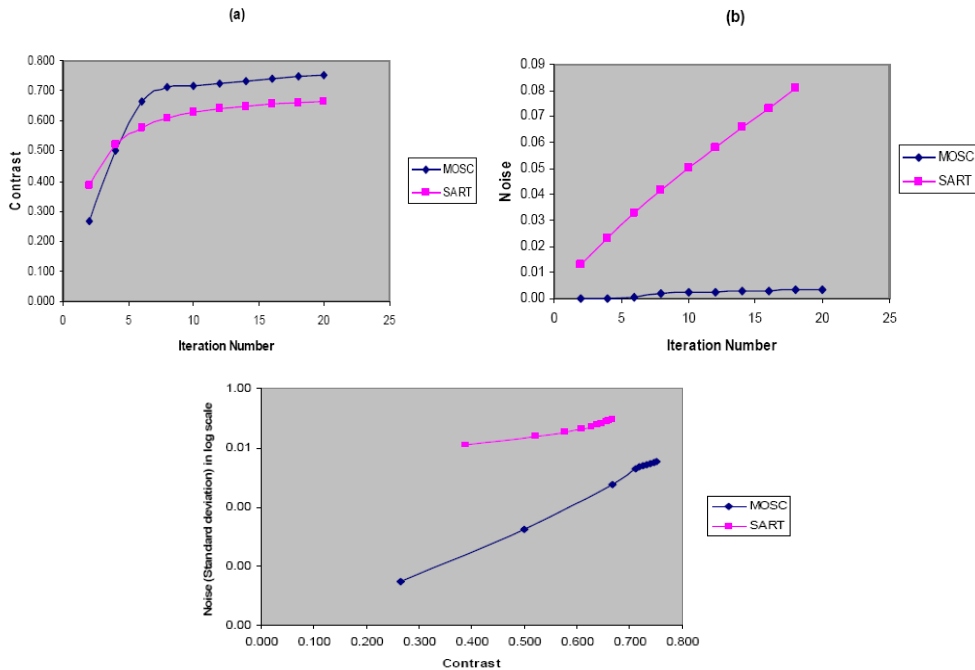


Figure 5.16 (a) Contrast and (b) noise as a function of iteration number in the two reconstructions. Shown below is noise as a function of contrast for the two reconstruction algorithms.

The step-size parameter plays an important role and other earlier studies on SART have used different step-size parameters to suit the particular application. In our implementation of SART, the parameter was set to vary sinusoidally from 0.04 to 0.2. It could be that the high noise is a result of the choice of  $\lambda$ . Also, SART updates after each projection while MOSC uses all of the projections for an update. So there might have been similar noise in both cases if MOSC was tried with subsets of one projection. However, SART does tend to be noisy in general and at least one another study that compared the performance of SART with ML-convex (both algorithms starting with initial estimates provided by a back projection reconstruction) concluded that although the CNR was about equivalent in the two cases, the noise was much higher in

SART [30]. In the current comparison, the computation time for both reconstruction algorithms was about the same up to 20 iterations but again MOSC could have been faster with the application the subsets option.

## 5.5 Imaging experiment

When the stationary digital breast tomosynthesis system was completely set up and ready to image, nine projection images of a home-made sponge phantom of thickness 2.2 cm that has three lima beans sandwiched between the sponges were obtained. The phantom was placed about 2.5 cm away from the Varian Paxscan detector along with two aluminum plates of different thicknesses that were placed closer to the detector for reference. The whole set-up was imaged at 31 kVp with an exposure of 3 mAs to yield projection images of size 960 x 768 x 9 (shown in figure 5.17). Corresponding blank images were also obtained and using calibrated values of the source-detector distance and the location of the sources, the images were reconstructed using MOSC to yield 50 slices (slice thickness of 1.27 mm) through the phantom with an in-plane resolution of 127  $\mu\text{m}$ .

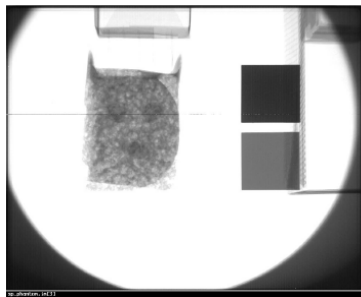


Figure 5.17 A single projection image of the home-made sponge phantom. On the right of the phantom are two aluminum plates of varying thickness used for reference [29].

Even without the use of subsets, the reconstruction of this first experimental 9-beam system with 960 x 768 pixels took less than six minutes for ten iterations. The reconstruction clearly showed the inserted beans and the aluminum plates getting resolved at their respective depths as shown in figure 5.18. The same projection images were also reconstructed using SART. SART was able to resolve the objects well at their true depths, and delivered similar visual quality [29]. However, earlier simulation results and a quick estimate of the contrast and noise in the reconstructed images allowed us to conclude that MOSC is capable of delivering excellent image quality when used in a novel tomosynthesis set up such as ours.

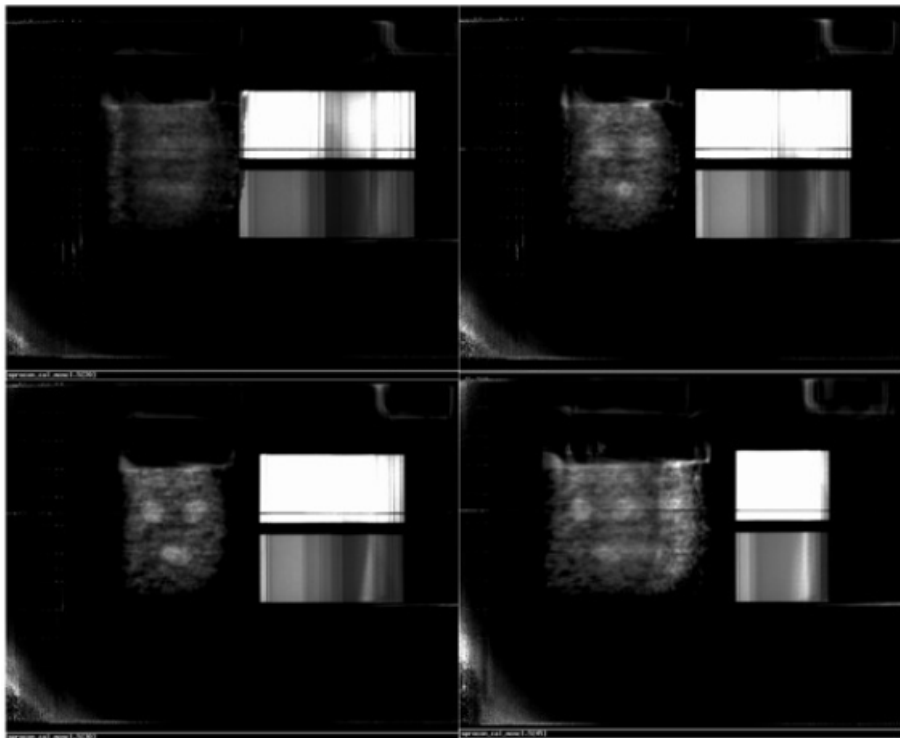


Figure 5.18 Slices of the sponge phantom reconstructed with MOSC  
The slices show the inserted beans getting resolved at their true depths (bottom left).

In another experiment, a stereotactic needle biopsy tissue-equivalent breast phantom was imaged on the fully set-up 25 beam x-ray system. The body of the 5.5 cm thick phantom is shaped to represent a partially compressed breast. It is made from a material that has a consistency similar to human tissue and includes many solid randomly positioned masses of varying sizes. This phantom was placed on a stage in front of the detector and no additional compression was applied. The air gap was about 2.5 cm and the total source to detector distance was about 64.5 cm. The phantom was illuminated using each one of the 25 sources running at a tube current of about 0.5 mA. The exposure time and the number of exposures were set so that the total exposure on the breast phantom was 100 mAs. The anode was operated at 28 kVp. A single projection image of the phantom is shown in figure 5.19.

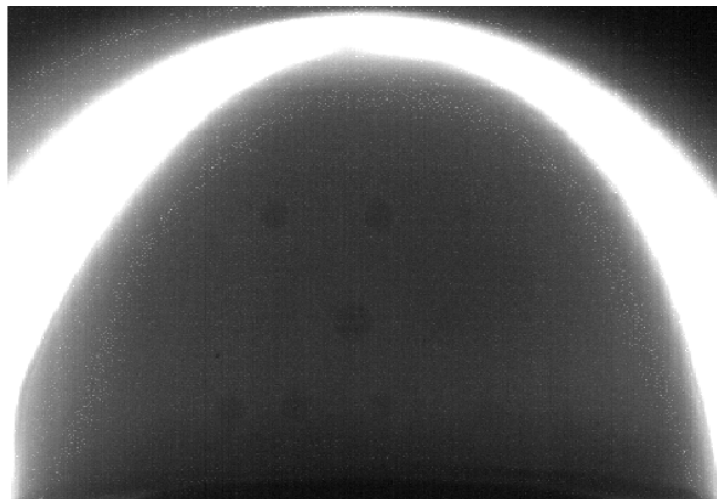


Figure 5.19 A single projection image of the commercial breast phantom

Corresponding blank scans (without the phantom) were also obtained. All images were cropped to a size of 1900 x 850 to show only the phantom. A simple profile

through the central mass seen in the projection image revealed the contrast ( $I_{obj} - I_{bkg}$ ) to noise ( $(\sigma_{obj} + \sigma_{bkg})/2$  where  $\sigma$  is the standard deviation) ratio (CNR) to be about 2.2. Twenty-five projection images were then used to reconstruct using MOSC with the designed geometric parameters. The reconstruction voxel size was  $0.1 \times 0.01 \times 0.01$  mm and 60 slices through the phantom were obtained. The reconstructed slices are shown in figure 5.20. The images are successive 3 mm slices and should be read top to bottom and then left to right. A profile through one of the masses in the reconstructed slice where it gets focused was used to calculate the CNR. The CNR was found to be about 10.

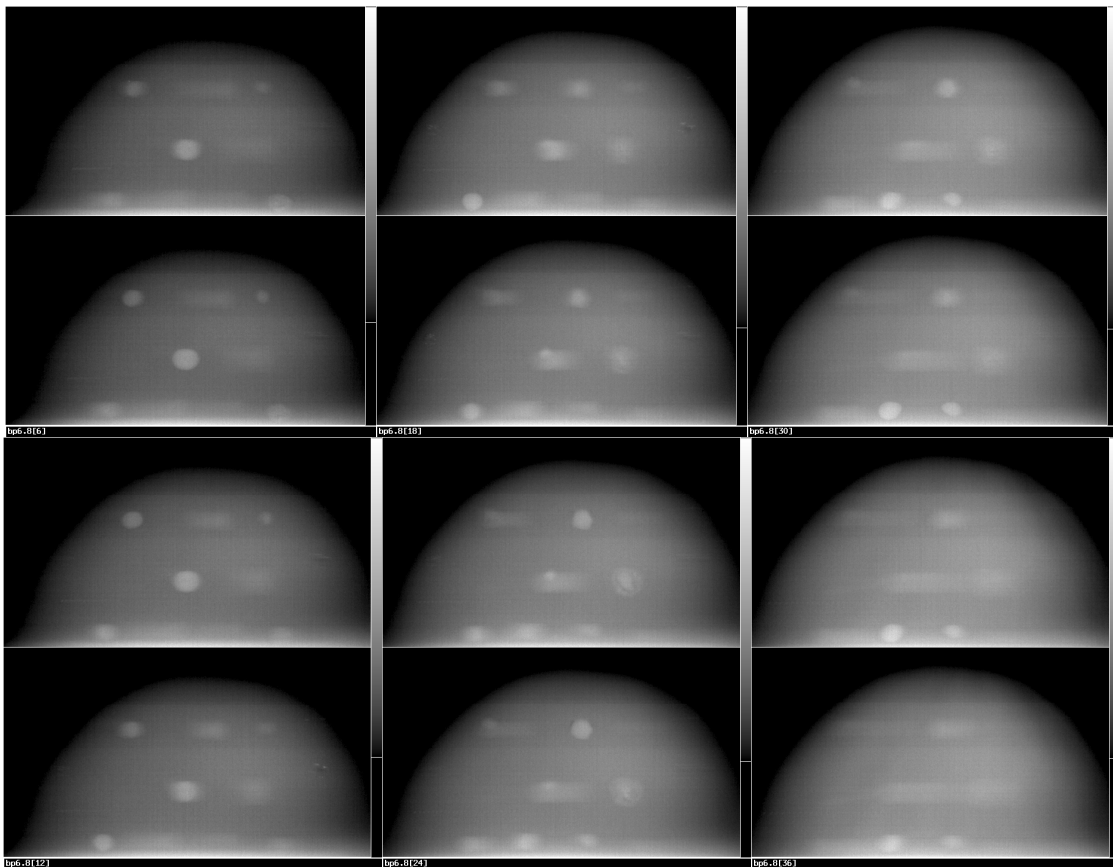


Figure 5.20 Slices of the commercial breast phantom reconstructed with MOSC.

Shown above are slices through the commercial phantom that show the different masses getting focused at their corresponding depths. The slices are 3 mm apart and the in-plane resolution is  $100 \mu\text{m} \times 100 \mu\text{m}$ . The slices should be read top to bottom and then left to right.

The same phantom was also imaged using the GE Senographe tomosynthesis unit undergoing clinical trial at UNC Hospitals. The imaging was done under identical conditions of anode voltage using Molybdenum as the anode as well as filter. The total exposure was 100 mAs in that case too although the exact thickness of the filter in the GE system is unknown. In addition, details on the detector or reconstruction were not furnished. However, a CNR analysis similar to what was done in our case was done on the projection and reconstruction images obtained from the GE system (shown in figure 5.21).

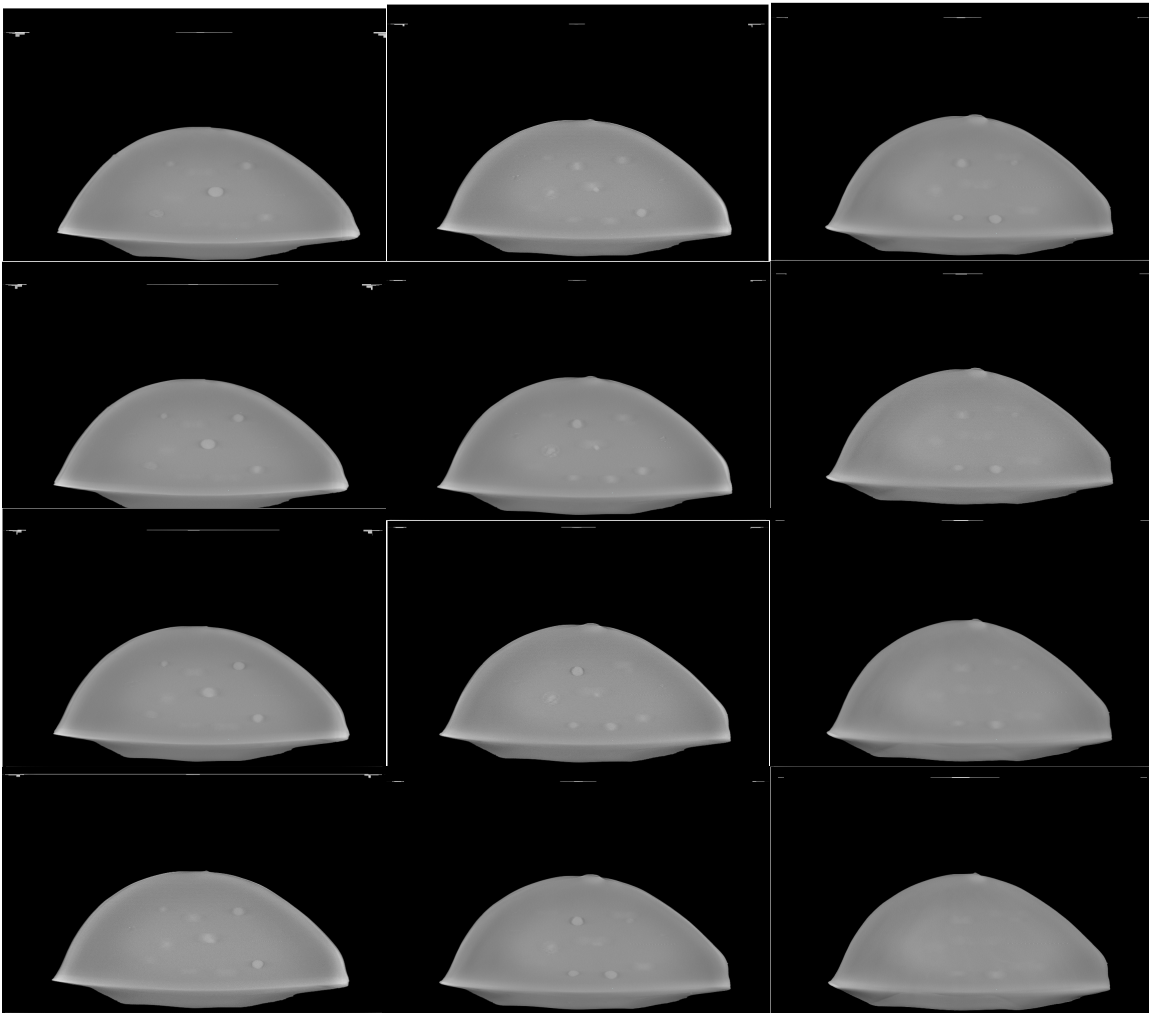


Figure 5.21 Reconstructed slices of the breast phantom obtained from the GE tomosynthesis unit.

The CNR on their projection image was estimated to be 3.3 while the reconstructed CNR was about 11. The reconstructed image quality looks similar in both cases. Therefore it is fair to say that our reconstruction performs and produces results that are as good as a system under clinical trial.

In order to exactly determine the resolution of the GE tomosynthesis unit, the projection MTF of the system was found by imaging the 100  $\mu\text{m}$  wire phantom and a commercial 10  $\mu\text{m}$  wire phantom on the GE scanner. The wire in each phantom is enclosed in clear cylindrical plastic so that there is a separation of only about 1.5 cm between the detector and the wire when the phantoms are placed on the surface of the detector, and with a source-to-detector distance of about 60 cm or more, the magnification is very close to 1. The projection images of the phantoms so acquired are then analyzed using the same Matlab program that we used to estimate the MTF of our system Argus.

The image of the 100  $\mu\text{m}$  wire together with the line spread function and the resulting MTF are shown in figure 5.22. It was found that with a 10  $\mu\text{m}$  wire, there is a substantial improvement in the projection MTF as illustrated in figure 5.22 (right) although the background is much noisier as seen in the line spread function graph. This indicates that for a system with a certain detector, a more accurate representation of MTF is obtained by using a wire that is smaller than the detector pixel pitch.

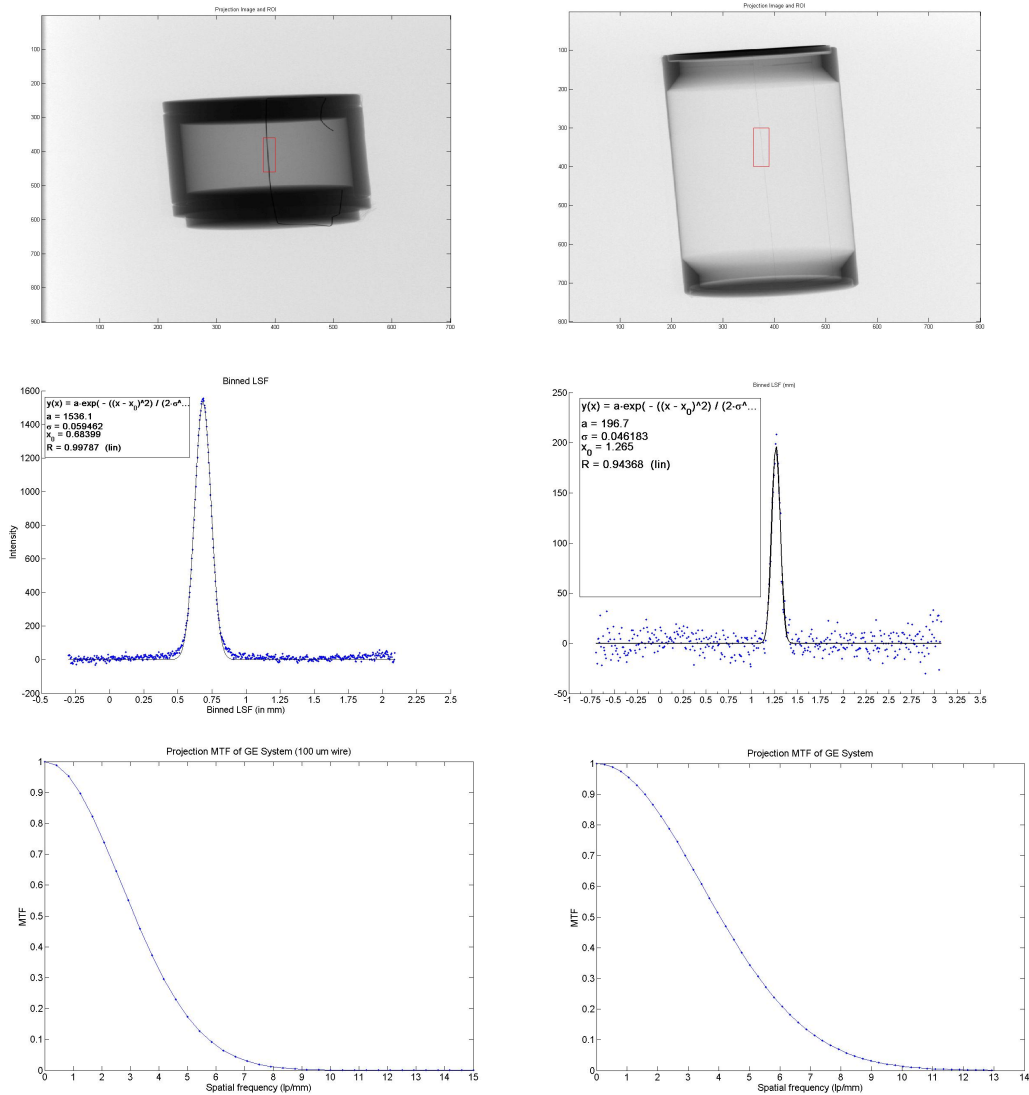


Figure 5.22 MTF of the GE scanner as determined using a 100  $\mu\text{m}$  wire (left) and using a 10  $\mu\text{m}$  wire (right).

The projection MTF of our system Argus has already been found to be about 2.8 lp/mm and the technician quoted and measured detector MTF for Varian Paxscan is about 3.1 lp/mm. This MTF was measured using the 100  $\mu\text{m}$  wire. Unfortunately, it is nearly impossible to see the 10  $\mu\text{m}$  wire in our case so that analysis was not done. In any case, the detector in the GE tomosynthesis

unit is far superior to the detector that is in use with Argus. The better resolution afforded by the GE detector may be partly responsible for the better image quality that may be perceived in the GE reconstructed slices.

It also appears from the reconstructed slices (figure 5.21) that the GE scanner incorporates some substantial post-reconstruction image processing algorithms that tend to enhance the appearance of the edges of the phantom. In order to do the same on our images, two approaches were followed. In the first case, a mask with a suitable threshold was applied on all the reconstructed slices in order to define the edges better. In the second case, based on the distribution of intensity values in the projection images, a binary mask was created using a suitable threshold intensity value. A Gaussian filter was applied to this mask to create a smooth boundary. This filtered mask was then used as the initial estimate file together with the projection images during reconstruction. The results of the two approaches yield similar results. However, both cases do result in tomographic slices of the breast phantom that have more sharply defined edges, a little more like what is seen on the reconstructed slices of the GE scanner than before. The reconstructed slices obtained by applying a Gaussian filtered mask to the projection images are illustrated in figure 5.23.

In addition, a careful evaluation of the reconstructed slices also revealed two sets of calcifications that get focused at different depths. These two reconstructed slices (with the window level adjusted to show the calcifications) are shown in figure 5.24.

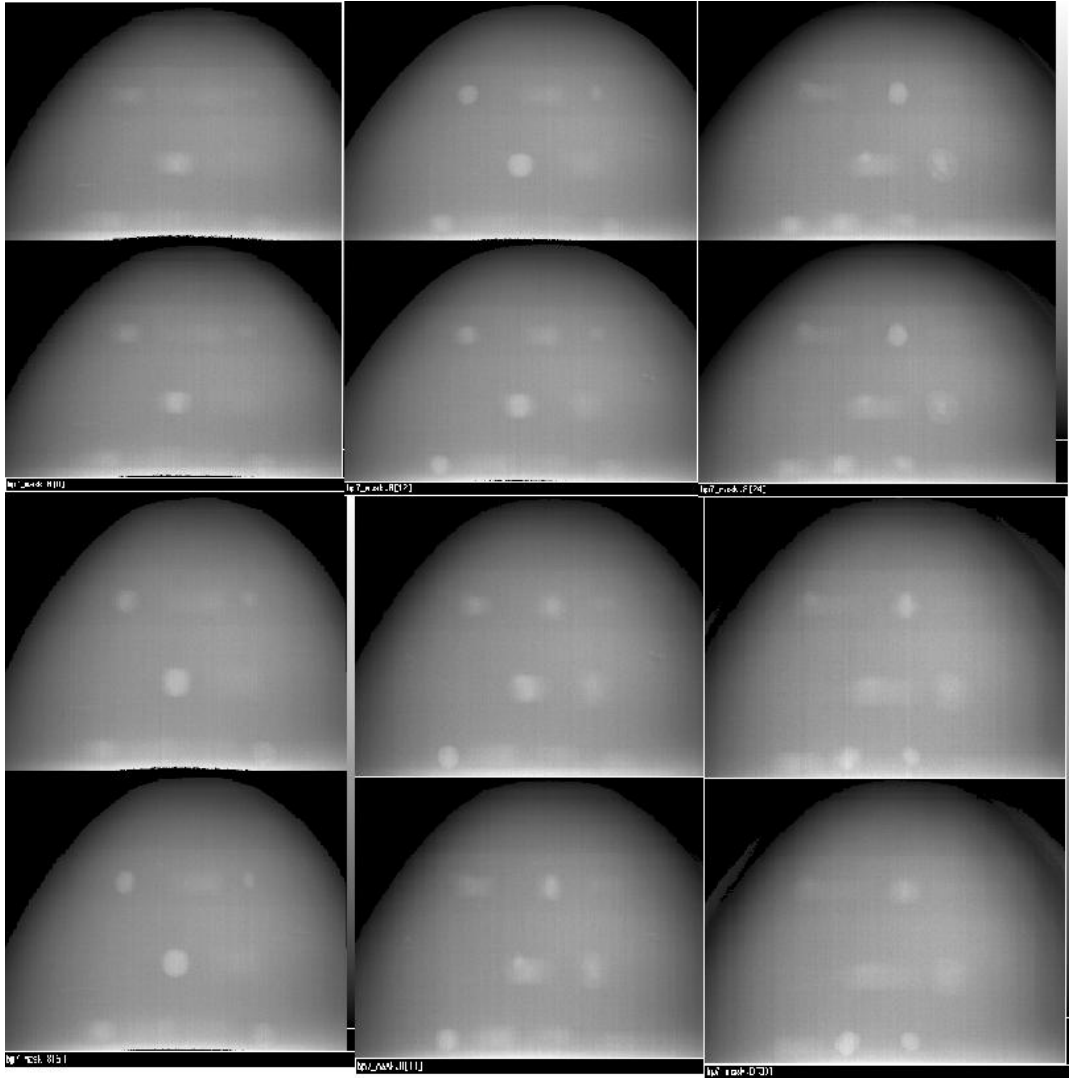


Figure 5.23 Slices of the commercial breast phantom reconstructed with MOSC after application of an edge-smoothing mask (projection images from Argus).

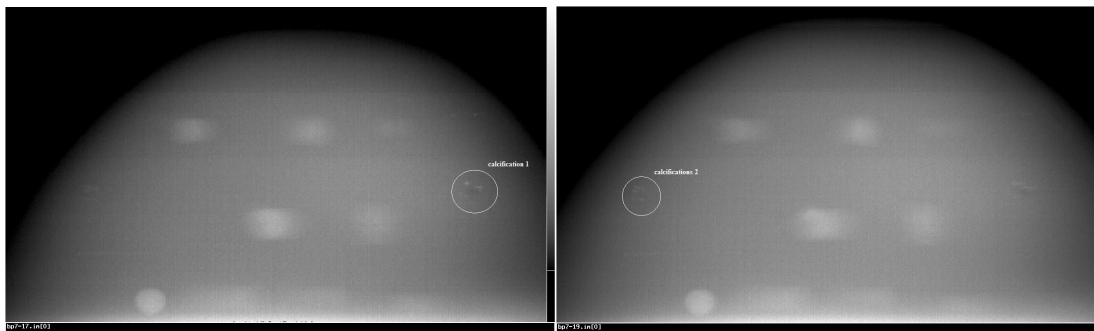


Figure 5.24 Tomographic slices that show two different sets of calcifications in the breast phantom.

## 5.6 Discussion

The advances in tomosynthesis imaging have been paralleled by similar advances in the reconstruction algorithms employed to reconstruct tomosynthesis projection images [30-33]. In general, algorithm development for tomosynthesis reconstruction is challenging because of the availability of a limited number of low dose projection images acquired over a small angular range but the general consensus seems to be that iterative reconstruction algorithms perform better than the analytical algorithms in the tomosynthesis set up due to many of the previously mentioned properties of the iterative algorithms. Iterative algorithms could be simple algebraic or statistical and we have chosen to use a statistical ML-based reconstruction algorithm for our novel system. Based on a comparison of the results obtained from using optimized versions of an algebraic algorithm and MOSC, it could be concluded that MOSC delivers better image quality. OSC and/or MOSC are also being tried on other configurations and have yielded consistent results. There may be different algorithms used by the other tomosynthesis systems under development that are claimed to be superior. A direct comparison of the reconstruction algorithms may not be fair or possible without knowing all the absolute details in the different techniques but it is believed that the modified OSC as applied to a novel imaging geometry such as ours will perform at least as well as other ML-based algorithms.

## References

1. Kak AC and Slaney M: Principles of computerized tomographic imaging, IEEE Press, NY, 1987.
2. Gordon R and Herman GT: Three-dimensional reconstructions from projections: A review of algorithms. International Review of Cytology, Academic Press, NY, pp. 111-151, 1974.
3. Hounsfield GN: A method of and apparatus for examination of a body by radiations such as x-ray or gamma radiation. Patent specification 1283915, The Patent Office, 1972.
4. Hsieh J: Computed Tomography: Principles, Design, Artifacts, and Recent Advances, SPIE Press, 2003.
5. Kak AC: Computerized tomography with x-ray emission and ultrasound sources. Proc. IEEE, 67, pp. 1245-1272, 1979.
6. Pan SX and Kak AC: A computational study of reconstruction algorithms for diffraction tomography: Interpolation vs. filtered-backprojection. IEEE Trans. Acoust. Speech Signal Processing. ASSP-31, pp. 1262-1275, 1983.
7. Feldkamp LA, Davis LC, et al: Practical cone-beam algorithm. J. Opt. Soc. Am. 1(6), pp. 612-619 (1984).
8. Wang G, Lin TH, et al.: A general cone-beam reconstruction algorithm. IEEE Trans. Med. Imag. MI-12, pp.486-496, 1993.
9. Grangeat P: Mathematical framework of cone-beam 3D reconstruction via the first derivative of the Radon transform. Mathematical Methods in Tomography, Lecture Notes in Mathematics, 1497, pp. 66-97, Springer Verlag, Berlin, 1991.
10. Defrise M, Noo F, et al.: A solution to the long object problem in helical cone-beam tomography. IEEE Trans. Med. Imag. 19, pp. 848-863, 2000.
11. Kohler Th, Proksa R, et al.: A fast and efficient method for sequential cone-beam tomography. Med. Phys. 28(11), pp. 2318-2327, 2001.
12. Lalush DS, Wernick MN: Iterative Reconstruction Algorithms, Emission Tomography: The fundamentals of PET and SPECT, Academic Press, 2003.

13. Kaczmarz S: Angenaherte auflosung von systemen lenearer gleichungen. Bull. Int. Acad. Pol. Sci. Lett. A., 355-357 (1937)
14. Rosenfeld A and Kak AC: Digital Picture Processing. Academic Press, Orlando, 1982.
15. Gordon R, Bender R, et al: Algebraic Reconstruction Techniques (ART) for three-dimensional electron microscopy and x-ray photography. J. Theor. Biol. 29, pp. 471-481, 1970.
16. Andersen AH & Kak AC: Simultaneous Algebraic Reconstruction Technique (SART): A superior implementation of the ART algorithm. Ultrason. Imag. 6, pp. 81-94, 1984.
17. Herman GT and Lent A: Iterative Reconstruction algorithms. Comput. Biol. Med. 6, pp. 273-294, 1976.
18. Solmon DC: The X-ray transform. J. Math. Anal. Appl. 56, pp. 61-83, 1976.
19. Andersen AH: Algebraic reconstruction in CT from limited views. IEEE Trans. Med. Imag. 8(1), 1989.
20. Kak AC: Tomographic imaging with diffracting and non-diffracting sources. Array Signal Processing, S. Haykin, Ed. Englewood Cliffs, NJ: Prentiss-Hall, 1985.
21. Andersen AH: The tomography transform and its inverse in geometrical optics. J. Opt. Soc. Amer. A, 4: pp. 1385-1395, 1987.
22. Lange K and Carson R: EM reconstruction algorithms for emission and transmission tomography. J. Comp. Assist. Tomogr. 8, pp. 306-316, 1984.
23. Lalush DS and Tsui BMW: Fast transmission CT reconstruction for SPECT using a block-iterative algorithm. IEEE Trans. Nucl. Sci. 47, pp. 1123-1129, 2000.
24. Hudson HM and Larkin RS: Accelerated image reconstruction using ordered subsets of projection data. IEEE Trans. Med. Imag. 13(4), pp. 601-609, 1994.
25. Lange K and Fessler JA: Globally convergent algorithms for maximum a posteriori transmission tomography. IEEE Trans. Imag. Proc. 4(10), pp. 1430-1438, 1995.

26. Kamphuis C and Beekman FJ: Accelerated iterative transmission CT reconstruction using an ordered subsets convex algorithm. *IEEE Trans. Med. Imag.* 17(6), pp. 1101-1105, 1998.
27. Lalush DS, Quan E, et al.: Tomosynthesis reconstruction from multi-beam x-ray sources. *Proceedings of 2006 IEEE International Symposium on Biomedical Imaging*, 2006.
28. Quan E and Lalush DS: A faster ordered-subset convex algorithm for iterative reconstruction in a rotation-free micro-CT system. *Phys. Med. Biol.* 54, pp. 1061-1072, 2009.
29. Rajaram R, Yang G, et al.: Image reconstruction for a stationary digital breast tomosynthesis system. *Proc. of SPIE* 7258, 72582L, 2009.
30. Zhang Y, Chan H, et al.: A comparative study of limited-angle cone-beam reconstruction methods for breast tomosynthesis. *Med. Phys.* 33(10), pp. 3781-3785, 2006.
31. Suryanarayanan S, Karellas A, et al.: Evaluation of linear and nonlinear tomosynthetic reconstruction methods in digital mammography. *Acad. Radiol.* 8, pp. 219-224, 2001.
32. Godfrey DJ, Warp RJ, et al.: Optimization of matrix inversion tomosynthesis. *Proc. SPIE* 4320, pp. 696-704, 2001.
33. Wu T, Moore RH, et al.: A comparison of reconstruction algorithms for breast tomosynthesis. *Med. Phys.* 31(9), pp. 2636-2647, 2004.

## 6 Conclusions and Future Direction

In this research study, a fully stationary digital breast tomosynthesis system 'Argus' with a novel geometry was completely characterized. The system was tested by acquiring preliminary images that were reconstructed by applying an iterative reconstruction algorithm to demonstrate good image quality.

Extensive simulation results enabled us to set up the final system. It was found that there is an optimum number for projection views within a certain angle given a fixed dose. The results also demonstrated that the tomosynthesis imaging quality could be improved by increasing the total angular coverage as it approximates the full CT scenario more and more.

The methods employed to characterize the system are mostly well established and reviewed in literature past and it is not the goal of this dissertation to devise new characterization techniques. However, it is our goal to apply those characterization techniques to our *stationary* system, which is even more unique because of its geometry. Some crucial results have been obtained during the characterization process. The resolution in terms of the modulation transfer function showed that the system resolution is largely limited by the detector. The results thus enabled us to focus on increasing the cathode size in order to achieve greater flux. The results of the geometric calibration seem to suggest that a good calibration is possible with the method of choice. The most important

geometric parameters for reconstruction were found to be the two-dimensional source location in space, and the source to detector distance. The method may have a slightly large inherent variance in the source location. These variances are likely due to highly correlated geometry parameters that may tend to cancel each other out. For instance, detector tilt and the source location in terms of  $(u_0, v_0)$  are highly correlated. Because of such correlations, a direct and simple evaluation of the deviations in the geometric parameters may not be a good indication of the accuracy of the calibration as large deviations may not necessarily mean a large error in alignment. However, future modifications to the method can include using the designed or known geometric parameters to act as constraints so as to reduce the variance. It may also be possible to improve the accuracy in the parametric estimation by using a phantom with more point objects at multiple planes than just the two as was used in this project. In any case, the reconstruction results demonstrated that the uncertainty does not result in any noticeable loss in resolution or contrast when applied to the tomosynthesis imaging geometry. It might even be that for future systems with larger cathodes, if the central x-ray source alone is calibrated, then the use of the designed values for the other sources may be enough for the reconstruction.

The reconstruction algorithm of choice for our system is the modified ordered subsets convex (MOSC) algorithm and it has been remarkably successful. It appears to be robust enough to handle minor inconsistencies in the geometry as well in the projection data. The early results using this iterative algorithm on preliminary images are what motivated us to proceed with the

design and construction of the full scale system. The superb image quality as well as short reconstruction time provided by MOSC as demonstrated with the home-made sponge phantom and the commercial phantom on the full scale system thus greatly validates our choice. Under very similar imaging conditions, the reconstruction image quality in terms of the contrast-to-noise ratio and spatial resolution obtained on our first generation system is on par with that obtained on a dedicated tomosynthesis unit developed by a major healthcare company.

It would be apt to call Argus as the world's first and up until now the only stationary DBT system. On one level, Argus is a successful demonstration of bench-to-bedside translational research. The fundamental technology that enabled Argus is the availability of field-emission carbon nanotube based x-ray sources. On another level, the set-up and successful characterization of the stationary DBT system was accomplished so that the image quality is at least as good as, if not better than, the other current DBT systems under development. The system has better stability because it is completely stationary. In addition, there is a great potential to reduce the total imaging time. It is important to remember that in breast cancer imaging, any reduction in the scan time can significantly reduce the dose as well as the pain of compression to the patient.

It is believed that tomosynthesis will at some point of time be able to replace or assist mammography in the screening and early diagnosis of breast cancer. There is a lot of research going on about new tomosynthesis systems, acquisition techniques, and reconstruction algorithms but clinical trials on some DBT systems are already underway in certain universities and hospitals. It is a

proud achievement that our stationary DBT is well on its way there. The groundbreaking study of Argus could change the way tomosynthesis is done.

Work has also started in our group on the next generation DBT system. This new system will be the clinical prototype stationary DBT scanner that will be able to acquire 25 projection images of the patient in either the medio-lateral oblique or the cranio-caudal positions that are common in conventional mammography. This system will have larger cathodes that are capable of delivering a higher x-ray flux that is required in order to reduce the total scan time. A total scan time of only 3 seconds is now a possibility. Research is also being undertaken to study the feasibility of using quasi-monochromatic x-rays. By using a tungsten anode running at higher energy (60 kVp) together with an appropriate thickness of a suitable filter (Cerium) it is possible to obtain a very narrow spectrum of energy as the output. Quasi-monochromatic imaging has been shown to increase contrast in tissues with similar attenuation. The use of a higher mean energy translates into reduced dose to the patient. It might also help reduce beam hardening effects where applicable. It is important to note that this thesis work on Argus has already set the standards for characterization and image reconstruction techniques for any future DBT systems so that the major focus can now be on the new system alone.

Argus is a system devoted to breast imaging but the idea of many individually addressable x-ray sources has a great potential to be applied to other systems such as tomosynthesis of the chest or even a CT system. Other research possibilities include multiplexing and dual energy imaging.